Enhancing PEPT: high fidelity analysis techniques with augmented detection systems

Robert van der Merwe

Supervisors: Dr T. Leadbeater and Associate Professor S. Peterson

A thesis submitted in fulfilment of the requirements for the degree of Master of Science in the

MeASURe Unit
Department of Physics
University of Cape Town

23 December 2023

Abstract

Enhancing PEPT: high fidelity analysis techniques with augmented detection systems
by Robert van der Merwe
supervised by Dr T. Leadbeater and Associate Professor S. Peterson
for the degree of **Master of Science**
Faculty of Science, Department of Physics

Positron emission particle tracking (PEPT) is a non-invasive, tracer-based technique used in the study of dynamic systems, such as particulate and fluid flows. Relying on positron imaging principles, typical PEPT systems operate with millimetre precision at tracking speeds of up to 10 m/s, with applications in fields from engineering to medicine. Performance is constrained by the efficiency of conventional fixed geometry detector systems and achievable activity of tracer particles, creating challenges when addressing phenomena on the micro-scale. Previous work with a pair of pixelated cadmium zinc telluride (CZT) room temperature semiconductors (9680 pixels of 1.8 x 1.8 x 0.5 mm^3) exhibited potential in micro-scale PEPT, but achievable location rates and field of view (FOV) were limiting. To address these issues, a modular bismuth germanate oxide (BGO) scintillator array, consisting of 1024 detector elements (512 pixels of 6.75 x 6.25 x 30 mm^3 and 512 pixels of 4.1 x 4.0 x 30 mm^3), has been developed and characterised for use in a hybrid system, combining semiconductor and scintillator devices. Optimal detection system geometry was determined through numerical modelling of system sensitivity, with the BGO array covering a FOV of $120 \times 174 \times 102$ mm^3 and the high-resolution semiconductor FOV of $62 \times 42 \times 20$ mm^3 placed centrally. This design maximises absolute efficiency through the scintillators and spatial resolution through the semiconductors. A coincidence timing resolution of 5.37 ± 0.17 ns and an energy resolution of $30.51 \pm 0.48\%$ at 511 keV was measured for the BGO devices, enabling optimisation of coincidence gates and energy level discriminators respectively. Using a novel 3D positioning stage and a 20.11 ± 0.26 kBq Na-22 calibration source, measurements of system sensitivity, spatial resolution and accuracy were performed. Sensitivity profiles were found in agreement with simulation, with a maximal central sensitivity of 34.8 ± 0.6 cps/kBq. Sub-millimetre system accuracy was achieved in all axes except between the BGO detector faces, in which an expected warping effect was identified. Sub-millimetre spatial resolution, σ, was achieved for a maximum location rate per unit activity, L', of 0.45 Hz/kBq, with an identified $\sigma = 1.5\sqrt{L'}$ trade-off to be optimised for specific use cases. The results of this work demonstrate the applicability of PEPT to the study of micro-scale phenomena and outline the path towards hybrid implementation.

Acknowledgements

This work represents the invaluable support and contribution of many people throughout my MSc who I wish to acknowledge and thank.

First and foremost, I would like to thank my supervisor Tom Leadbeater. Your wealth of knowledge and wisdom surrounding PEPT and research in general has been an amazing resource for me over the years. Your guidance, support, and the opportunities you've made available to me have enabled me to grow significantly as a researcher throughout my studies. This work truly would not be possible without you.

Secondly, I would like to thank my co-supervisor and HoD Steve Peterson. Your knowledge of the Polaris system, support in conference planning/funding, insight in publication preparation, and general assistance in all things UCT Physics have been invaluable.

Thanks must also go to Tanya Hutton for all of the support with 3D modelling and printing matters. Without your technical skills and experience, the quality of this work would have suffered substantially.

I would also like to thank my frequent co-authors Andy Buffler and Michael van Heerden for your consistent willingness to provide detailed feedback and advice on my written material. Your comments have always been instrumental in refining and enhancing the quality of my presentations and publications.

Thanks also go to all of my colleagues in physics, in particular the other occasional inhabitants of the PEPT lab, Alice and Mikayla. Our discussions on all things PEPT have always been useful, and I hope you can see the impact your contributions had on this work.

Lastly, heartfelt thanks go to my friends and family. Your consistent support has been my source of motivation and resilience throughout this degree, and you have all filled my life with much joy. To my parents, Karen and Steve, and my sister Georgie, thank you for your love and support throughout my life. Your unwavering encouragement has always enabled me to meet any challenge. Thank you to my grandmother Balli for always doing crosswords with the professor, inspiring my career trajectory from childhood. Finally, thanks to my friends Adam, Alex, Maria, Michyla, Rachel, Ra-eez, Rashaad and many others for countless years of friendship.

Research Contributions

Conference Proceedings (abstract), December 2023
R. van der Merwe et al. Micro-scale particle tracking with hybrid detectors. In *Proc. of IEEE NSS MIC RTSD 2023 (November 4-11 Vancouver)*, 2023

Presentation, November 2023
Micro-scale particle tracking with hybrid detectors, presented by R. van der Merwe at the 2023 IEEE Nuclear Science Symposium, Medical Imaging Conference and International Symposium on Room-Temperature Semiconductor Detectors (NSS MIC RTSD 2023), 4 - 11 November 2023, Vancouver, Canada

Conference Proceedings, September 2023
R. van der Merwe et al. Micro-scale particle tracking using hybrid detectors. *J. Phys.: Conf. Ser.*, 2586, 012123

Conference Proceedings (co-author), September 2023
T. Leadbeater et al. Dynamics of physical flows measured by positron emission techniques. *J. Phys.: Conf. Ser.*, 2586, 012127

Conference Proceedings, December 2022
R. van der Merwe et al. MicroPEPT: A step toward hybrid PEPT detectors. In *Proc. of SAIP2022, the 66th Annual Conf. of the South African Institute of Physics (July 1-8 Gqeberha)*, pages 588-593, 2022

Conference Proceedings (co-author), December 2022
A. McKnight, T. Leadbeater, and R. van der Merwe. Characterisation of a new LSO block detector for Positron Emission Particle Tracking. In *Proc. of SAIP2022, the 66th Annual Conf. of the South African Institute of Physics (July 1-8 Gqeberha)*, pages 224–229, 2022

Presentation, September 2022
Micro-scale particle tracking using hybrid detectors, presented by R. van der Merwe at the 28th International Nuclear Physics Conference (INPC 2022), 11 - 16 September 2022, Cape Town, South Africa

Presentation, July 2022
MicroPEPT: A step toward hybrid PEPT detectors, presented by R. van der Merwe at the 66th Annual Conference of the South African Institute of Physics (SAIP 2022), 1 - 8 July 2022, Gqeberha, South Africa

Abbreviations

ADC	Analogue-to-digital converter
BGO	Bismuth germanate oxide
CFD	Constant fraction discriminator
CT	Computed tomography
CZT	Cadmium zinc telluride
FDG	Fluorodeoxyglucose
FOV	Field of view
FWHM	Full width at half maximum
LLD	Lower level discriminator
LSO	Lutetium oxyorthosilicate
LOR	Line-of-response
MCA	Multi-channel analyser
MWPC	Multi-wire proportional chamber
PET	Positron emission tomography
PEPT	Positron emission particle tracking
PMT	Photomultiplier tube
SBSR	Spatiotemporal B-spline reconstruction
SSC	Separated Sector Cyclotron
SUV	Standardised uptake values
UCT	University of Cape Town
ULD	Upper level discriminator

Contents

Chapter 1

Introduction and background

1.1 Introduction

Positron emission particle tracking (PEPT) is a non-invasive tracking technique typically used to study the dynamic properties of millimetre-scale flow systems. With a recent desire to study micro-scale phenomena, this thesis builds upon the work of a previous University of Cape Town (UCT) MSc student who developed a cadmium zinc telluride (CZT) semiconductor system towards micro-scale PEPT applications, namely proton beam line tracking in proton radiotherapy [1].

With this CZT system, significant improvements to PEPT spatial resolution were achieved in comparison to conventional systems, offering minimal location uncertainties of approximately 100 micron. However, the achievable absolute efficiency, and therefore location rate, was poor in comparison to conventional scintillator systems, limiting the system's applicability to slow-moving (mm/s) phenomena and post-treatment imaging.

This thesis builds upon the achievements of the semiconductor system but aims to account for its limitations through the design and development of a modular bismuth germanate oxide (BGO) scintillator system, offering significantly increased absolute efficiency. Through the simulation, construction and characterisation of the scintillator system in this thesis, and the future integration of both semiconductor and scintillator systems into a hybrid camera, this research serves as a step towards a broadened scope of micro-scale PEPT applications, such as the potential study of novel microfluidic systems.

Thesis outline

Chapter 1 outlines the background of positron emission imaging, describing the history of PEPT instrumentation as well as current approaches in tracking algorithms and tracer production. A crucial discussion on PEPT spatial resolution is given, significantly impacting the design decisions of later chapters to enable micro-scale precision.

Chapter 2 follows to provide an in-depth technical description of the relevant PEPT detector systems. A brief description of the semiconductor devices is given with reference to previous work, followed by a full description of the radiation detection, data acquisition and data processing methodology used by the BGO scintillator devices developed here. In addition, characterisation of the calibration tracer particle is performed, enabling

precise sensitivity measurements in later chapters, and a description of the modified 3D positioning stage used for tracer positioning is given.

Chapters 3 to 5 handle the design and characterisation of the modular camera. In Chapter 3, the components of the system are characterised in terms of their energy and timing resolution, determining optimal energy level discriminators and coincidence windows respectively. These values are optimised to enable low-noise detection, ensuring sufficient system spatial resolution for micro-scale applications without sacrificing on location rates.

Chapter 4 makes use of a Monte Carlo simulation of the system sensitivity profile for system geometry design. Here, a uniform sensitivity profile maximising absolute efficiency is desired to improve upon achievable location rates, and several geometry possibilities are discussed and compared. Following selection of the optimal system geometry, the system construction process is detailed, realising an experimental version of the designed modular positron camera in the laboratory.

System characterisation in terms of optimal tracking parameters, sensitivity, spatial resolution and accuracy is performed in Chapter 5 throughout the field of view (FOV) of the system. These results are discussed and evaluated, considering the intended development towards a hybrid semiconductor/scintillator system.

Finally, Chapter 6 presents the conclusions of this thesis, highlighting the primary outcomes of this work, and proposes future work to enable the complete development of the micro-scale hybrid PEPT system.

1.1.1 PEPT: History and background

Positron emission particle tracking is a powerful imaging technique based on medical positron emission tomography (PET), whereby radiolabelled positron emitting tracer particles can be non-invasively tracked within a system of interest. PEPT is typically applied to the study of industrial processes, particularly in particulate and fluid flow phenomena, with mining and minerals applications, among many others [2–8]. By measuring the instantaneous position (with associated uncertainty) of the tracer particle over time as it flows within a system, a Lagrangian description of the related flow can be obtained. Through computation and analysis of system velocity and acceleration fields, as well as occupancy and residence times, an Eulerian description of the system can be determined, as described and performed in [9].

The world's first PEPT system at the University of Birmingham, UK, consisted of a pair of position-sensitive multi-wire proportional chambers (MWPCs), placed opposite one another to perform coincidence measurements. Initially designed by the Rutherford Appleton Laboratory to improve spatial resolution and reduce instrumentation cost in PET, the camera's poor detection efficiency made it unsuitable for medical applications, leading to its development towards flow mapping for industrial applications at the University of Birmingham [10]. With this system, initial development of the PEPT technique was performed, achieving millimetre precision with location rates, or the frequency at which the position of the tracer could be determined, on the order of hertz in 1993 [11]. This system operated for approximately 15 years, until it was replaced in 1999 by the ADAC Forte, shown in Figure 1.1, consisting of two NaI(Tl) crystals attached to arrays of photomultiplier tubes on separate, opposing heads. With improved detection efficiency,

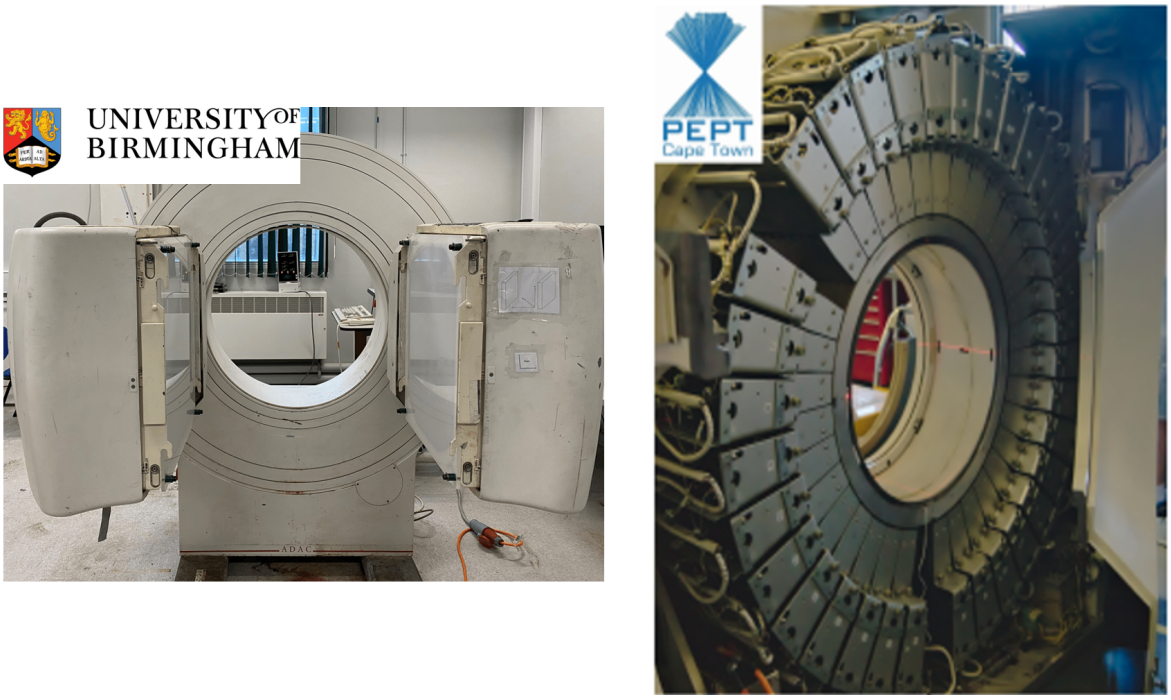

Figure 1.1: The ADAC Forte gamma camera housed at Birmingham, UK (left) and the Siemens HR++ PET scanner housed at iThemba LABS, Cape Town (right).

timing resolution and energy resolution, sub-millimetre precision was achieved at a significantly increased 250 hertz location rate [12], enabling numerous studies on flow-related topics to the present day [13, 14].

A significant advancement in PEPT instrumentation was achieved with the use of pixellated BGO block detector systems, following the acquisition of the CTI Inc. ECAT931 PET camera at the University of Birmingham in 2002 [15]. This system offered 128 detector blocks, each segmented into 8x4 detector elements which were coupled to an array of photomultiplier tubes. Subsequently, the Siemens/CTI ECAT951 system was acquired, with 8x8 segmentation reducing the pixel size of the system and improving upon achievable spatial resolution. Due to the self-contained nature of these detector blocks, modular systems designed for specific applications became possible, requiring custom data acquisition systems. With one such modular system 1-4 kHz location rates were achieved with half-millimeter precision for stationary particles, reducing to 2.5 mm precision for average particle speeds of 1 $m.s^{-1}$ [2].

In 2009, PEPT Cape Town was established by the UCT Department of Physics at a purpose-built laboratory on the iThemba LABS site in Cape Town, South Africa, with the donation of a Siemens EXACT HR++ PET camera which was modified for PEPT usage. The HR++ was designed for high sensitivity and resolution, and through its development, tracer particles are tracked with millimetre precision at kilohertz location rates, reducing as the tracer particle speed increases from 1 $m.s^{-1}$ to the maximum achieved speed of 15 $m.s^{-1}$ [16].

Despite the demonstrable success of PEPT in the measurement of flow in physical and engineering systems, with every advancement in instrumentation improving upon

the achievable precision and tracking speed, a recent desire to address flow phenomena on the micro-scale has led to the necessity of advanced instrumentation and technique development to address the limitations of existing systems.

At the micro-scale, tracer activities are necessarily limited given the difficulty in fabrication (see Section 1.2.2). In addition, existing PET/PEPT detection systems are typically constructed with fixed geometries, limiting the achievable geometric, and therefore absolute, efficiency. These factors limit the achievable sensitivity of the system, which consequently limits the achievable location rate (see Section 1.3).

Since PEPT is typically used to examine dynamic systems, the location rate is crucial in the quality of analysis that can be performed, as the trajectory of the tracer particle is interpolated between measured locations. If the time between measured locations is large relative to the motion of the tracer, small-scale elements of the motion cannot be inferred, reducing the information extracted from the system. As a result, uncertainty bounds on the tracer trajectory increase, propagating and growing through higher-order measurands of the system such as the velocity and acceleration, and hence to force and energy.

Due to these limitations of existing systems, this MSc develops enhanced instrumentation to perform micro-scale low activity PEPT, with location rates enabling the study of micro-scale flows moving at greater speeds (cm/s) than previously achieved (mm/s) at this scale [1].

1.1.2 Enhanced systems

As a first step towards realising micro-scale capabilities in PEPT, previous work [1] investigated the use of room-temperature semiconductor CZT detectors for PEPT applications. UCT acquired two PolarisJ CZT units, produced by H3D Inc., for prompt gamma imaging research which were adapted for use in PEPT as shown in Figure 1.2. With this system, micro-scale location uncertainties were achieved with a selection of tracer particles with varying sizes and activity. However, the semiconductor intrinsic efficiency and timing resolution were limited in comparison to the scintillator crystals typically used in PEPT, resulting in maximum location rates on the order of tens of hertz with optimal activity tracer particles. In addition, the small form factor of the Polaris units coupled with their poor intrinsic efficiency required the units to be placed close to one another to maximise their geometric efficiency. As a result, the addressable FOV of the system was small, limiting possible applications to those that would actually fit within the system footprint in practice.

In this work, the semiconductor limitations are addressed through the development and characterisation of a proof-of-concept modular BGO scintillator array, making use of existing hardware and data acquisition systems as shown in Figure 1.2. The primary purpose of the scintillator system is its integration into a hybrid camera alongside the Polaris system, leveraging the improved intrinsic efficiency and timing resolution of the scintillator crystals to improve upon the overall achievable location rates and increase the system FOV.

In comparison to existing PET systems, especially high resolution preclinical systems, the primary benefit of developing the scintillator array is to enable a high degree of modularity, ensuring the geometric efficiency and achievable FOV of the system can

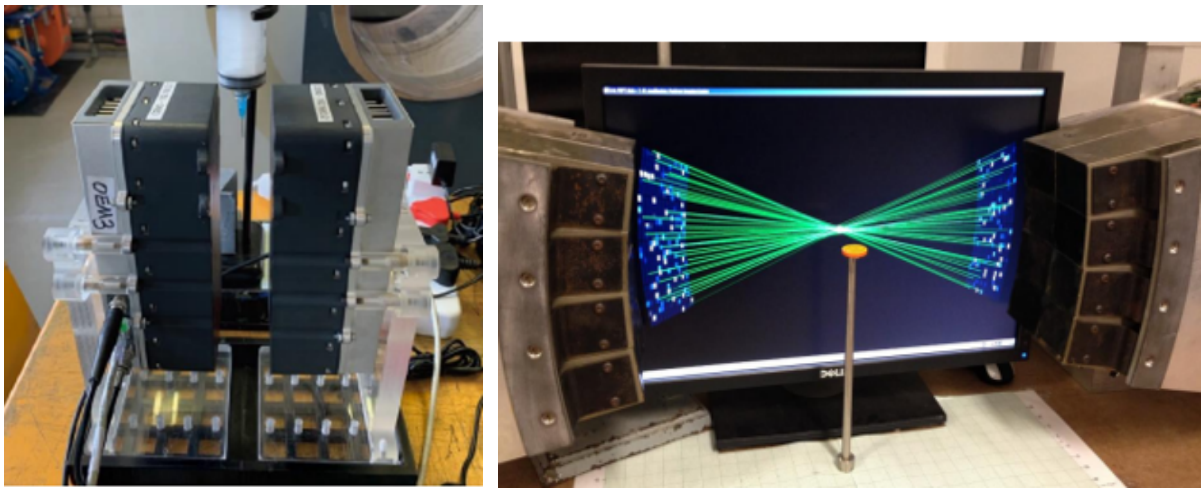

Figure 1.2: The Polaris system performing PEPT measurements at iThemba LABS with a Ga-68 tracer placed on the tip of a hypodermic needle [17] (left) and the UCT modular BGO array (right).

be optimised for any desired applications. As no particular application was designed towards in this work, a reasonable proof-of-concept system geometry is used to inform upon the achievable results with such a system, whilst also developing the construction and characterisation pipeline for future alternative geometries.

Initial applications of the hybrid system include identified micro-scale applications such as proton beam line tracking, however the versatility of the modular system enables applications in broader research. An illustrative example of the system versatility is its potential application with the recently acquired Siemens Biograph 16 HiRez PET/CT scanner, currently undergoing commissioning at UCT [18]. Combining X-ray tomography with PET/PEPT imaging, this system enables novel opportunities for simultaneous structural and functional imaging at PEPT Cape Town. However, the spatially distinct FOVs of the CT and PET components present challenges in the coregistration of each detection modality. To address this, a modular PET/PEPT array facilitates optimal system positioning allowing the CT and PET FOVs to overlap in space, enabling true simultaneity of measurement.

1.1.3 Micro-scale applications

The desire to improve upon PEPT systems and techniques, particularly towards the micro-scale, is driven by potential applications. Typical use cases of PEPT are of significant industrial importance, such as the measurement and characterisation of multiphase, particle-laden and particulate material flows [2] with applications as diverse as energy and water sciences [4, 7, 19], metallurgy [20], mining [6] and pharmaceuticals [8], among many others [21]. Therefore, improvements made to PEPT systems and techniques will enhance physical measurement capabilities, naturally increasing the complexity of systems that can be investigated as well as the quality of analysis that can be performed, with positive impact on the mentioned fields.

Beyond the typical use cases of PEPT, an alternative, relatively unexplored appli-

cation space is the biomedical sector, where PET already plays a significant role in the domain of diagnostic imaging. With recent advances in tracer production, instrumentation and algorithms, PEPT has become increasingly feasible for micro-scale biomedical applications, making use of previously unmeasured dynamic system information to enable the study of complex micro-scale biological and fluid systems. Possible use cases include the tracking of individual cells in cell-based therapies [22], the study of blood flow [23], and dose verification in proton radiotherapy [24]. In particular, the application of dose verification was the initial driving force behind the development of PEPT with semiconductor systems at PEPT Cape Town. Through PEPT, with simulation demonstrating viability [1], the positron emitting radioisotopes produced along the beam line may be tracked *in situ*, informing on the position of the beam line during treatment for dose verification methods.

Besides the specific biomedical applications of PEPT, direct improvements to the PEPT technique and associated systems will have implications in the biomedical space, as problems solved in PEPT have use cases in medical PET/CT, such as patient/organ motion tracking [25], non-uniform FOV corrections, reduction of image artefacts from physical structures, etc. Through the development of PEPT towards the micro-scale with modular, hybrid devices, the expected improvements in measurement capability and developments in analysis techniques will feed back into these spaces.

1.2 Positron emission imaging

Fundamentally, all positron emission imaging techniques rely on the placement of positron emitting tracers within a system of interest. Following emission and after rapidly thermalising, these positrons annihilate with free electrons in surrounding matter to produce two approximately back-to-back 511 keV annihilation photons. If these photons are detected in coincidence, i.e. within a short time window of one another, by a position-sensitive detection system, a line-of-response (LOR) can be drawn in three dimensions connecting the two detection points, and as a result of the back-to-back nature of annihilation this LOR ideally defines the line along which the annihilation occurred.

In medical PET, tracers typically take the form of a distributed fluid containing biologically relevant molecules labelled with an appropriate radioisotope. Over an extended time, a large collection of LORs can be measured and tomographic techniques can be applied, following any necessary corrections, to accurately reconstruct an image of the tracer distribution and concentration. The concentration of the tracer is commonly represented by standardised uptake values (SUVs), which express the ratio of measured activity within a region of interest to the known injected activity, after appropriate corrections for scatter and decay. Typically, these values range in the order of hundreds of megabecquerel [26]. When applied to biological systems, PET images visualise metabolic and physiological processes and can be used in imaging tumours, bone formation, blood flow, etc.

In standard PET measurements, images are acquired over minutes [27], making use of many LORs to produce a single image. Advancements in dynamic PET techniques have reduced image acquisition times by employing gating approaches and enabled the extraction of short timescale dynamic information from data averaged over a longer dura-

tion [28]. Despite these improvements, these techniques still face challenges in extracting dynamic information from rapidly moving, especially turbulent, systems. Therefore, techniques producing information on shorter timescales are required such that the dynamic properties of a system may be investigated.

In contrast to PET imaging, PEPT makes use of a single solid tracer particle which is tracked over time, requiring few LORs to determine its position at 10 - 250 kHz rates in typical systems. Tracer positions are determined in PEPT through the use of several possible algorithms, but primarily through the use of an iterative minimisation approach described below, in which a single position with uncertainty is typically computed with fewer than 250 LORs, and hence at sub-millisecond intervals for sufficiently large coincidence rates. For example, the achievable coincidence rates of the HR++ system (4 MHz) enable kilohertz location rates in PEPT reconstruction.

Through the use of tracer particles that are representative of the bulk material within a system, PEPT becomes a Lagrangian technique in which system behaviour over long timescales can be inferred from average tracer motion, while dynamic properties of the system can be determined from tracer motion on short timescales.

1.2.1 PEPT algorithms

In an ideal world, it could be assumed that all annihilation events would originate at the position of a point-like tracer particle, with corresponding annihilation photons emitted back-to-back generating straight-line LORs. In this case, all LORs would intersect at the position of the tracer, and the intersection could be used to track the tracer position exactly throughout the system.

However, several physical limitations introduce complexity into position reconstruction. The size of the tracer particle and the positron range following decay impact the position of annihilation in relation to the centre of the tracer. Annihilation acollinearity and the spatial resolution of the detector can also spatially offset the measured LOR such that it does not exactly intersect the annihilation position. More limiting however is the detection of false coincidences, discussed below, generating LORs that are not representative of the tracer position, significantly skewing measured positions. Additionally, a loss of events caused by attenuation or, at high detection rates, singles deadtime leads to a loss of true coincidences.

To handle these additional complexities in tracer position reconstruction, algorithmic methods are used to reduce the uncertainty of measured positions through the exclusion of corrupt events in reconstruction. The earliest and most widely used PEPT algorithm is the Birmingham method, described below, but many others exist, including those with extensions to multiple tracer tracking, each with their own strengths and weaknesses [21].

Event types

Alongside physical limitations in the detection of LORs, the existence of false coincidence events, which can be separated into different event categories, adds additional complexity to the calculation of measured positions.

Before considering false coincidences, a true coincidence event is defined by a pair of photons detected in time coincidence which correspond to a single annihilation event

originating from the tracer particle. When used in reconstruction, true coincidences generate true LORs related to the position of the tracer, at rates proportional to the activity of the tracer particle and the absolute efficiency of the detector system.

False coincidences are coincidence events which do not represent the trajectory of the tracer particle in reconstruction. These can be either scattered coincidences, in which one or both of the coincident photons scatter before detection, or random coincidences. Random coincidences occur when one or both of the detected photons do not originate from the same annihilation event within the tracer, or from the tracer at all in the case of a background detection. The random coincidence rate therefore increases with tracer activity and system absolute efficiency more rapidly than the true coincidence rate, as random coincidences can originate from multiple annihilation events. However, since random coincidences are expected to be distributed approximately uniformly in time, the use of a short coincidence window significantly reduces random coincidences in favour of true coincidences. These event types are demonstrated in Figure 1.3.

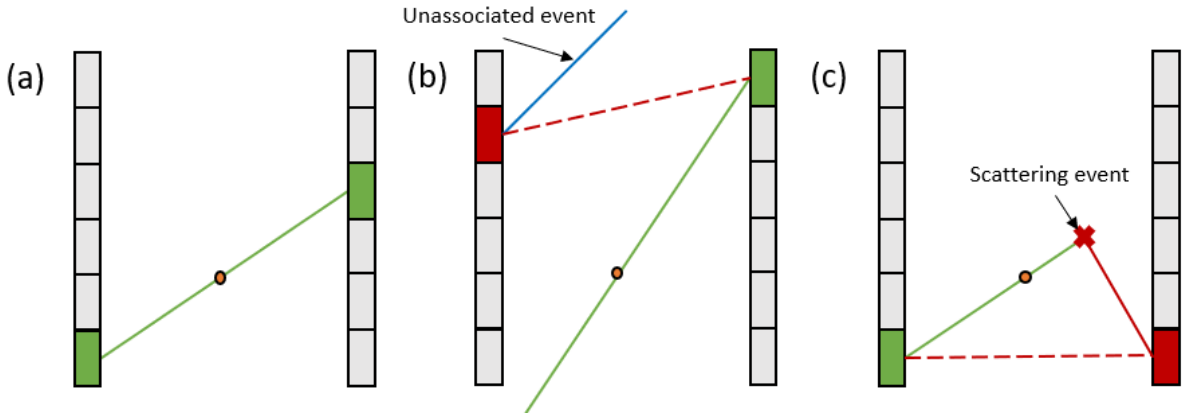

Figure 1.3: A tracer particle, shown as an orange circle, placed in an arbitrary block detector system showing true (a), random (b) and scattered coincidence (c) events. Annihilation photons arising from the tracer are shown as green lines and detector blocks are coloured green where these photons are correctly detected. Where a random or scattered photon is detected the associated block is coloured red, with a dotted red line showing the measured corrupt LOR.

When coincidence events are reconstructed into LORs, true and corrupt LORs are generated in a ratio determined by physical system parameters, with the coincidence rate therefore consisting of the sum of both true and false coincidence rates. PEPT algorithms are used at this stage to select only the true LORs for reconstruction, utilising the fact that random coincidences are approximately uniformly distributed in space to determine the tracer's location in a form of clustering approaches, providing an accurate representation of the trajectory of the tracer.

The Birmingham method

The Birmingham method, developed in 1993 at the University of Birmingham [11], is an iterative minimisation algorithm designed to optimally select only true LORs for position reconstruction. As mentioned, several alternative algorithms have become available

since 2012 [21], beginning with the development of the line-density method, however the Birmingham method remains the primary algorithm in use today.

Considering a measurement of an arbitrary number of time-consecutive LORs, a sample set S of N LORs ($N(S) = N$) are selected and the minimum distance point m_S is calculated. m_S is defined as the point in 3D space which minimises the sum D of perpendicular distances δ_i from each LOR, i, to a point (x, y, z), and can be described by $D_S(x, y, z) = \sum_S \delta_i(x, y, z)$, with m_S given as the solution to $\nabla D(x, y, z) = 0$.

After calculating m_S as above, the mean deviation d of each LOR in S is calculated as $d(S) = \frac{D(m_S)}{N(S)}$ and LORs with $\delta_i(m_S) > kd(S)$ are discarded to form a subset S_1 of $N(S_1)$ LORs. The parameter k determines how many events are discarded per iteration, with optimal values lying between 1 and 1.5 [11] and a typical operating value of 1.2 at PEPT Cape Town.

A more accurate minimum distance point m_{S_1} and smaller mean deviation $d(S_1)$ are then calculated on S_1. To avoid discarding LORs which may now be closer to the improved m_{S_1}, S is used such that any LOR in S with $\delta_i(m_{S_1}) > kd(S_1)$ is discarded to form S_2. This process is repeated until a fraction f of events remain to form a subset S_f, i.e. $N(S_f) = fN(S)$. As the remaining events, $fN(S)$, are presumed to be exclusively true coincidence events, the fraction f serves as an estimate of the expected proportion of true coincidences, with an optimal value f_{opt} determined by physical characteristics of both the detector systems in use and the experimental media itself [29]. With a single detector system, f_{opt} varies between experimental setups with the amount of scattering and absorbing material present in the system FOV [30], as a respective increase in scattered coincidences and loss of true coincidences naturally reduces f_{opt}. Without scattering or absorbing material present in the FOV, i.e. a bare source at a given activity, the value of f_{opt} is determined by the detector system's ability to measure true coincidences and discriminate against false coincidences. This is primarily determined by the system absolute efficiency, timing resolution and energy resolution. Improved absolute efficiency implies that true and random coincidence rates are increased, with true coincidence rates typically growing faster than random coincidence rates. Improved timing resolution implies that shorter coincidence windows may be used, minimising the detection of random coincidences. Improved energy resolution implies that narrower energy windows may be used, reducing the detection of scattered and random coincidences.

To ensure convergence, if no LORs are removed between iterations the LOR with the greatest δ_i is removed. If too many LORs are removed between iterations, i.e. if $N(S_n) < fN(S)$, LORs with the closest δ_i are added to S_n until convergence is satisfied.

Therefore, following iteration and convergence, a subset S_f is selected such that $N(S_f) = fN(S)$ and the mean distance point m_{S_f} is defined as the position of the tracer with location uncertainty $d(S_f)$. Since each LOR is measured at separate times t_i, the location is allocated a timestamp corresponding to the mean of t_i in S_f.

For clarity, the above iterative process is demonstrated for a simple selection of LORs in an arbitrary system in Figure 1.4.

Parameter optimisation

Since several adjustable parameters exist within the Birmingham method with a direct impact on the location uncertainty and rate of measured PEPT locations, an important

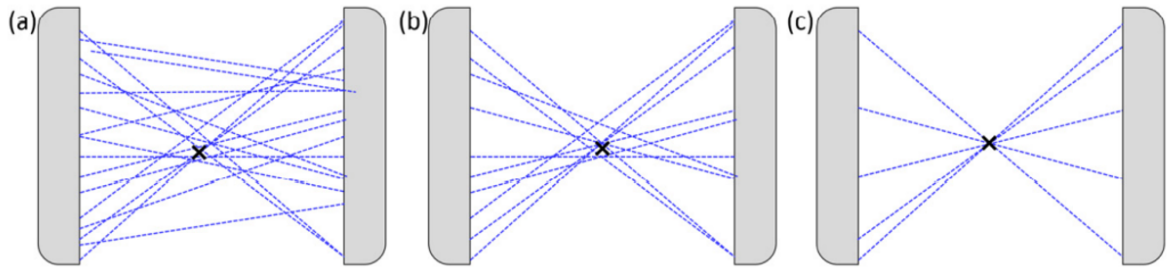

Figure 1.4: A simple example of the Birmingham method for 15 initial LORs and an f value of 0.33, reprinted from [31]. The initial sample of 15 LORs is shown in (a), with an intermediate step in (b) and the final subset of five LORs in (c). At each step, the minimum distance point is shown as a cross.

first step in experimental analysis is parameter optimisation. Typically the k parameter is treated as fixed as only the rate of convergence is affected, leaving the initial number of LORs used per location N and the fraction of true LORs used f variable.

The value of f_{opt} varies significantly between detector systems and experimental setups, ranging from 10% to 30% for earlier systems [11, 30], to 70% for newer systems at PEPT Cape Town [32], to between 90% and 95% for small semiconductor systems [1]. The observed increases of f_{opt} are the result of consistent improvements to detector technology. From the initial MWPC system to the modern BGO scintillator devices, detection efficiency, energy and timing resolutions have improved, allowing improved discrimination against false coincidences as described above. In the case of semiconductor devices, system efficiency and timing resolution are poor in comparison to the scintillators, but order of magnitude improvements to the energy resolution significantly reduce the detection of scattered and background events in favour of true annihilation events. In addition, systems are typically small-scale, so minimal attenuation and scattering is observed, and low-activity tracer particles are used, further reducing random coincidences.

In a typical optimisation process, a stationary tracer particle of experimentally representative activity is placed in the centre of a representative system and coincidence measurements are made, generating a large set of LORs. The Birmingham method is then applied to subsets of LORs with varying initial sizes of N and values of f, generating tracer positions over time. Since the tracer is stationary, the standard deviation $\sigma_{x,y,z}$ in each coordinate is determined, and the 3D standard deviation $\sigma = \sqrt{\sigma_x^2 + \sigma_y^2 + \sigma_z^2}$ is calculated and plotted against values of f, with separate curves plotted for different N values. These curves are typically U-shaped, with an expected proportionality to $\frac{1}{\sqrt{Nf}}$ and a minimum f_{opt} value for each curve with different N. This minimum is expected, as $f > f_{opt}$ implies that corrupt LORs are used in calculation, and $f < f_{opt}$ implies a reduction in statistics.

As N is increased, these U-shaped curves are shifted downwards, i.e. the achievable uncertainty for each value of f is reduced. This isn't unexpected as the measured fraction of corrupt LORs is unchanged and the inclusion of more LORs per location will naturally provide a more precise representation of the position of a stationary particle. However, for low event rate systems, larger values of N may use LORs measured with large time differences in the reconstruction of a single position, leading to low location rates and

poor accuracy in the case of moving particles.

These trade-offs need to be accounted for with every PEPT system and experimental setup, and optimisation can be performed towards experimental requirements. For example, in micro-scale tracking, the goal of parameter optimisation is to achieve the lowest possible location uncertainty, while maintaining adequate location rates such that slow-moving systems can be accurately analysed. In other cases, such as fast-moving systems, location uncertainty may be partially sacrificed for superior location rates, such that system dynamics may be more accurately studied.

1.2.2 Tracer particles

Alongside the detector systems and algorithms that enable positron emission imaging, tracer particles play a crucial role in the capabilities of PEPT systems.

Radionuclide properties

As required for coincidence imaging, any tracer particle must consist of a proton-rich radionuclide which emits positrons as it decays. Since only the photons following positron annihilation are used for imaging purposes, a purely positron emitting radionuclide is desirable to reduce the detection of photons not arising from annihilation contributing to corrupt LORs and singles deadtime. For example, Na-22, a typical calibration source, produces both positrons and 1275 keV photons as it decays, whereas F-18 produces only positrons [33].

Short-lived isotopes are desirable as throughout an experimental process, or shortly thereafter, the tracer will decay to acceptable background levels, simplifying the safety requirements for radioisotope retrieval and disposal following any experimental work. In addition, a short half-life implies that higher activity may be loaded onto the tracer in comparison to an isotope with a longer half-life, maximising the event rates which in turn improves both the accuracy and precision of tracking. However, the half-life must be long enough to allow for suitable measurement time, which may vary with experimental requirements.

Several radionuclides satisfying these conditions exist, and only those currently in use or development at PEPT Cape Town are discussed further.

Typical radionuclide selection

In PET imaging, the radioisotope F-18 is typically used, being a pure positron emitter with a half-life of 109 minutes, suitable for experimental and clinical purposes. In a medical context, F-18 is substituted onto fluorodeoxyglucose (FDG) molecules to be used as glucose analogues. Typically, F-18 is produced at iThemba LABs for medical FDG production using O-18(p,n)F-18 reactions with an 11 MeV proton beam, however, this requires both beam time and enriched O-18 targets.

PEPT Cape Town typically makes use of Ga-68 tracer particles in experimental work, also being a pure positron emitting radioisotope with a half-life of approximately 68 minutes. Ga-68 is produced through the use of Ge-68/Ga-68 generators, removing the need for dedicated beam time in the production of each tracer. These generators are made

by iThemba LABs, with Ge-68 produced through ^{nat}Ga(p,xn)Ge-68 reactions on natural gallium using a 66 MeV proton beam from the Separated Sector Cyclotron (SSC), which is then loaded onto SnO_2 columns. Ge-68, with a half-life of approximately 271 days, decays slowly to Ga-68 which can be eluted as required for tracer radiochemical production.

While the use of Ga-68 tracers offers convenience from the use of iThemba LABs produced generators, the greater positron yield and lower positron range of F-18 has been demonstrated to yield improvements in both the spatial resolution and sensitivity of PET measurements [34], and as such work into the use of F-18 for PEPT is ongoing [35].

Tracer activation and labelling

Alongside the choice of radionuclide, the manner in which the tracer particle is radiolabelled is an important consideration. In PEPT measurements the tracer particle must be representative of the constituents of a system in both its physical (size, density, etc.) and chemical (hydrophobicity, solubility, etc.) properties, such that it can be inserted into the bulk media without disrupting the system and non-invasive measurements can be made. To produce the tracer, direct or indirect activation methods may be used. A selection of tracers produced at PEPT Cape Town is shown in Figure 1.5.

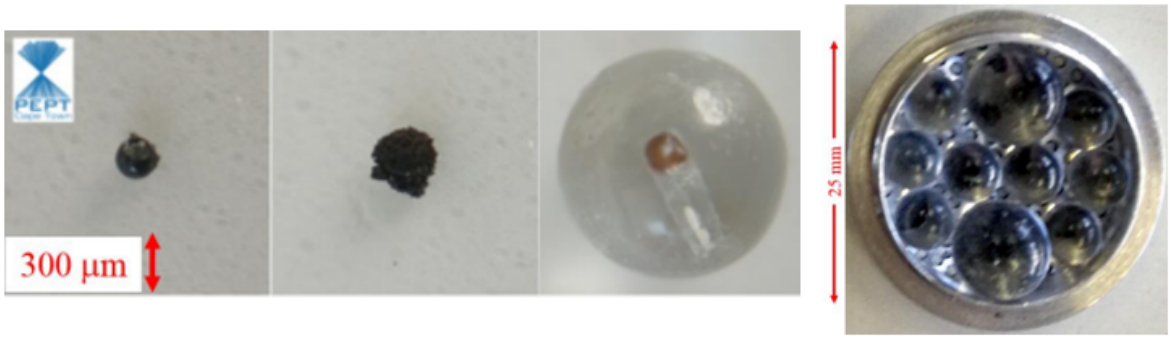

Figure 1.5: Tracers of various sizes, produced at PEPT Cape Town [35] using various techniques. From left to right, these are a moulded and density-modified tracer, a mineral-coated tracer, a glass bead with an ion-exchange inset and SiO_2 glass beads. Image scales are shown separately for the first three tracer particles and the glass beads.

Direct activation of a tracer involves extracting an original particle of a system and irradiating it to produce a suitable positron emitting radioisotope within the particle. This is typically achieved using proton beams on O-18 enriched targets, or He-3 beams on natural oxygen bearing targets to produce F-18 [21], but the use of high energy alpha particle beams has been investigated for use at PEPT Cape Town [35].

Direct activation is a particularly useful technique as tracer representation of the bulk system is ensured, and activity of > 100 MBq with a millimetre-sized tracer particle has been achieved [36]. However, for micro-scale applications, the size of the tracer impacts the scale at which tracking can be used to study systems. For a tracer of 1 mm size, phenomena at the micro-scale will be obscured. Therefore, indirect activation methods are typically used to produce micro-scale tracer particles.

Two primary options for indirect activation exist, being ion exchange and surface labelling. In ion exchange radiolabelling, atoms of a suitable material are replaced with those of a radionuclide of choice, typically within an ion exchange resin. With this method, tracers have been produced with sizes ranging from 50 µm to 1.2 mm, with maximal activities ranging from 600 kBq for the 50 µm tracer [37] to $>$ 37 MBq for the larger tracers. However, these resins may not be representative of bulk properties, being naturally hydrophilic, and surface labelling, in which a tracer is coated with the suitable radionuclide, has been shown to offer improvements in tracer representation. At PEPT Cape Town surface labelling has been used to produce tracers of approximately 22 MBq within size ranges of 0.1 to 1 mm [35], whereas at King's College London 1 µm particles have been coated with Ga-68 for PEPT use [21].

1.3 PEPT spatial resolution

For any PEPT system, the spatial resolution, or positional uncertainty with which a tracer particle can be located, plays a crucial role in the achievable quality of trajectory analysis. If the positional uncertainty is too large, with bounds that may vary depending on experimental requirements, it may be difficult or impossible to extract parameters from the system, such as the tracer velocity or acceleration, or even simply the trajectory of the tracer, to the precision required for meaningful analysis.

For micro-scale systems, this location uncertainty is critical, as the spatial scale of the phenomena being measured in micro-scale experiments is exceeded by the typically achievable location uncertainty of existing PEPT setups. Therefore, an understanding of the spatial resolution of a PEPT system is required to make improvements enabling the study of micro-scale phenomena with the required precision.

The spatial resolution of a PEPT system is described through the 3D location uncertainty $u(\bar{P})$ as:

$$u(\bar{P}) = \frac{w}{\sqrt{fN}} = \frac{w}{\sqrt{T}},$$

where w is the spatial resolution of the positron camera and N is the initial set of measured LORs used to produce the location. When this initial set N is reduced to only true LORs through the use of the fraction f, the true coincidence rate T is produced [2]. To improve upon the PEPT spatial resolution, clearly w must decrease or T must increase, and changes to both the choice of tracer and detector system can provide these improvements.

To reduce w, the effects of tracer choice on the corresponding PET spatial resolution can be considered, being positron range and annihilation photon acollinearity. Positron range and acollinearity effects are typically tied directly to the choice of radionuclide, determined by the positron endpoint energy. These effects can be reduced for a given nuclide [38, 39], although this is impractical for PEPT experiments, and the use of alternative tracer particles was considered to be out of scope for this work. On the detector side, reducing the pixel size can reduce w, up until the point at which the range and acollinearity tracer effects dominate positional uncertainties. At this point, the fundamental limit for PET spatial resolution is reached, and as such detector systems with smaller pixel sizes than this limit are not manufactured.

Enhancing T requires improving the true coincidence rate, which can be achieved by increasing the activity of the tracer particle. In the case of a small tracer particle, especially at the micro-scale, the amount of radioactive material that can be loaded is limited, which places an upper bound on achievable activity. For a larger tracer particle, greater activities are possible. However, the true coincidence rate scales linearly with activity, whereas the random coincidence rate scales as the square of activity [40], reducing the signal-to-noise ratio with increasing activity. In addition, an upper limit on event rates may be imposed by deadtime effects, further limiting useful tracer activity. Therefore, investigation into the optimal tracer activity is required to place limits on the achievable spatial resolution improvements through tracer optimisation, and is described for future investigation in Section 6.2.2.

Alternatively, an increase in the absolute efficiency of a detector system can lead to improvements in T. The absolute efficiency is determined in part by the detector materials used (intrinsic efficiency), but also by its associated geometry (geometric efficiency). An increase in the intrinsic efficiency of a detector system involves the use of alternative detector materials, typically involving the development or purchase of an entirely new detection system. An increase in the geometric efficiency involves an increase in the solid angle subtended by the detectors, typically achieved by placing more detectors surrounding a system of interest, or by placing them closer to the centre of the FOV of the system.

Previous instrumentation developments [1] have focused on the minimisation of w, making use of semiconductor devices, namely the Polaris system, to achieve significant reductions of the achievable PEPT location uncertainty. The Polaris system offers a small pixel size, and therefore an extremely low w in comparison to conventional PET/PEPT systems. However, the efficiency of this system is consequently poor, limiting the achievable coincidence rate in comparison to conventional systems, negatively impacting both the system spatial resolution through T as well as the achievable location rates. A system that can achieve an improvement in the PEPT location uncertainty while maintaining a useful location rate is desirable, although challenging to accomplish with a single existing detector system. This work focuses on the use of a secondary scintillator system designed to make improvements on the true coincidence rate, which, when combined in a hybrid camera with the semiconductor system, will lead to an overall improvement in the PEPT spatial resolution while maintaining desirable location rates.

Chapter 2

Equipment

2.1 Semiconductor detectors

Within a semiconducting detection material, ionising radiation produces electron-hole pairs, which are separated by an applied voltage and collected at an anode and cathode. The total charge produced by the interaction is proportional to the energy of the incident radiation, and through the system electronics the produced voltage pulses are translated into events with characteristics such as energy, time and position.

One of the primary benefits of using a semiconductor detector is that many more information carriers, being electron-hole pairs in semiconductors as opposed to photons in scintillators, are produced for a given interaction, reducing the effects of statistical fluctuations in their production, improving upon the energy resolution [41]. An improved energy resolution enables the use of a narrow energy window in event discrimination, reducing the contribution of scattered coincidences in favour of true coincidences. Additionally, semiconductor detectors typically have compact overall and pixel sizes, which contributes favourably to the spatial resolution of a detector system.

However, semiconductor systems generally have lower intrinsic efficiency, overall size, and timing resolution compared to scintillators. These result in a reduced detection rate and an increased random coincidence rate as a result of a necessarily larger coincidence window. The negative impact of these factors on PEPT spatial resolution is discussed in Section 1.3, introducing a trade-off that influences design decisions.

2.1.1 Polaris system

UCT owns the PolarisJ system manufactured by H3D Inc., shown in Figure 2.1 as a pair of pixelated room-temperature CZT semiconductor detectors. Each module contains two $20 \times 20 \times 10$ mm^3 CZT crystals, making use of a pixelated anode array and depth of interaction information to segment each crystal into $11 \times 11 \times 20$ pixels of $1.8 \times 1.8 \times 0.5$ mm^3, giving a total of 9680 individual detector elements. These modules are placed approximately 60 mm apart in typical operations, providing a FOV of $60 \times 42 \times 20$ mm^3.

Detected singles events are stored in list mode format. This format includes information such as the number of interactions recorded within a 10 ns window of the first event, the module in which the interaction occurred, the energy deposited in keV, the

3D pixel coordinates in millimetres, and the timestamp in 10s of nanoseconds. The number of interactions is typically used for scattered detections, where multiple interactions of a single incoming photon are recorded and summed to produce a single event. This stored information is then used in coincidence processing, where a 15 keV energy window around 511 keV, and a 600 ns coincidence window are typically applied for event discrimination [1], with the remaining events determining LOR endpoints through the measured pixel coordinates.

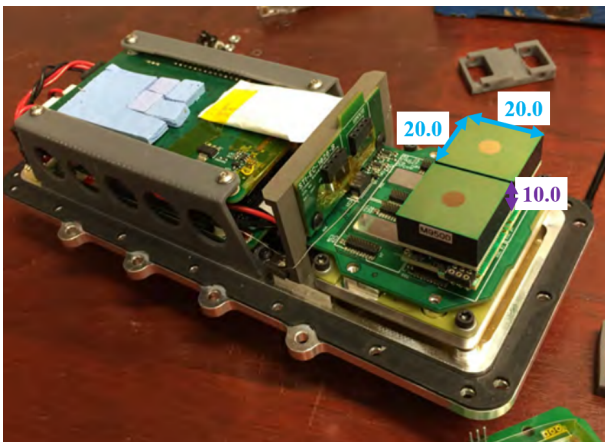

Figure 2.1: The internals of the PolarisJ module, showing the two CZT crystals as the green squares on the right, with dimensions given in mm.

Previous work with this system demonstrated its applicability to PEPT, achieving sub-millimetre tracking of low-activity tracer particles. An approximately 20 kBq stationary Na-22 calibration source was tracked to a location uncertainty of approximately 0.5 mm with a location rate of 0.27 Hz, whereas a stationary 1.1 MBq Ga-68 source was tracked to a location uncertainty of approximately 0.8 mm with a location rate of 11 Hz [1].

The achievable location uncertainties are promising for a micro-scale PEPT system, however the location rates are limiting. To study a moving tracer particle, its motion would need to be sufficiently slow and smooth such that dynamic information of the particle trajectory was not lost between consecutively determined locations. To extend the capabilities of this system to particles moving at speeds above the threshold for informative study, a system offering improved absolute efficiency and timing resolution is required, leading to the necessity of using scintillator systems.

2.2 Scintillator detectors

At UCT, parts are available for research purposes from scintillator-based PET scanners manufactured by Siemens; the decommissioned ECAT 951 scanner and spare components from the EXACT HR++ scanner currently used by PEPT Cape Town. The detector elements of these systems are comprised of scintillating BGO crystals. When struck by high-energy photons, ionising electrons are produced through either photoelectric absorption or Compton scattering, leading to the excitation of atoms within the crystal.

Following deexcitation photons are emitted (approximately 4200 at 511 keV), resulting in a light output that is generally proportional to the energy deposited by the initial photon. The emitted light exhibits a short decay time, enabling the production of fast signal pulses.

The recent development of a data acquisition system designed to interface with these detector elements positions them as optimal choices for the development of a scintillator array. However, detector elements from a lutetium oxyorthosilicate (LSO) detector system are currently being characterised and may be found to offer improved performance in future work [18].

The functional description of each part of the detection chain is outlined in the following sections.

2.2.1 Detector blocks

Both the 951 and HR+ detector systems make use of detector blocks, shown in Figure 2.2. At the front of each block is a scintillating BGO crystal which is segmented into 8 x 8 individual pixels. Four photomultiplier tubes (PMTs) are attached to the crystal of each block, converting the light signal produced through scintillation into a measurable electrical pulse through the use of a 1500 V bias voltage applied across the tube. The pulses from each PMT can then be used to determine in which pixel the photon interacted, as described in the following section, with the response of each crystal element being well-defined in terms of the pulses produced in each PMT. The sum of the pulses from all PMTs measures the total energy deposited in the block.

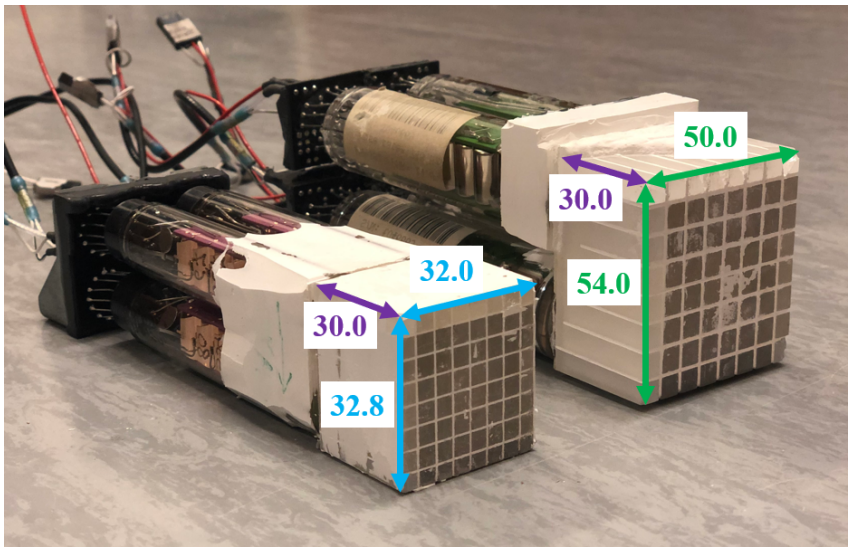

Figure 2.2: Detector blocks from the EXACT HR+ (left) and ECAT 951 (right) without their protective casing. In each block, four photomultiplier tubes and the 8 x 8 segmented BGO crystal can be seen, with dimensions given in mm.

The 951 detector block offers an intrinsic detection efficiency of approximately 55% at 511 keV [42], with the HR+ detector block offering a slightly improved 60% [18]. In

comparison, the Polaris system offers only 5-15% intrinsic efficiency [43], demonstrating the significant improvement in efficiency possible through the use of a BGO system.

Both the 951 and HR+ blocks have the same pixel count, but the 951 block is larger (pixel dimensions of $6.25 \times 6.75 \times 30$ mm^3) than the HR+ block (pixel dimensions of $4.1 \times 4.0 \times 30$ mm^3), implying a trade-off between the achievable spatial resolution and absolute efficiency by virtue of their pixel densities and overall sizes.

2.2.2 Module controllers

The module controller consists of the electronics required to process the signals from each detector block into digital events. A simplified schematic of the 951 detector module, along with a picture of a module controller, is shown in Figure 2.3.

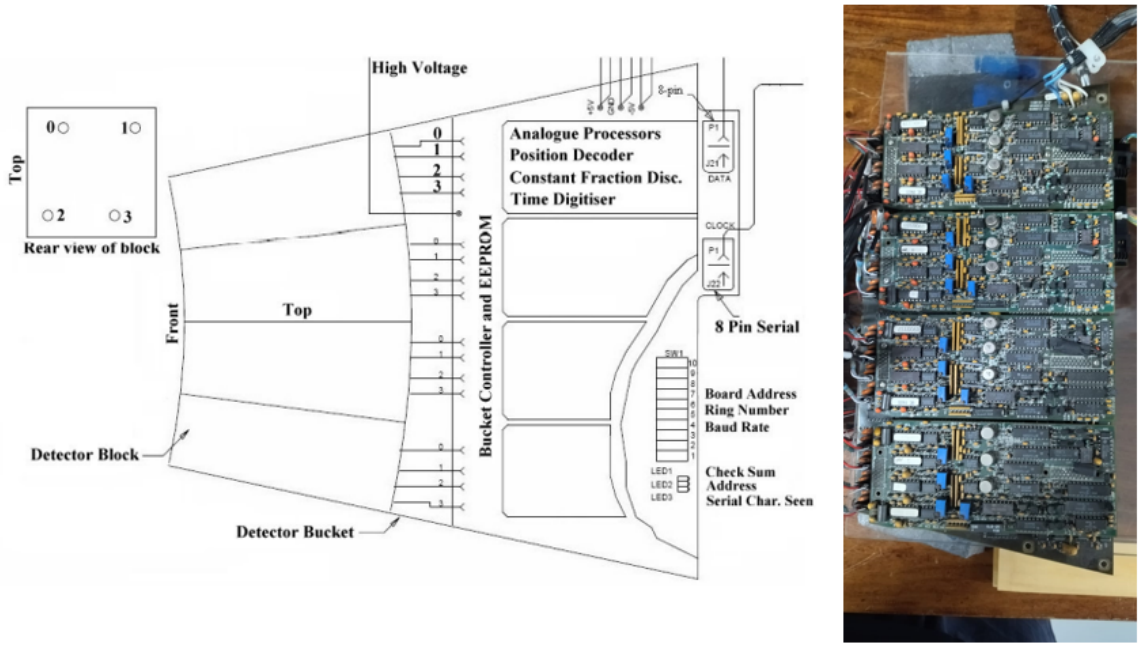

Figure 2.3: Simplified schematic of a 951 module [44] (left) and a top-down picture of the module controller (right).

Each module is connected via a serial connection to a master clock, producing synchronisation pulses at 32.5 MHz and strobe pulses at 1/8th of the clock frequency, approximately 4 MHz.

The 951 module controllers are capable of connecting to four detector blocks, and therefore 16 PMTs, providing each PMT with high voltage and retrieving signals from the same connection. The signal from each PMT is retrieved and passed through an analogue signal processor, first passing through variable gain amplifiers with gains that can be adjusted through a calibration procedure, followed by further amplification and smoothing.

Three different subsets of the amplified signals from each PMT are then summed into

three separate signals producing total, axial and transaxial energy signals:

$$\begin{aligned} \text{Total energy} &= \text{PMT } 0 + \text{PMT } 1 + \text{PMT } 2 + \text{PMT } 3 \\ \text{Axial energy} &= \text{PMT } 0 + \text{PMT } 1 \\ \text{Transaxial energy} &= \text{PMT } 0 + \text{PMT } 2 \end{aligned}$$

The total energy signal is sent to a constant fraction discriminator (CFD) which makes use of a precision time gate enabling energy integration and event time tagging at 2 ns precision.

Each energy signal is then digitised, and the transaxial and axial signals are passed through the position energy processor, containing a lookup table which takes both signals and determines the crystal position in which the event originated as two 3-bit values. The total energy signal is tested against variable energy discriminators, determining whether the event had valid energy for an annihilation event. Finally, event time is digitised into a 6-bit data word, producing the time in units of 4 ns since the last strobe pulse was received, thus giving a local time signal between modules.

The above signal processing steps are illustrated in Figure 2.4.

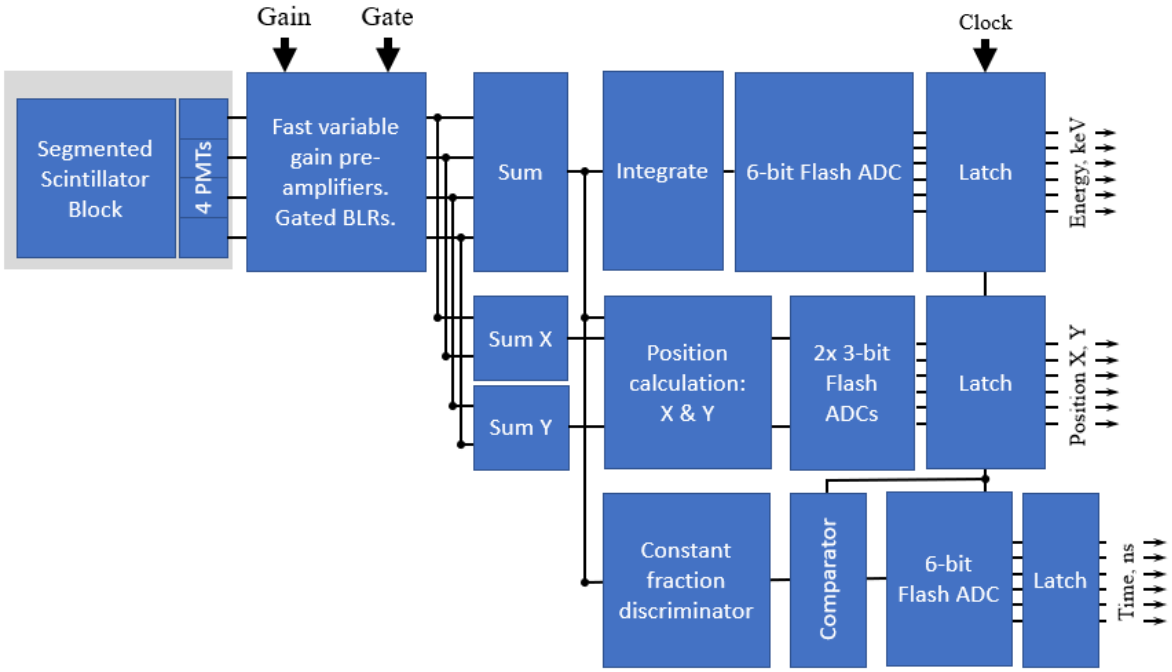

Figure 2.4: The detection and signal processing chain of a module controller, used in the computation of total energy deposition, interaction crystal coordinates and time of arrival for each singles event. Inputs of PMT gain, energy level discriminators (gate) and master clock synchronisation pulses are shown.

In addition to clock pulses, the serial connection serves to allow communication with each module, either through the sending of commands or receiving of data. This connection is useful in both calibration and troubleshooting with direct, fast access to each element of the detection system. For troubleshooting, the count rate of a block or set of

blocks can be accessed in the case of count rate issues, and full block histograms, detailing the number of events measured in each pixel of each block, can be used in the case of suspected PMT issues.

For calibration, the gain of each PMT can be individually adjusted, as well as energy discriminators and CFD values among others. To simplify this process, the 951 controller stores an automated calibration routine which may be used as a first step in block calibration. Firstly, each of the four PMT gains of a single block are iteratively adjusted to approach a uniform output from each crystal. Subsequently, position profiles are measured, identifying 64 peaks corresponding to each crystal within the block, so that row and column boundaries separating each crystal can be determined. Finally, individual crystal energy responses are investigated, allowing for the identification of the 511 keV peak enabling the controller to set optimal analogue-to-digital converter (ADC) energy discriminator values for each crystal.

Following the automated calibration procedure, a histogram of the block is used to determine its uniformity. By calculating the standard deviation of the counts in each pixel of a block, and comparing it to the uncertainty of the mean counts, the quality of the calibration can be determined. In the case of calibrations for this system, a standard deviation lower than the Poisson uncertainty of the mean indicated a sufficiently uniform response from the block, i.e. the block was successfully calibrated. If this condition was not met, a manual approach was taken to address noticeable issues in the histogram, such as manual gain adjustments or electronic adjustments, or the block was completely replaced.

The full PEPT data acquisition and control scheme as described above is illustrated in Figure 2.5, highlighting each component of the system, its role in PEPT measurement and the communication between components. The event data capture process is described in the following section.

2.2.3 Data acquisition

During acquisition, event data, containing digitised information about the time and crystal in which an event occurred, is streamed from each controller to a PC and acquired using an ADLINK PCI-7300A digital I/O card. These data take the form of two 8-bit data words, with one containing positional information and the other containing timing and additional event information.

To enable simultaneous acquisition, two bits from each controller are acquired in parallel at the clock frequency (32.5 MHz). These bits are separately reconstructed into 8-bit words for each module, with the end of each word given by a strobe pulse (1/8th of the clock frequency, approximately 4 MHz). This data acquisition mechanism accounts for acquisition deadtime effects, as all controllers simultaneously transmit data, as opposed to waiting for each controller to transmit a full word. In software, information identifying the module in which the event occurred, and the number of strobe pulses since the last event, are appended to these words to produce individual 32-bit words for each event, which are then stored for processing.

The data format of the stored events is shown in Figure 2.6. Bits 0-7 contain the 8-bit word of positional information, whereas bits 8-15 contain the 8-bit word of timing

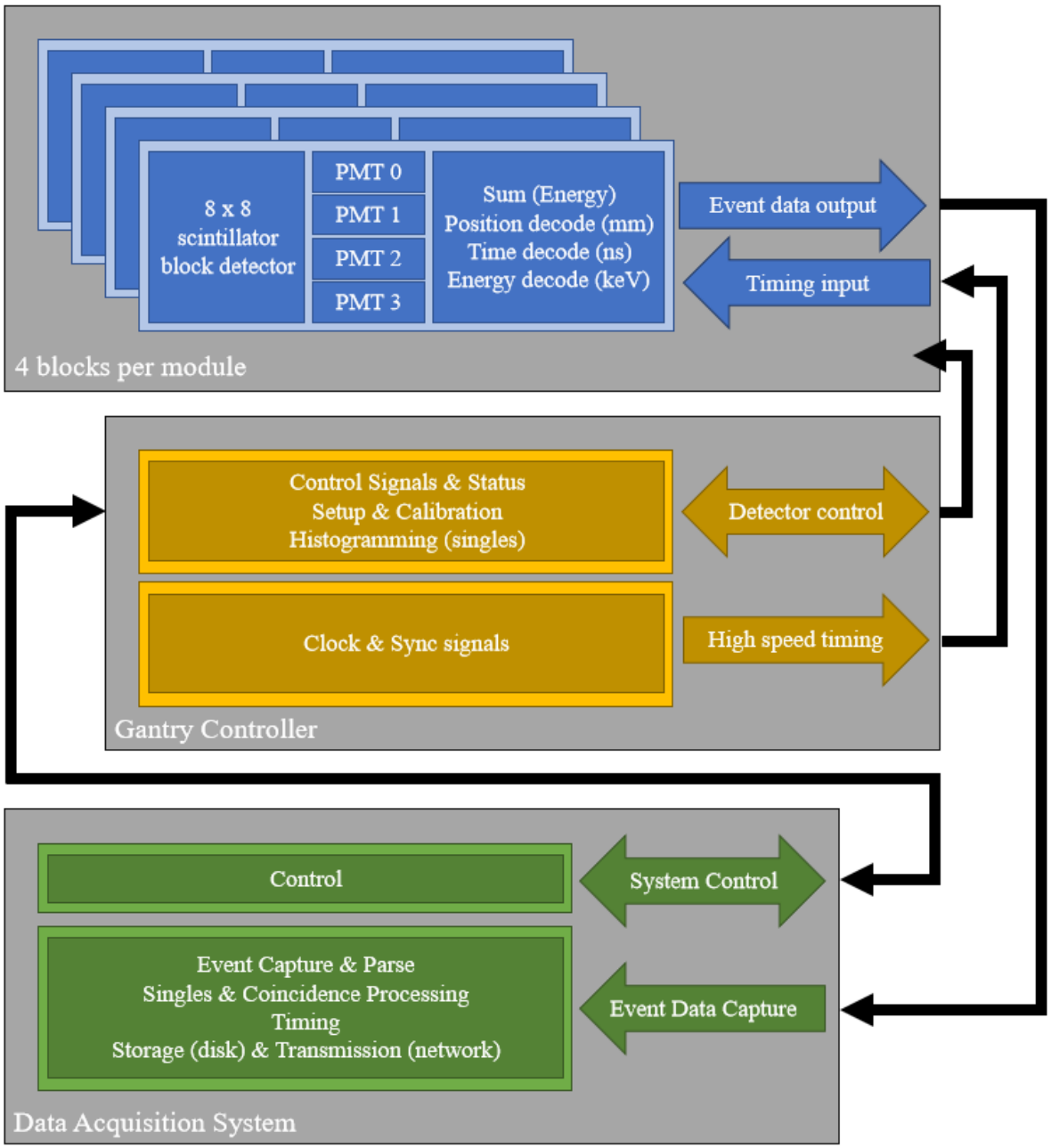

Figure 2.5: The PEPT data acquisition and control scheme. Detector modules as illustrated in Figure 2.4 are shown, outputting event data to the acquisition system, with timing signals input from the gantry controller. The gantry controller consists of the master clock and uses a serial connection to communicate with and control the detector modules. The data acquisition system is used to control the system and capture event data and is described in Section 2.2.3.

and additional event information, both read from the controller. The remaining bits are appended by the PC in acquisition as described above.

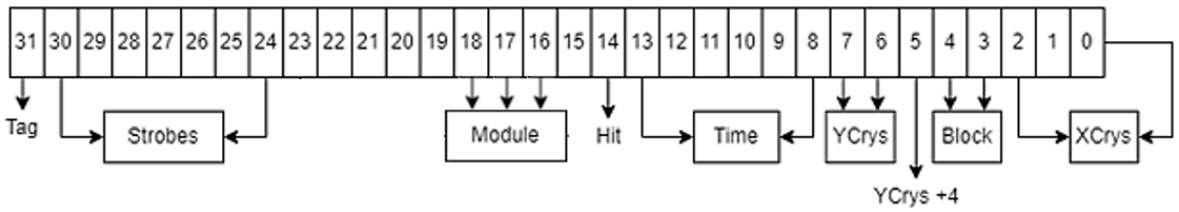

Figure 2.6: Data format of the stored 32-bit word representing a singles event. Each event is reconstructed from simultaneous, parallel acquisition from each module. Several bits used in timing events are currently unused in the storage of event data, but are available to increase the module and block capacity of the system.

The 'Tag' bit is used to distinguish between a detection event and a timing event. The timing events are written at the end of each data buffer, recording first a tagged marker, followed by the time since the start of acquisition in seconds and then the number of microseconds since the last second, both determined by the acquisition PC. The 'Hit' bit indicates whether an event was detected. If this bit and the 'Tag' bit are not set, the data word is discarded and no event is stored.

The 'Strobes' bits count the number of strobe pulses that have occurred since the last recorded event, resetting to zero following a detection event. The 'Time' bits give the time in units of 4 ns since the last strobe pulse at which the event was detected.

To determine in which crystal the event occurred, the 'Module' bits are used to identify the controller, the 'Block' bits to identify the block within the controller, and the 'Xcrys' and 'Ycrys' bits to identify the x and y coordinates of the crystal within the block in which an event occurred. The coordinates are represented as 3-bit values with a maximum value of 8, since the blocks have eight crystals along each dimension, but due to a legacy hardware issue the 'Ycrys' bits have been reorganised such that the most significant bit is placed instead in bit 5, requiring slight additional processing when extracting these values.

2.2.4 Data processing

After passing through the data acquisition of the previous section, individual events are stored on a PC in list mode with the format described in Figure 2.6. From this data, any analysis can be performed in software, such as generating heatmaps of the crystals in 3D space and conventional sinograms as used in PET imaging, which is a benefit of storing data in this way. However, the primary use case of this system is to perform PEPT tracking and this section will explain how the data is processed to enable this.

Firstly, custom C code is used in which several data structures and algorithms enable the identification of coincident events. Module controllers are defined as a structure in C, storing their position and orientation in the lab reference frame as sets of vectors. Additional parameters such as the number of blocks connected to each controller are stored, as well as a Boolean array defining which other modules a given module is in coincidence with. These arrays are required, as coincident modules are not taken into account in the list mode storage of singles event data, requiring software input when a system geometry is defined to determine which modules are in coincidence. This is

unconventional, as coincidence processing is typically performed in hardware, storing only coincidence events on disk. Here, all singles events are stored, with coincidence processing performed in software, enabling greater flexibility in processing. Detector blocks are also defined as a structure, with each block stored within its respective module and its position and orientation stored in the reference frame of the parent module. Additional block characteristics such as the number of crystals in each dimension, dimensions of the crystals and the block efficiency are also stored. The above structures are graphically represented in Figure 2.7.

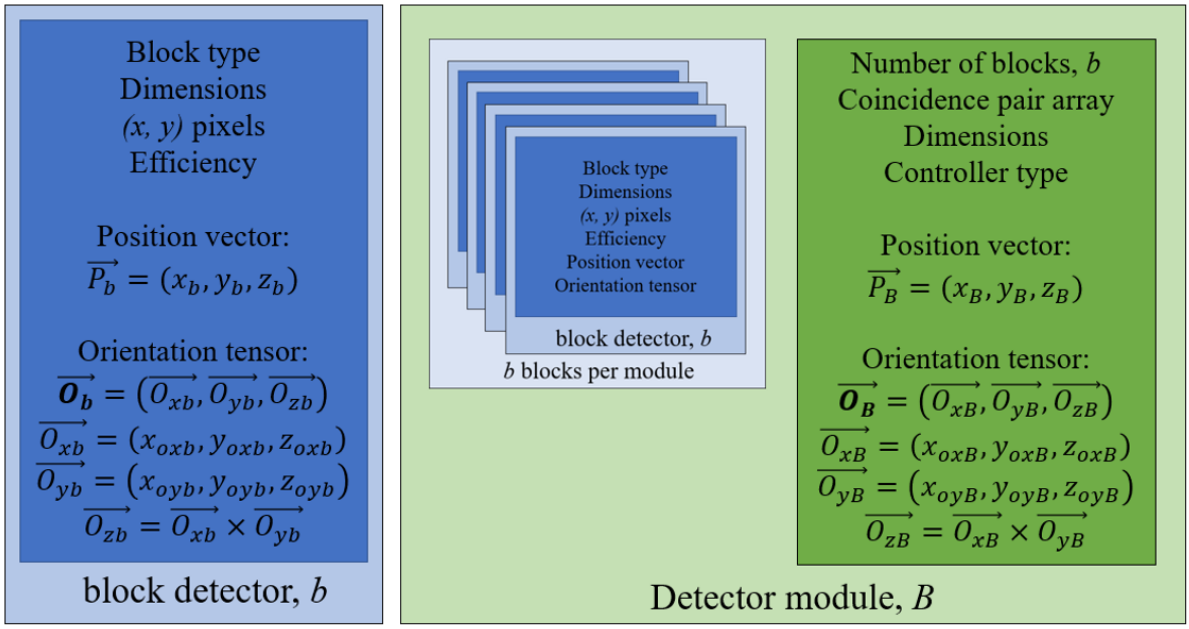

Figure 2.7: The contents of the block detector (left) and detector module (right) structures used in custom C code for coincidence processing. Each detector module, B, consists of several detector blocks, b, limited to four with the 951 controller system.

The module structures are then collected and stored within an overall camera structure, represented in Figure 2.8, and this defines the overall camera geometry and its components which are used to determine the position and timing of events.

Events are processed individually in the order of time of arrival and the PEPT algorithm makes use of a first in first out buffer, i.e. only the latest event from each module is considered in coincidence processing.

Since the strobe pulse is received approximately every 256 ns, which is much larger than a typical coincidence window for a BGO PEPT system, events arriving from different strobes are not considered in coincidence processing. This does discard potentially valid events from consecutive strobes, but with a narrow coincidence window the fraction of events discarded in this way is expected to be small. Since the events are time ordered, a non-zero strobe value in an event discards all previous events from processing, ensuring that events from different strobes cannot be in coincidence, requiring only the testing of the event time.

If an event arrives within the same strobe as another event, the pair of events are tested against both the predefined coincidence window, as well as the coincidence Boolean

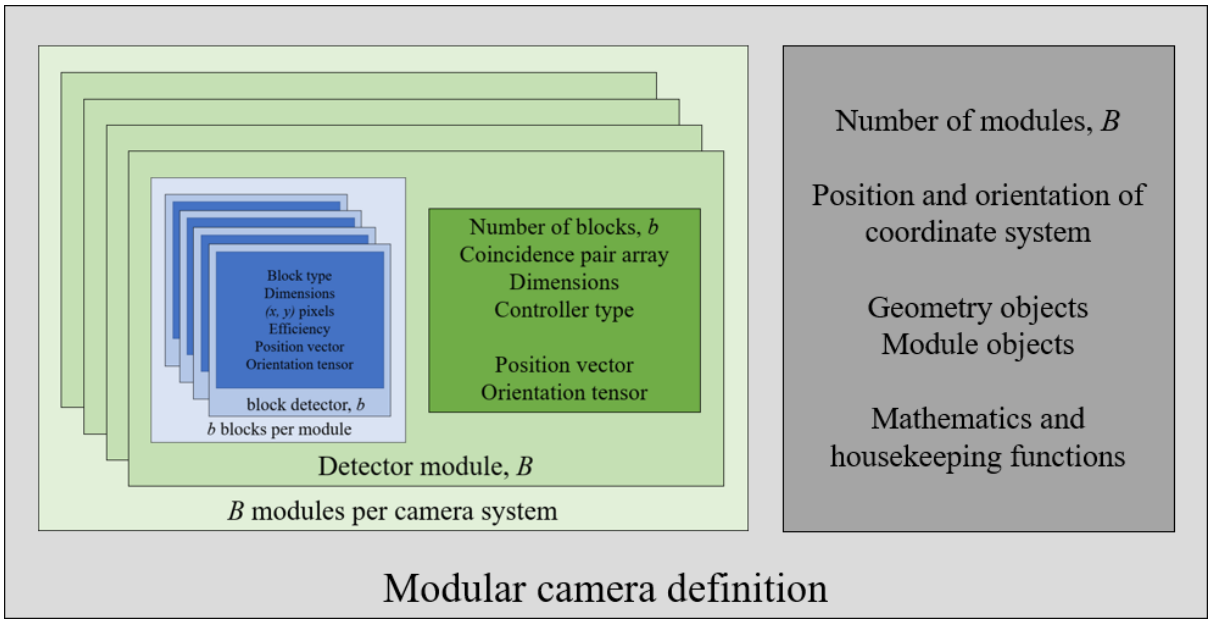

Figure 2.8: The contents of the modular camera structure used to contain the entire geometry of the detection system for coincidence processing. The nested block-module structure is demonstrated.

array from their corresponding modules to determine whether they were detected as valid coincidence events. If events are detected in two coincident modules within a strobe pulse, and the timing conditions are satisfied, a coincident event has occurred and an LOR is created as the vector joining the two event positions in 3D space using the geometry definition of the module and block structures. This LOR is then passed to the PEPT algorithm and the tracer position is found as described in Section 1.2.1.

2.3 Calibration sources

To perform calibration of the detector blocks, as well as analyses not requiring high tracer activity, calibration sources were used. At UCT, a Spectrum Techniques calibration kit [45] is available for such purposes, consisting of a selection of gamma-emitting radioisotopes. Each source from this kit features an active diameter of approximately 3 mm and a height of less than 1 mm positioned centrally within a larger plastic disc.

The positron emitter Na-22 from this kit was used to perform detector block calibration and resolution characterisation, as well as sensitivity profile measurements. In addition, the Cs-137 and Co-60 sources were used in the energy calibration of the BGO detector blocks and the Polaris system. Each source was manufactured with an initial activity of 1 µCi, reported to a precision of 20%, in October 2020 with an assumed time precision of 1 month. In the case of Cs-137 and Co-60, knowledge of the source activity was not required in analysis, however, to perform sensitivity measurements the activity of the Na-22 source needed to be measured to higher precision.

Na-22 has a half-life of approximately 2.6 years. Using nuclear decay data the activity of the source at time of use (July 2023) can be estimated to be $A = 17.8 \pm 3.6$ kBq. To

confirm this expectation and improve upon the uncertainty limits, the activity of the source was measured using coincidence techniques.

Detector response

The expected singles rate r_s in a given detector, sensitive to one emission energy range only, is given by the product of emission ($A\gamma$) and detection (ϵ_{abs}) probabilities as:

$$r_s = A\gamma\epsilon_{abs},$$

with source activity A, emission branching ratio γ and detector absolute efficiency ϵ_{abs}.

To perform coincidence measurement two detectors are used, arbitrarily selecting detector 1 to detect the Na-22 1275 keV photon only and detector 2 the 511 keV annihilation photon only. Assuming the Compton scattered detections of the 1275 keV photon in detector 2 to be negligible, the coincidence rate r_c can be determined as the product of the detection probabilities, $\epsilon_1\epsilon_2$, with the probability of each emission, as well as the probability that the emissions are coincident. In the case of Na-22, these probabilities are independent, and the probability that the emissions are coincident is given by $\gamma_c = \gamma_1\gamma_2$. Therefore, the coincidence rate can be written as:

$$r_c = A\gamma_1\epsilon_1\gamma_2\epsilon_2\gamma_c = A\gamma_1^2\epsilon_1\gamma_2^2\epsilon_2$$

Rearranging the above to remove the unknown efficiency terms, the activity of the source can therefore be determined through measurement of the true coincidence rate r_c and the background corrected singles rates of each emission $r_{1,2}$ as:

$$A = \frac{r_1 r_2}{r_c}(\gamma_1\gamma_2),$$

with branching ratios of $\gamma_1 = 0.9994$ and $\gamma_2 = 0.8996$ for the Na-22 1275 keV and 511 keV emissions respectively [33].

Measurement

The above activity formula consists only of true singles and coincidence rate terms. However, in measurement with a real detector system, background events and random coincidences contribute to the detected rates. As these events arise from unrelated sources, or different annihilation events within the same source, they should not be included in activity calculations and must be corrected for. Deadtime effects were assumed to be negligible as the source activity was low and were therefore not accounted for.

In the singles rates, each detector is sensitive to background events from natural radioisotopic sources, cosmic rays, as well as emissions from surrounding laboratories, which may fall into the same energy ranges as the emissions under study. Therefore, these background event rates need to be measured to determine the true singles rates in each detector.

Assuming M measured singles events over time T_M with the source present, and B measured background events over time T_B, the corrected singles rate r_s can be expressed as:

$$r_s = \frac{M}{T_M} - \frac{B}{T_B},$$

with uncertainty propagating as:

$$u(r_s) = \sqrt{\frac{M}{T_M^2} + \frac{B}{T_B^2}},$$

assuming the fractional uncertainty of measurement time to be negligible, as well as assuming that all counting measurements follow a Poisson $\sqrt{N}$ uncertainty.

Since a coincidence gate is used to determine the coincidence rate, random coincidences need to be accounted for. This is achieved through the use of a delayed coincidence measurement, in which one arm of the coincidence circuit is delayed in time such that any coincidences measured are guaranteed to be random. Therefore, for measured P prompt and D delayed coincidences over time T_c, the true coincidence rate can be expressed as:

$$r_c = \frac{P - D}{T_c} = r_P - r_D,$$

with uncertainty propagating as:

$$u(r_c) = \frac{1}{T_c}\sqrt{P + D},$$

again assuming a Poisson $\sqrt{N}$ uncertainty.

To perform these measurements, two NaI detectors were placed at a 90° angle to one another, with a Na-22 source placed equidistant to each. At 180°, the detection of a 511 keV photon in one detector geometrically necessitates the second annihilation photon striking the opposing detector, with negligible acollinearity considerations. Consequently, the second 511 keV photon has a probability of depositing some or all of its energy concurrently with the detection of the 1275 keV photon, possibly summing to produce an event with energy above the accepted upper level. This results in a reduced, inaccurate coincidence rate measurement, leading to inaccuracies in the activity calculation. Therefore, a 90° configuration was used to ensure that both annihilation photons could not simultaneously strike both detectors, enabling accurate measurements of the coincidence rate.

Each detector was connected to NIM pre-amplifier and amplifier systems, as seen in Figure 2.9. The amplified signals from each detector were sent to single channel analysers gated separately on the 1275 keV and 511 keV annihilation emissions from Na-22, using window sizes such that the entire photopeak was encompassed. Singles events from each detector were separately counted and simultaneously sent to two coincidence units to measure the prompt and delayed coincidence rates. To measure the delayed coincidences, a gate and delay generator was used to add a large delay to the signal from one of the detectors before being sent to the second coincidence unit, ensuring that while all prompt coincidences were measured in the first unit, only random coincidences would be measured in the second.

From this setup, singles events from each detector were counted, along with the prompt and delayed coincidences. These values were measured for both the background and the Na-22 source several times. From these measurements, and the activity formula determined above, a weighted mean activity of the Na-22 calibration source was determined to be 20.11 ± 0.26 kBq on 24 July 2023, agreeing with the estimated value of 17.8 ± 3.6 kBq whilst improving the measurement precision from 20% to 1.3%.

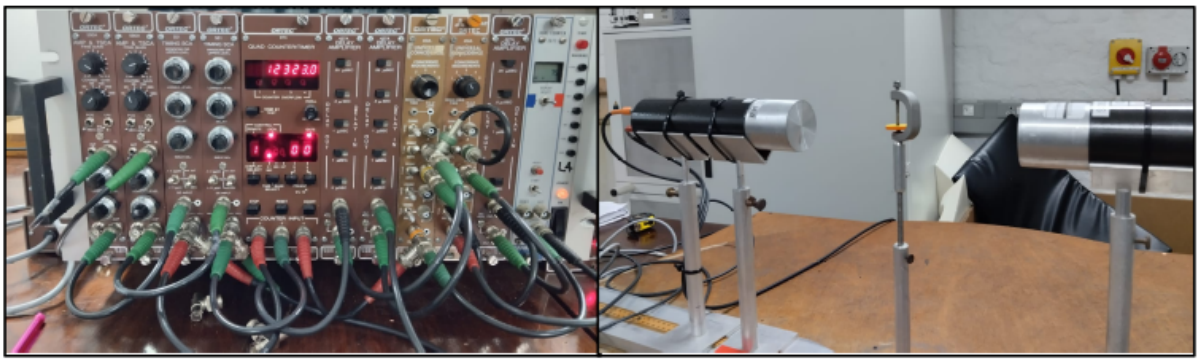

Figure 2.9: The two NaI detectors (right) and electronics (left) used to measure the activity of the Na-22 calibration source. The detectors were positioned at 180° for the clarity of this image; in measurement one detector was rotated by 90° as discussed.

2.4 Anet A8

For characterization purposes, precise and reproducible positioning of tracer particles within the system FOV was essential. To achieve this, a 2D motion stage was used to both hold and move the calibration sources used in characterisation through a selection of precise positions with the use of custom-written code. This motion stage was developed through the modification of a 3D printer, chosen to be the Anet A8 as it required minimal modification after use in previous work [1]. The Anet spatial resolution is quoted at ±200 µm, determining the precision of tracer particle positioning in characterisation. The effect of the Anet spatial resolution is discussed further in Section 5.1.

Since motion along the printer's y-axis is achieved through the motion of the print bed, ordinarily shifting the location where the printing occurs as opposed to the position of the head itself, motion in this direction was not useful for tracer positioning as, unlike in previous work, the 16 detector blocks could not be placed on the bed. Therefore, the print bed was removed from the printer and the Anet was placed face down on a custom-built stand, shown in Figure 2.10, used to raise it above the detector units, addressing only horizontal planes. The source holder, consisting of threaded rods attached to a 3D printed base, was therefore adjustable in terms of its height, allowing for the mapping of different planes.

To control the printer, Python code was written to produce G-code scripts that moved the print head in well-defined motions. These scripts were then uploaded to the printer directly through the Octoprint network interface via a USB connection.

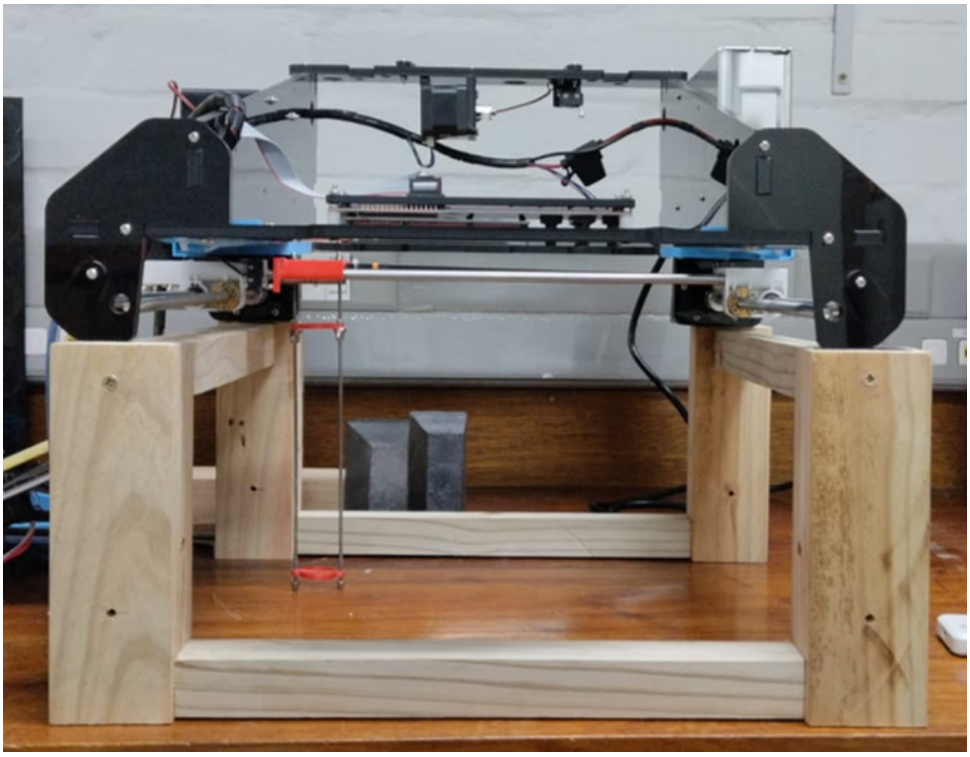

Figure 2.10: The Anet A8 placed face down on a custom-built wooden stand. The source holder (threaded rods with red discs attached) is positioned so that the tracer may be moved in horizontal planes throughout the central FOV.

Chapter 3

Component characterisation

3.1 Pulse height analysis

To optimise the system for low-noise detection before considering its geometry, several parameters can be adjusted. One of these system parameters is the energy window, which selects photons meeting energy criteria based on the energy the photon deposits when interacting with a detector block. In the case of PEPT experiments, the 511 keV photon arising from positron annihilation is required, and by discarding detections that are unlikely to have arisen from annihilation the fraction of corrupt LORs can be reduced.

The energy window is defined by upper and lower level discriminators (ULD and LLD), which are set on each module controller in the system. A detection with energy lying between the discriminators is considered valid and is recorded as a singles event. To set these discriminators to optimal values, which maximise the annihilation photons detected while minimising scattered or random detections, an understanding of the system energy resolution is required.

Pulse height analysis enabling energy resolution measurement is described and performed below, making use of a single 951 detector block connected to an amplification and digitisation system. While direct optimisation of energy level discriminators is achievable through module controller calibration functions, functionality is limited in terms of user control and precision. Through external pulse height analysis, improved counting statistics and post-processing enable significantly higher precision measurement of system energy resolution.

A similar pulse height analysis methodology was replicated using a single HR+ detector block in related work [18]. In the case of the Polaris system, where the energy of individual events is directly measured and stored, pulse height spectra were produced through conventional acquisition in previous work [1]. The primary findings from both systems are also detailed below.

Gain matching

The four PMTs of a single 951 detector block were connected to individual NIM preamplifiers and amplifiers and the analogue signals were summed and digitised such that a multi-channel analyser (MCA) could produce pulse height spectra.

However, the PMTs do not provide uniform outputs due to manufacturing and component tolerances, and the resulting pulse height spectra can vary drastically, as evident in Figure 3.2 (left). Therefore, a process of gain-matching was performed to align the photopeaks from each PMT in pulse height by adjusting each tube gain on the amplifier system. This detection and control chain is illustrated in Figure 3.1.

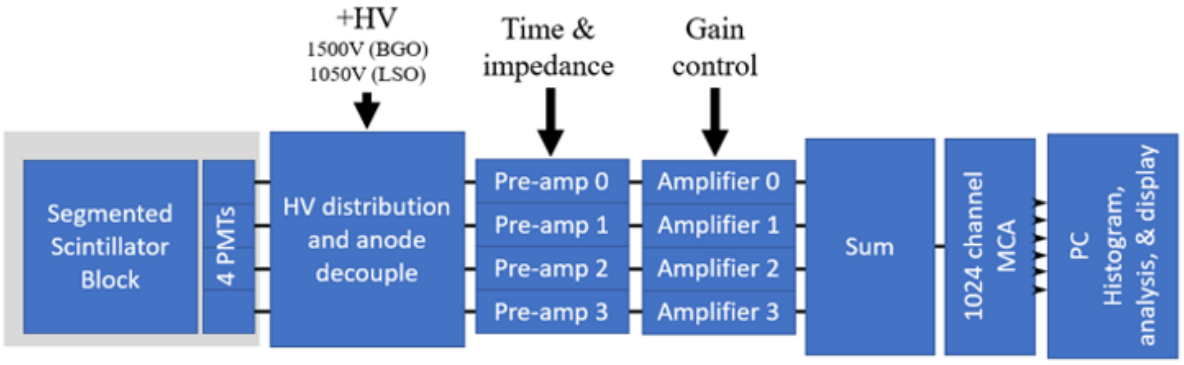

Figure 3.1: Block diagram illustrating the detection system used for pulse height analysis. The signal processing of the block detector output is shown, with analogue signals passing through pre-amplification, amplification and summing stages before digitisation by the MCA and analysis on the PC. Gain inputs to the amplifier system were used for gain matching purposes.

To perform gain-matching, a reference tube was arbitrarily selected, labelled 'Tube 1', and the gains of each other tube were adjusted to produce similar pulse height spectra, using a Na-22 calibration source placed approximately 6 cm away from the block face. To ensure accuracy in identifying the position of the 511 keV peak such that gain adjustments could be made, data was acquired until approximately ten thousand counts were detected in the prominent photopeak of each tube.

Due to a low count rate, caused by necessarily using only a single PMT and a low activity calibration source, perfect alignment of each tube's response was challenging, often requiring up to an hour of measurement to accurately identify the location of the 511 keV photopeak. Coupling this with voltage drift effects that were experienced, in which the position of photopeak could vary over time without adjustment, gain matching was only performed to within reasonable tolerance.

Looking at the summed spectra before and after matching the gains in Figure 3.2 (right), a notable qualitative improvement can be seen. Only two photopeaks and Compton scattering contributions are expected from the Na-22 source, however before gain matching several labelled artefacts are visible, caused by the pulse height misalignment between PMTs. Following gain matching, a smooth spectrum matching expectation is achieved, exhibiting two clear photopeaks, Compton edges and continua with none of the previously noted artefacts.

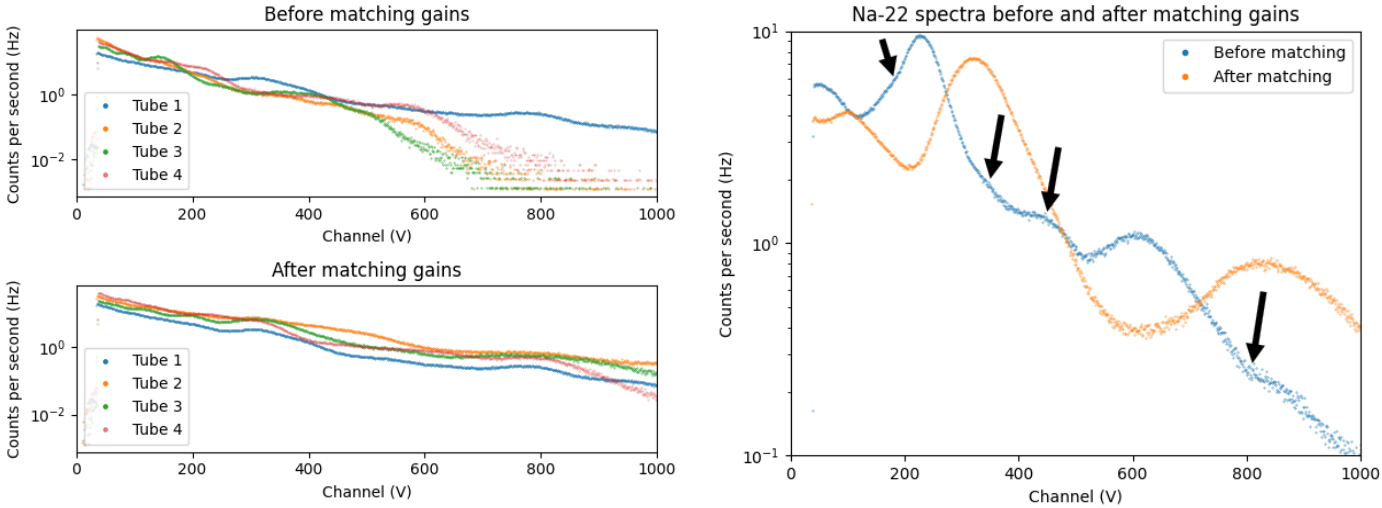

Figure 3.2: Pulse height spectra from individual PMTs (left) and summed from all PMTs (right) before and after the gain-matching process, using a 951 detector block and a Na-22 calibration source. Unexpected artefacts caused by pulse height misalignment between PMTs are labelled with arrows.

Energy calibration

The summed spectra were then used to perform an energy calibration of the detector system, translating measured pulse heights (channel numbers) to their corresponding energies. To perform the calibration, a Gaussian function was fitted to each of the identified photopeaks from the three calibration sources, being Na-22 (511 and 1275 keV), Cs-137 (662 keV) and Co-60 (1173 and 1332 keV) [33]. From the calculated centroid channel values, a weighted linear fit could be performed using expected energy values to provide the calibration in Figure 3.3.

Due to the poor energy resolution of the BGO detector block, the two separate photopeaks of Co-60 could not be independently resolved, and instead formed a single combined peak. Some time was spent with enhanced curve fitting procedures, but it was found to be too challenging to extract distinct parameters without introducing restrictions that may have biased results. Therefore, a single Gaussian function was fitted to the combined peak, producing a single centroid value. However, as the detector response varies depending on the initial photon energy, this centroid cannot be assumed to correspond to the average energy of both peaks.

To account for this, a theoretical description of the Co-60 spectrum, describing the combined peak as the sum of two Gaussian functions, was used to place uncertainty bounds on the possible energy values the combined centroid could represent, taking into account the detector efficiency and energy resolution for each peak. A wide range of estimates were used for both the efficiency and resolution parameters, and a range of these parameters were identified in which the two independent photopeaks could not be qualitatively distinguished. This range was used to set the uncertainty bounds on the energy of the combined peak, and this centroid value was then able to be used in the four-point energy calibration.

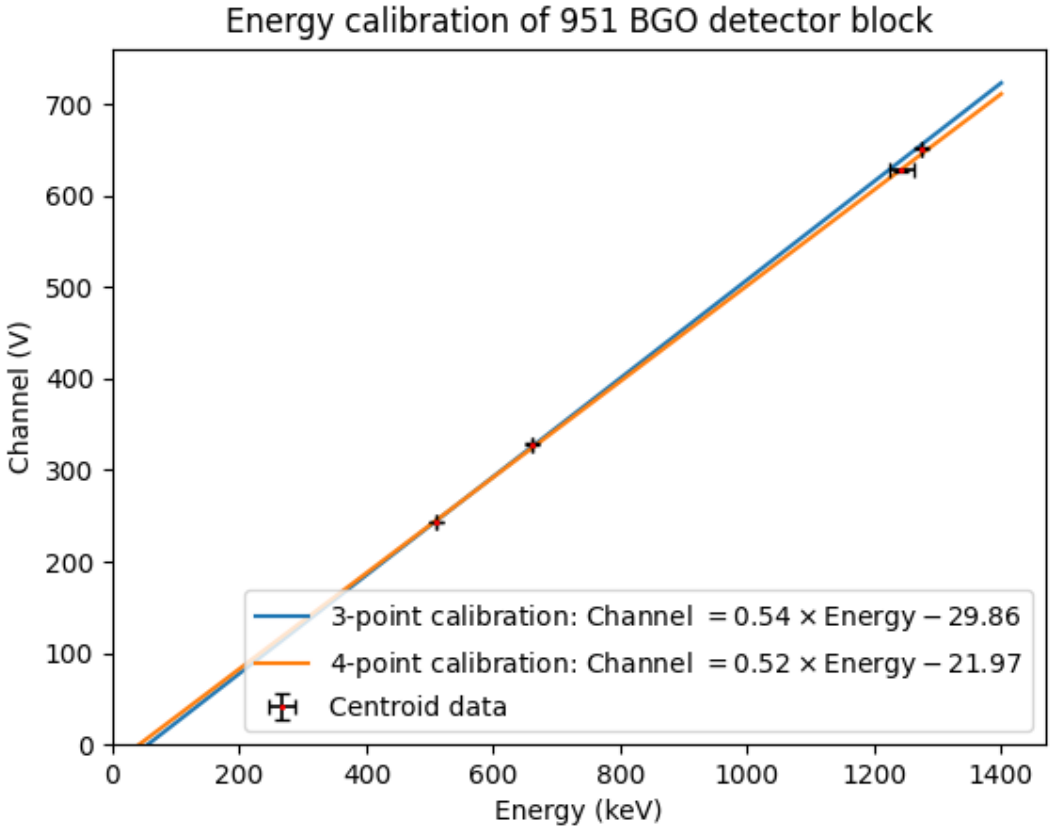

Figure 3.3: An energy calibration performed using fitted centroids and expected energy values, with straight line fits and their corresponding calibration equations displayed. Each fit has a coefficient of determination $R^2 > 0.999$.

Using either the three-point calibration, excluding the Co-60 contribution, or the four-point calibration provided results that differed by less than a single channel at 511 keV, and therefore the four-point calibration was used in the following analysis, taking the difference into account as part of the uncertainty budget.

3.1.1 Energy resolution

Following gain matching and energy calibration of the detector block, the energy spectrum of Na-22 was measured and plotted in Figure 3.4, Cs-137 in Figure 3.5 and Co-60 in Figure 3.6. In each spectrum, Gaussian curves were fitted to the photopeaks as inset plots, such that the centroid energy and standard deviation could be determined.

From the Gaussian function fitted to the annihilation photopeak of Na-22, the energy resolution, defined as $R = \frac{\text{FWHM}}{\text{centroid energy}}$ [41], was determined to be $30.51\% \pm 0.48\%$ at 511 keV. Repeating the process at 662 keV and 1275 keV, the energy resolution was found to be $31.23\% \pm 0.44\%$ and $28.9\% \pm 2.2\%$ respectively.

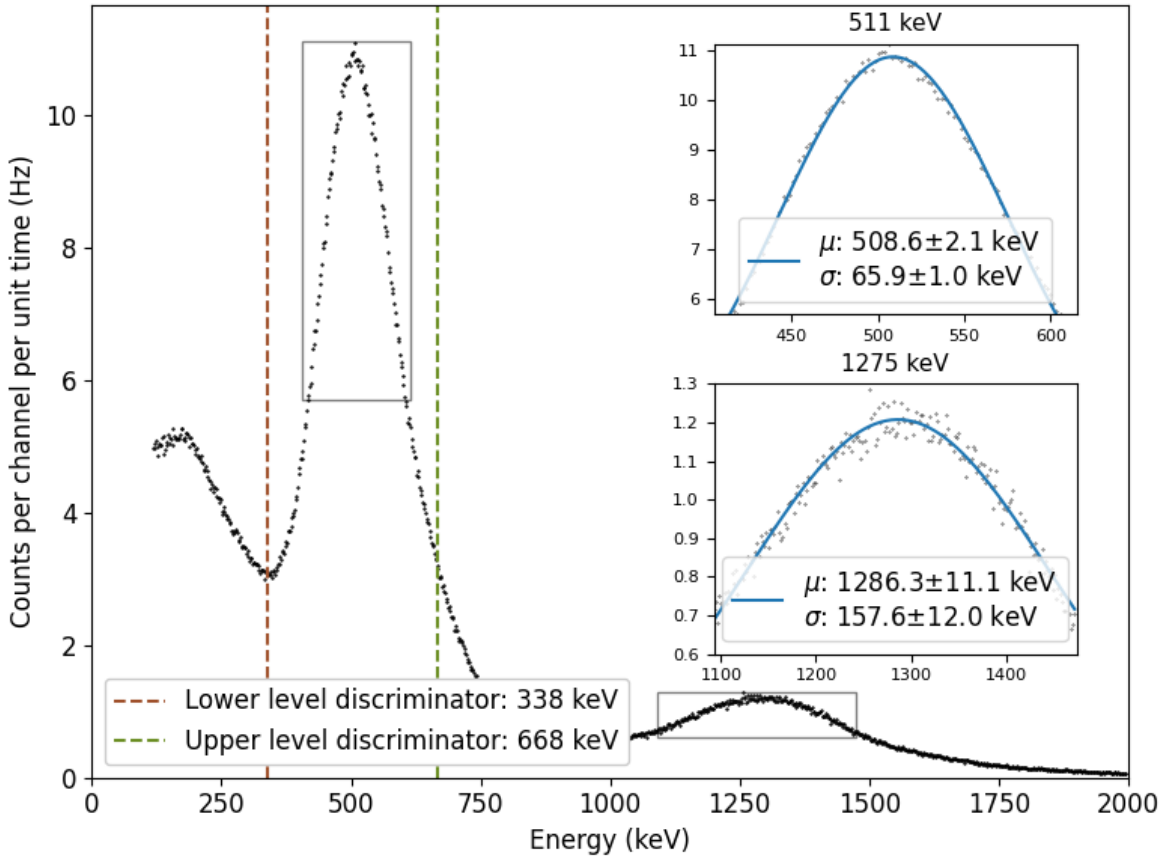

Figure 3.4: Calibrated energy spectrum of the Na-22 calibration source as measured by a 951 detector block. The optimal LLD and ULD are shown as dashed vertical lines, with values displayed in the legend. **Inset plots:** Gaussian curves fitted to the 511 keV (top) and 1275 keV (bottom) photopeaks, with fitting parameters displayed in the legend.

3.1.2 Energy discriminators

Using the computed energy resolution at 511 keV, the optimal LLD and ULD were selected such that 99% of the annihilation photopeak was encompassed within the energy window. This was achieved using discriminator values of $\mu \pm N\sigma$, with fitted centroid energy μ and standard deviation σ, selecting N to be approximately 2.58 which provides 99% coverage. The optimal LLD and ULD values were therefore calculated to be 338.9 ± 3.3 keV and 678.4 ± 3.3 keV respectively, shown in Figure 3.4.

The theoretical value of the Compton edge, given as [41]:

$$E_{Compton} = E\left(1 - \frac{1}{1 + \frac{2E}{m_e c^2}}\right),$$

can be calculated at $E = 511$ keV to be approximately 340 keV, overlapping with the selected LLD. Therefore, this choice of LLD excludes the majority of single Compton scattered 511 keV photons. Many of these photons may have scattered for the first

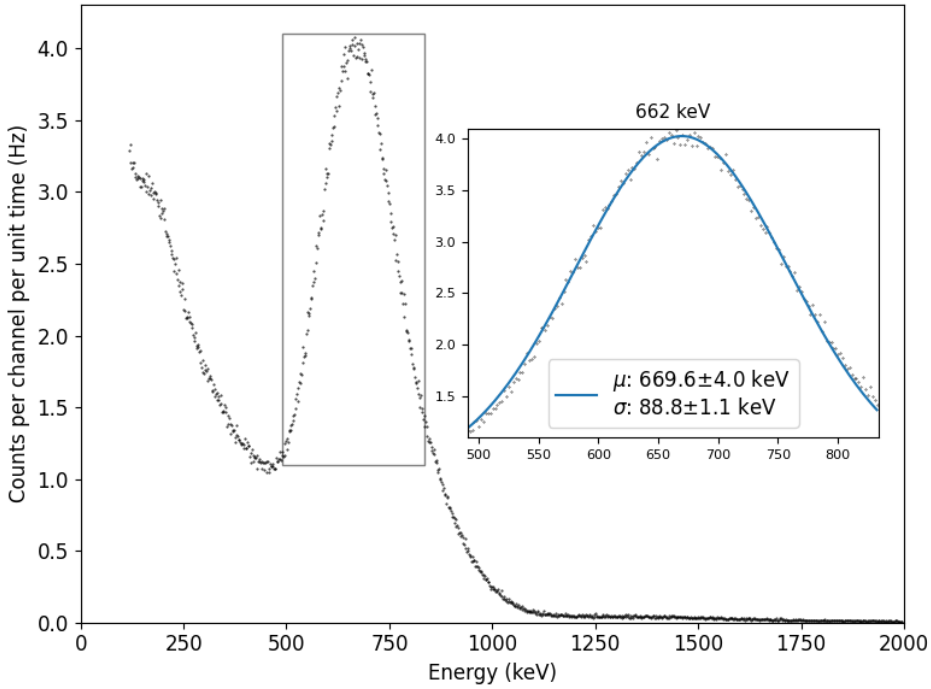

Figure 3.5: Calibrated energy spectrum of the Cs-137 calibration source as measured by a 951 detector block. **Inset plot:** A Gaussian curve fitted to the 662 keV photopeak, with fitting parameters displayed in the legend.

time within the detector, producing singles events that would lead to true coincidences, but this conservative choice aims to exclude higher energy photon scatter, either from associated gamma emissions or unassociated external sources, to reduce corrupt LORs produced from these detections.

The selected ULD is slightly larger than the value used in typical PEPT systems, being in the range of 650 keV [46], but is instead symmetric about the centroid and includes only a small fraction of additional events. These events should not contribute significantly to corrupt LORs, especially with the use of a pure positron emitter with no associated gamma emission, such as F-18.

3.1.3 Key HR+ and Polaris results

With an identical methodology to the above, calibrated energy spectra were produced with the HR+ detector block in related work [18]. By fitting a Gaussian curve to the 511 keV photopeak, the energy resolution was measured to be approximately 33%. Varying by less than 2% of the resolution measured for the 951 block above, the use of different energy level discriminators for each block type within the scintillator system was not considered, as operation complexity would increase substantially.

In the case of the Polaris system, energy discrimination is performed in software and all detected events are stored with the associated energy of interaction. Therefore, energy spectra were easily produced through conventional data acquisition, and an energy reso-

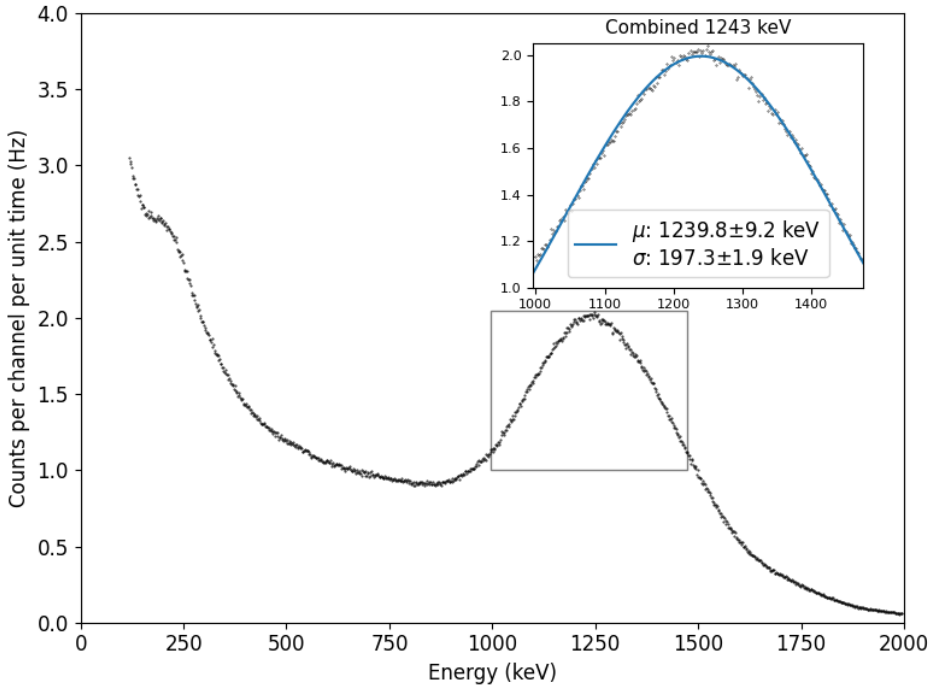

Figure 3.6: Calibrated energy spectrum of the Co-60 calibration source as measured by a 951 detector block. **Inset plot:** A Gaussian curve fitted to the estimated combined 1243 keV photopeak, with fitting parameters displayed in the legend.

lution of $1.15\% \pm 0.04\%$ was measured at 511 keV [1]. The calibrated 511 keV photopeak is shown in Figure 3.7 for both the HR+ block and the Polaris system, demonstrating the significant difference in energy resolution.

3.2 Coincidence window

In addition to the energy window, a system parameter that can be adjusted to optimise for low-noise detection is the coincidence window. Any detected photon with an accepted energy value is considered a singles event, and any two singles events are regarded as coincident if they occur within the same period 2τ, defined as the coincidence window. These coincident events define LORs, and as the random coincidence rate scales linearly with τ careful selection of the coincidence window can reduce the detected fraction of corrupt LORs, reducing noise in the system and therefore improving its spatial resolution.

In the following analysis, the complete modular system, as described in Section 4.2, was required for coincidence measurement, involving both HR+ and 951 detector blocks. A similar analysis for the Polaris system was performed in previous work [1] and key results are detailed below.

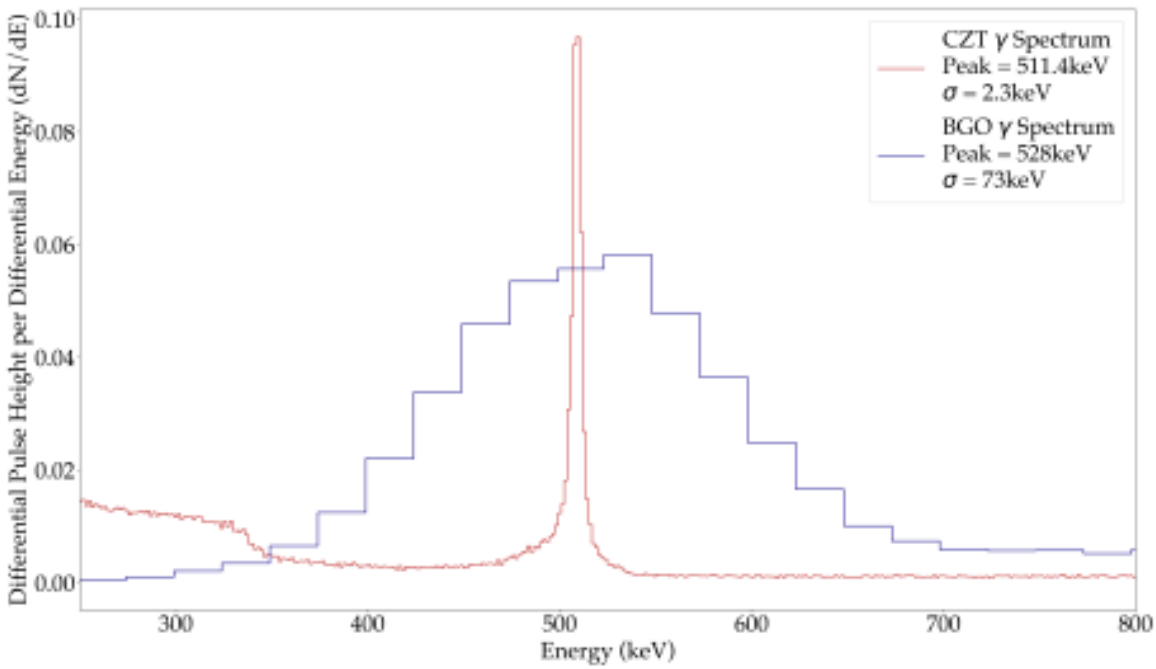

Figure 3.7: The annihilation photopeak of the Na-22 calibration source as measured by the Polaris system and the HR+ detector block, reproduced from [17]. Both spectra have been normalised to the area under each peak and the HR+ spectrum has been scaled down by a factor of ten for clarity in comparison.

3.2.1 Coincidence timing resolution

To gain an understanding of the timing characteristics of the system, singles events were recorded for a Na-22 calibration source placed in the centre of the modular camera FOV.

The coincidence window was increased to 256 ns, much larger than typical, and the frequency of absolute time differences of all possible coincidence events was measured and plotted in Figure 3.8. In addition, the PEPT algorithm was applied with varying f parameters and the frequency of time differences for events used in the reconstruction was plotted on the same axes. From the figure, it is clear that in all cases fewer than 1% of coincidences have an absolute time difference greater than 12 ns, and a significant majority of coincidence events occur with a difference of 4 ns or less. Since a selected value of τ corresponds to a cutoff point in absolute time difference, the optimal coincidence window 2τ is expected to lie between 0 ns and 24 ns.

To further investigate the optimal coincidence window, coincidence delay curves were used to gain an understanding of the coincidence timing resolution [41]. A variable time delay was added to the events detected on one side of the system, and coincidence events were counted and plotted in Figure 3.9 for various coincidence windows 2τ. Note that the timestamp resolution of detected coincidence events is 4 ns, implying that only integer multiples of 8 ns may be used as the coincidence window 2τ.

A typical curve generated by this procedure is Gaussian in shape when τ is lower than

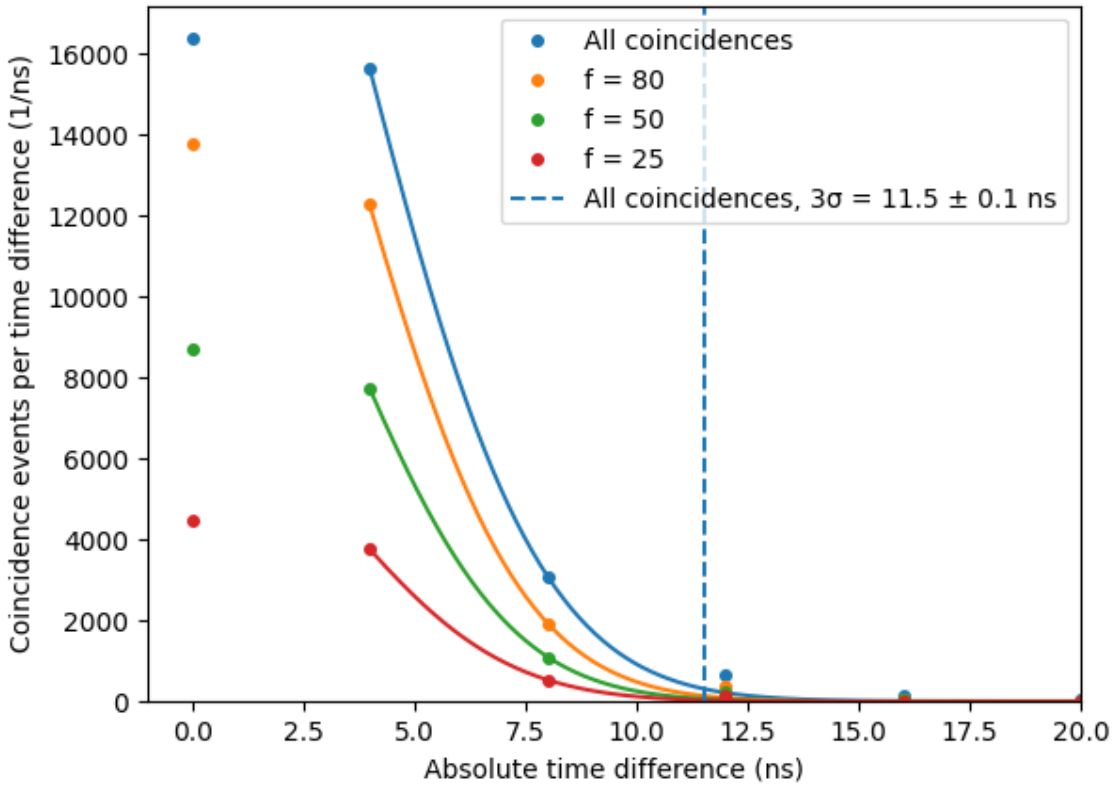

Figure 3.8: The measured coincidence rate as a function of the absolute time difference between measured events, plotted for all coincidences as well as the events used following application of the PEPT algorithm for different f parameters. Gaussian curves are fit to estimate tail behaviour, and an upper limit containing 99% of all coincidence events is plotted as a dashed line at approximately 11.5 ns.

the coincidence timing resolution of the system, defined here as the standard deviation of the largest Gaussian-shaped coincidence delay curve, reaching a maximum coincidence rate when no delay is added. As τ is increased to the coincidence timing resolution of the system, the coincidence window 2τ covers most true coincidences. With necessarily discrete coincidence windows of 8 ns intervals, the closest window is $2\tau = 8$ ns, being the largest coincidence window maintaining a purely Gaussian-shaped coincidence delay curve in Figure 3.9. Increasing 2τ beyond this point leads to the detection of most true coincidences at multiple delay values, creating a plateau in the coincidence delay curve.

In conventional PEPT measurement this plateau may be desirable, allowing some tolerance for timing drifts in the system such that true coincidences are not lost, improving location rates. However, as demonstrated above in Figure 3.8, an increase of the coincidence window beyond $2\tau = 24$ ns is unlikely to include useful events, instead increasing the random coincidence rate and therefore noise. The choice of coincidence window is therefore informed by a trade-off between the achievable location rate and spatial resolution, which may be application-dependent.

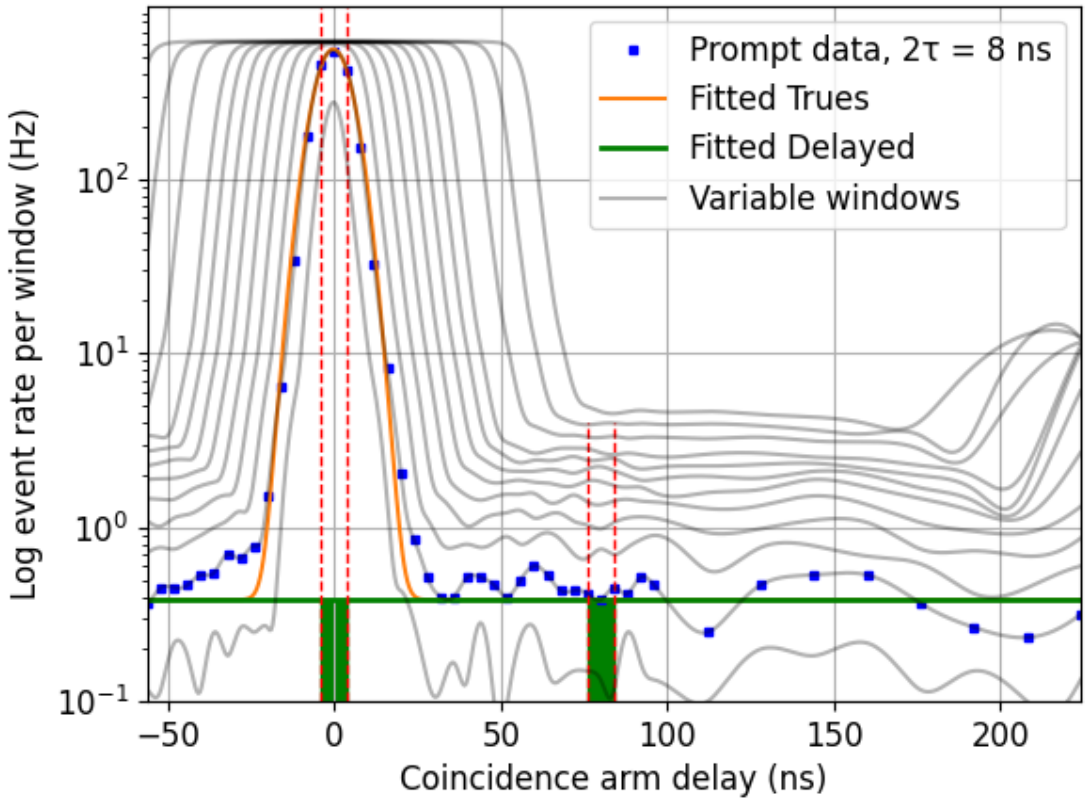

Figure 3.9: Coincidence delay curves of various coincidence windows plotted using a Na-22 source placed within the modular system. The maximal Gaussian case $2\tau = 8$ ns has a Gaussian fit overlaid, with standard deviation 5.37 ± 0.17 ns, along with the mean random rate plotted as a horizontal line and the window width displayed as vertical dashed lines.

For example, the study of slow-moving tracer particles may not be noticeably affected by a reduction in location rate, and would therefore benefit from a smaller coincidence window, whereas at greater velocities the location rate becomes more important in meaningful study, requiring a larger coincidence window. Since the modular system is designed in general, an intermediate case is desired, choosing a coincidence window such that neither the location rate nor spatial resolution is unnecessarily sacrificed, with the understanding that either can be optimised with coincidence window adjustments.

3.2.2 Window impact on PEPT performance

To find this intermediate coincidence window, both the achievable spatial resolution and location rates following PEPT analysis were investigated.

The windows $2\tau = 8$ ns, corresponding to the largest coincidence window maintaining a Gaussian-shaped coincidence delay curve as seen in Figure 3.9, $2\tau = 16$ ns and $2\tau = 24$ ns, corresponding to at least 99% coverage of all true coincidences as seen in Figure 3.8, were used in the PEPT analysis of the previous measurement, and their

relative performance in terms of spatial resolution and location rate was compared in Figure 3.10.

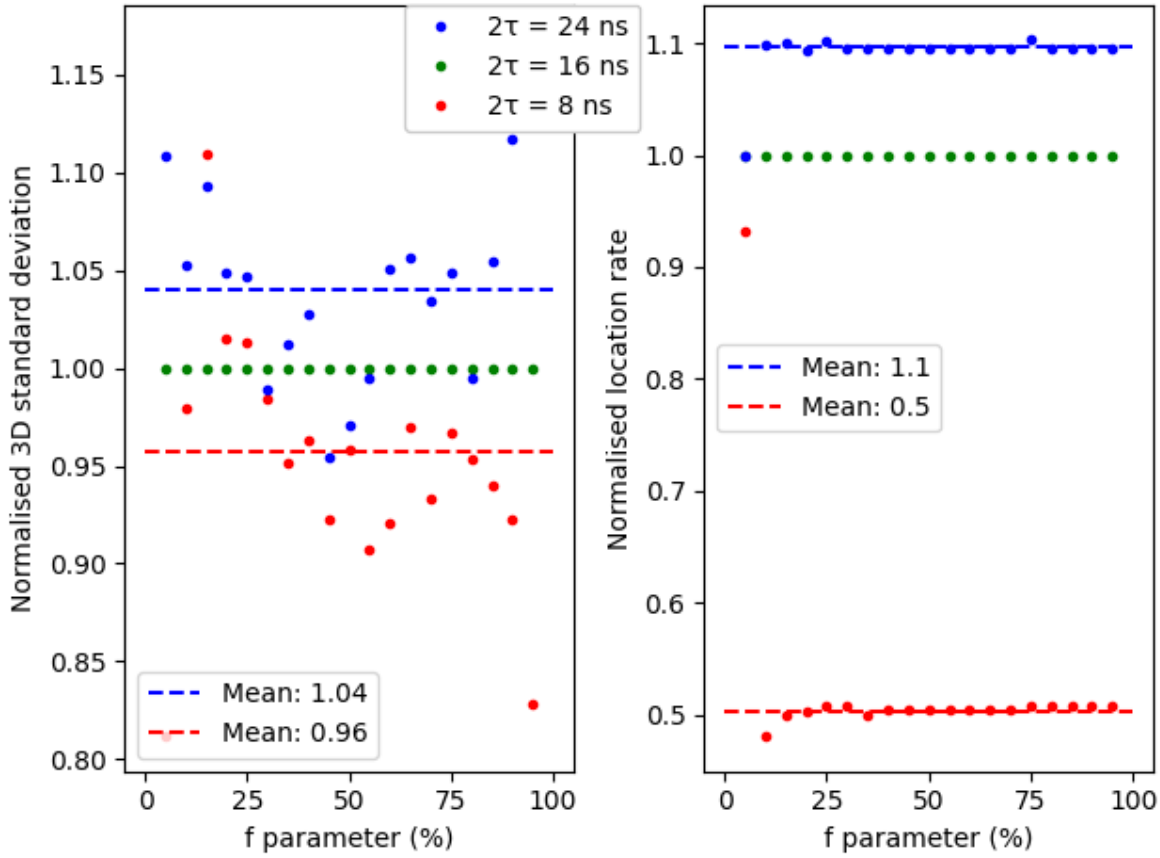

Figure 3.10: The 3D standard deviation (left) and location rate (right) plotted as a function of the PEPT algorithm f parameter for $N = 215$. Both plots are normalised to the $2\tau = 16$ ns case. Mean values for the 8 and 24 ns cases are plotted as dashed horizontal lines.

Increasing 2τ from 8 ns to 16 ns approximately doubled the location rate regardless of other PEPT algorithm parameters. Increasing 2τ to 24 ns then provided only an additional 10% improvement in location rate. Increasing 2τ beyond 24 ns led to negligible location rate improvements.

The spatial resolution of the system, defined here as the three-dimensional standard deviation, was in contrast highly dependent on selected PEPT algorithm parameters, and in general was not predictable for arbitrary measurements. Therefore, for the sake of comparison, the means of each window were compared. Decreasing 2τ from 24 ns to 16 ns produced an approximately 4% improvement in spatial resolution, with similar results following a further decrease to 8 ns. Increasing 2τ beyond 24 ns led to the increased inclusion of random events, reducing spatial resolution further.

In an attempt to consider these results simultaneously, a trial figure of merit was used, being the standard deviation divided by the location rate, once again normalised to the 16 ns case and plotted in Figure 3.11. As the aim was to minimise standard deviation

while maximising location rate, lower values were desired.

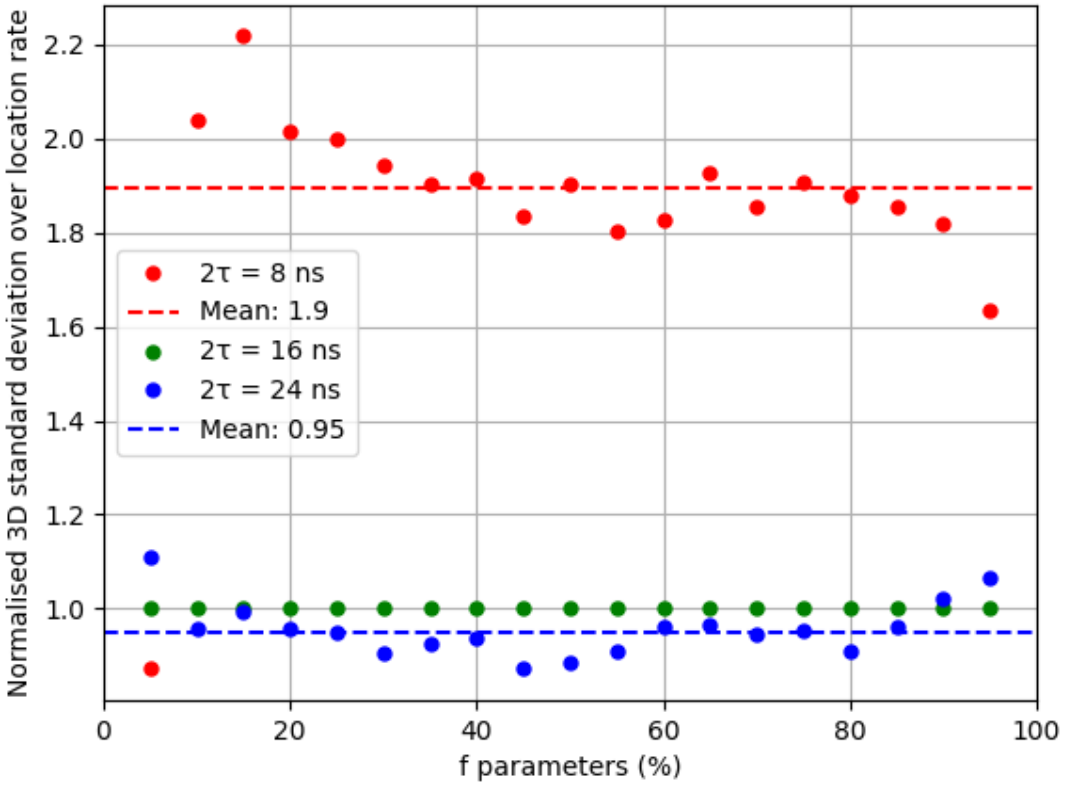

Figure 3.11: The 3D standard deviation divided by the location rate, plotted as a function of the PEPT algorithm f parameter for $N = 215$. Both plots are normalised to the $2\tau = 16$ ns case. Mean values for the 8 and 24 ns cases are plotted as dashed horizontal lines.

From this metric, it can be seen that the $2\tau = 8$ ns case offers poor results, caused by the significant reduction in location rate when compared to the slight improvement in spatial resolution. The $2\tau = 16$ ns and $2\tau = 24$ ns cases are more comparable, with the 24 ns case offering a 5% improvement on average, as the slight reduction in standard deviation is outweighed by the moderate improvement to location rate.

However, in contrast to the Polaris system, the location rates of the modular camera are not expected to be limiting. Therefore, the achievable spatial resolution was favoured more heavily in the selection of the optimal coincidence window than the figure of merit, such that the 5% improved spatial resolution of the $2\tau = 16$ ns case outweighed the 10% improved location rate of the $2\tau = 24$ ns case.

Therefore, the optimal coincidence window was selected to be $2\tau = 16$ ns, as the trade-off between spatial resolution and location rate is sufficiently managed in general cases. For applications requiring improved spatial resolution a window of 8 ns may be used, and for applications requiring improved location rates a window of 24 ns may be used.

3.2.3 Key Polaris results

To optimise the coincidence window for the Polaris system, a similar process was followed in previous work [1]. A variable time delay was added to the measured events of one Polaris module in coincidence event processing, and a coincidence delay curve was generated as shown in Figure 3.12. In this work, a single coincidence window of $2\tau = 300$ ns of was used, producing a plateaued curve as the chosen value of τ was greater than the system coincidence timing resolution. Regardless, a Gaussian curve was fitted to estimate the coincidence timing resolution. To determine this resolution precisely, the analysis must repeated in future work with additional coincidence windows such that the maximal Gaussian case may be found, as in Figure 3.9.

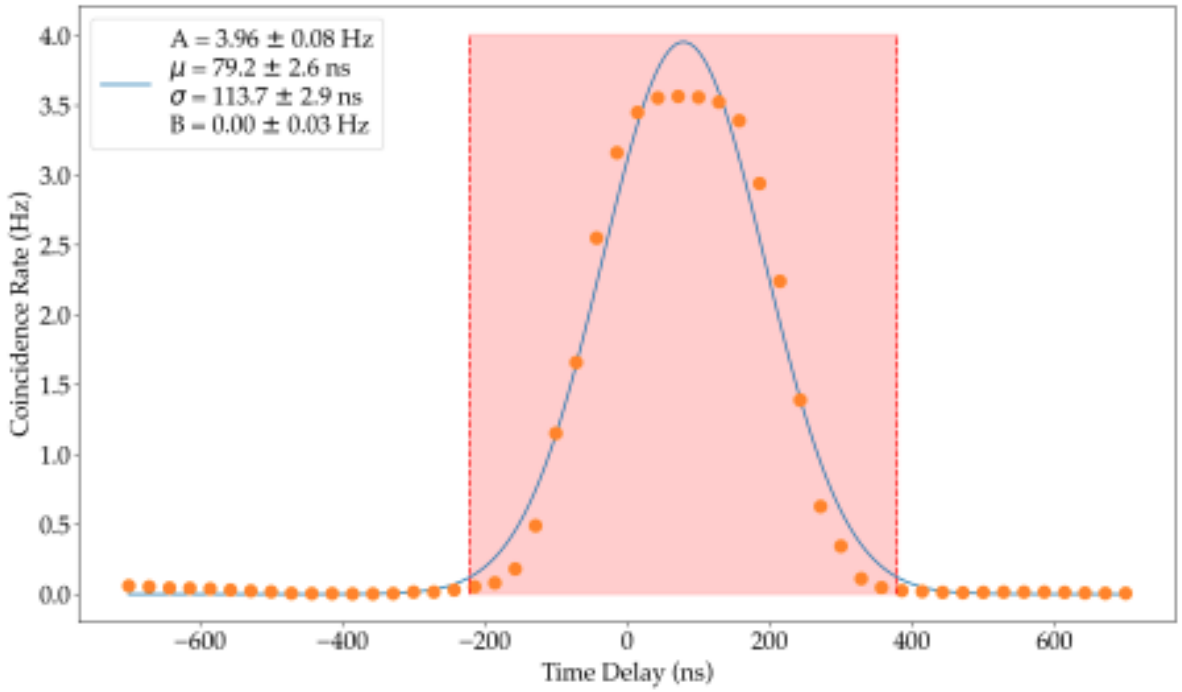

Figure 3.12: The coincidence delay curve measured by the Polaris system with a coincidence window of 300 ns, reproduced from [17]. A Gaussian curve has been fitted, estimating system coincidence timing resolution with fitting parameters displayed in the figure legend. Shaded in red is the initially selected optimal coincidence window of 600 ns, or approximately 5σ.

However, precise knowledge of the coincidence timing resolution was not utilised in the selection of optimal coincidence windows for the Polaris system. To improve upon the limiting location rate, a large coincidence window of approximately 600 ns was used initially, aiming to detect a majority of true coincidence events by covering the majority of the coincidence delay curve. Since the random coincidence rate was expected to be minimal, due to low efficiency and hence overall low singles rates, this choice did not significantly affect the achievable spatial resolution of the system.

In further investigation, the use of a much larger coincidence window was found to offer similar PEPT location uncertainties with improved location rates. Through deeper

analysis, two additional peaks in the coincidence delay curves were identified at delays of approximately ±1500 ns. It was proposed that these coincidence events were true coincidences with inaccurate timestamps caused by buffering effects in processing electronics. Therefore, a final coincidence window of 5 µs was found to be optimal for the Polaris system.

3.3 Summary and discussion

In this chapter, detection parameters, being energy level discriminators and coincidence windows, were measured and optimised for low noise detection, aiming to exclude a majority of corrupt LORs in detection before PEPT tracking. These parameters were measured here for the 951 detector block and modular camera system, with key results for the HR+ detector block and Polaris system given from related [18] and previous [1] work.

The energy resolution of the 951 detector block was measured to be $30.51\% \pm 0.48\%$ at 511 keV, with the HR+ block having a similar resolution of approximately 33%. Aiming to encompass approximately 99% of the annihilation photopeak, while conservatively opting to exclude the detection of Compton scattered events to maximise spatial resolution, lower and upper energy level discriminators of 338.9 ± 3.3 keV and 678.4 ± 3.3 keV respectively were selected for the BGO detector blocks. With the Polaris system, the energy resolution was determined to be $1.15\% \pm 0.04\%$ at 511 keV, but the use of no energy discrimination was determined to be optimal in maximising the limiting location rate of the system with no corresponding reduction in spatial resolution.

Secondly, optimal coincidence windows 2τ were determined for the modular camera. Through the measurement of the coincidence delay curve, the coincidence timing resolution, taken to be the standard deviation of the maximal Gaussian curve, was determined to be 5.37 ± 0.17 ns. Through comparison of PEPT performance using several different coincidence windows the optimal window $2\tau = 16$ ns was selected. As discussed, this window is fairly large, leading to the increased detection of random coincidences. However, the corresponding gain in achievable location rate was determined to offer the optimal trade-off between spatial resolution and location rate in general applications. As tracer activity is increased or improved spatial resolution is required, the minimal window $2\tau = 8$ ns may be used instead. With a similar analysis of the Polaris system, a wide coincidence window of 5 µs was found to be optimal, capturing all genuine coincidences. This extremely long coincidence window may have a negative impact in future work, when both the Polaris system and the modular camera may share a coincidence gate, and will require additional investigation.

In future work, the precise characterisation of system energy and timing resolution as performed here may enable detector-level corrections to measured responses. Each detector module, block, or even individual crystal element may be referenced against its own energy and timing calibrations, with systematic offsets in measured responses corrected post-acquisition, improving upon the accuracy, and therefore quality, of measured events.

In conclusion, optimal detection parameters have been measured and selected for low noise detection above, enabling enhanced spatial resolution towards micro-scale precision. Building upon this, design and development of the optimal modular camera geometry is

performed in Chapter 5, leveraging the achieved low noise detection for optimal absolute efficiency, enhancing both spatial resolution and location rates.

Chapter 4

Modular camera

Following the component characterisation of the previous chapter, this chapter covers the design, development and construction of the modular BGO scintillator array, or modular camera. The camera geometry is optimised in terms of its sensitivity and spatial resolution towards future use with the Polaris system in a hybrid camera.

4.1 Proof of concept and compatibility

One of the main ideas in the development of the modular BGO camera was to incorporate detector elements from both the 951 and HR+ scanners. Due to their differing pixel and overall sizes, a trade-off exists between the achievable absolute efficiency and spatial resolution, which can be optimised in the placement and quantity of detectors used for micro-scale tracking.

The data acquisition system available for use with the modular camera was capable of interfacing with both the module controllers of the HR+ and 951 systems, where each HR+ controller connects to twelve detector blocks and each 951 controller connects to only four. However, as a small, compact system was desired to maximise geometric efficiency and reduce the scale of measurement in comparison to conventional PEPT systems, the use of few detector blocks (less than 20) was expected in the design of this modular camera. As each controller can only read an event from a single detector block per cycle, the use of HR+ controllers would lead to the loss of events within the same cycle from the other eleven connected blocks. In comparison, the use of 951 controllers would lead to the loss of events from only three other blocks within the same cycle. Therefore, it was desirable to make use of only 951 controllers in this system, connecting to both 951 and HR+ blocks.

However, it was necessary to test the compatibility of the HR+ blocks with the 951 controllers. Since the blocks have similar construction, consisting of four PMTs with separate data cables, it was plausible that the HR+ blocks could be connected to the 951 electronics and used without any adjustment. However, possible incompatibilities led to the requirement of testing the combination for certainty.

One factor that may have led to the HR+ blocks not being compatible with the 951 controllers was the high voltage supply to the 951 blocks running through each PMT connection directly, as opposed to the HR+ block where it is supplied through one such

PMT connector and then distributed within the block. Another issue to consider was possible gain limitations and impedance matching. Since the HR+ blocks are newer and typically have improved manufacturing, the output signal from each HR+ block is greater than that of the 951 block, and a lower gain is required to produce a processable signal. If the appropriate gain is too low, using both 951 and HR+ blocks on the same controller may be impossible, impacting camera design decisions as the HR+ blocks would require the bias voltage to be lowered such that the controller gain could lie within an accessible range.

To test these possible issues, a trial setup of four 951 blocks and four HR+ blocks connected to two separate 951 controllers was used, shown in Figure 4.1. Using a calibration Na-22 source, it was evident that each PMT was providing reasonable output when looking at the histograms returned from the serial connection, indicating that the first possible issue of high voltage supply would not be an issue.

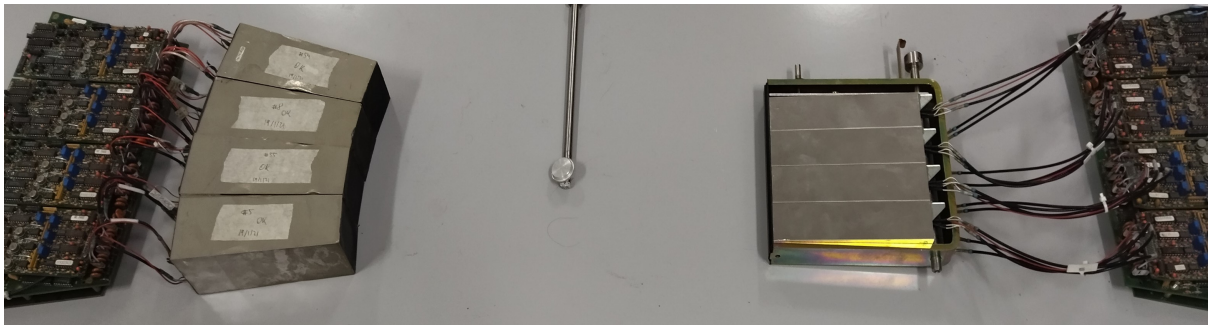

Figure 4.1: Trial setup of four 951 blocks (left) and four HR+ blocks (right) used to test compatibility with 951 module controllers. A calibration Na-22 source is placed centrally.

By calibrating each detector block, optimal PMT gains for the HR+ blocks were found using the same bias voltage as for the 951 detector blocks, indicating that the second issue of using both HR+ and 951 blocks connected to the same controller would also not be an issue.

With these issues tested, a PEPT measurement with the calibration source placed centrally was made. As this was just a proof of concept experiment, placement of both the detector modules and source was approximate, calibration of the detector blocks was not performed to the highest possible quality, and mostly default PEPT algorithm values were used. Despite this, promising results were demonstrated, and a subset of measured LORs are plotted in Figure 4.2 demonstrating convergence.

When optimising the PEPT algorithm for maximal event rate, ten lines per location and an f_{opt} of 90% were used, giving a 4 mm average location uncertainty with seven computed locations per second. When optimising for minimal location uncertainty, 150 lines per location and an f_{opt} of 50% produced < 0.5 mm location uncertainty with one computed location every two seconds.

However, these results are not unsurprising, as the reduced size of the setup leads to an improvement in geometric efficiency, as well as an overall reduction in the scale of corresponding PEPT measurements. In addition, the source used was low activity with minimal scattering material within the system FOV, leading to mostly true coincidences

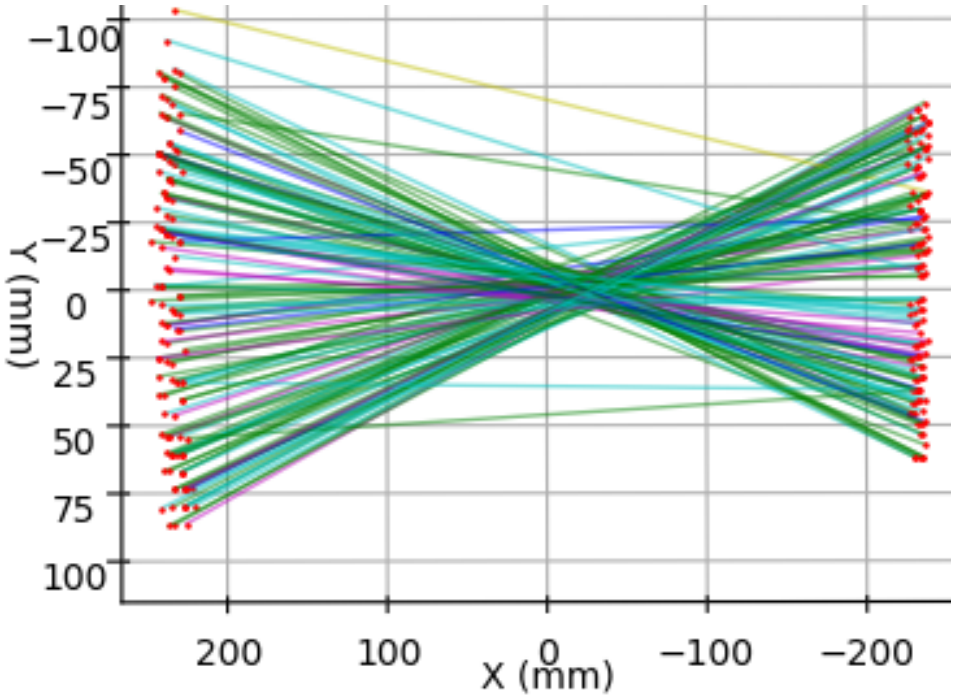

Figure 4.2: Top-down view of LORs measured by the trial setup of Figure 4.1. LOR colour indicates the absolute time difference between each side of the coincidence event, unused here.

being detected, minimising the contribution of corrupt LORs to the location uncertainty. Regardless, these results demonstrate the applicability of a modular setup to micro-scale PEPT measurements, and lead the way towards the full development of the modular camera.

4.2 Modular camera geometry

The most important decision to be made in the construction of the modular scintillator camera was that of the geometry of the system, i.e. how many of each type of detector to use and where to place them. Since the data acquisition system enables fully modular detector setups and geometry adjustments only require the repositioning of detector blocks and slight code adjustments, many options were available for the system geometry.

A difficulty in the design of the camera was the fact that a direct application of the system was not yet under consideration. For a specific application, the geometry of the system could be optimised directly for application requirements and system limitations could be used to simplify some aspects of the design process.

For example, an experiment needing to measure a very slow-moving tracer particle in a small FOV may benefit from using only HR+ blocks tightly packed and placed close together to leverage the increased spatial resolution, whereas a faster-moving tracer particle in a larger FOV may require blocks placed further apart, where the greater absolute efficiency of the 951 blocks would be useful. In addition, specific physical constraints

of the experiment could significantly influence the placement of detector modules, such as limited space surrounding a region of interest. Some examples of these cases are demonstrated in Figure 4.3.

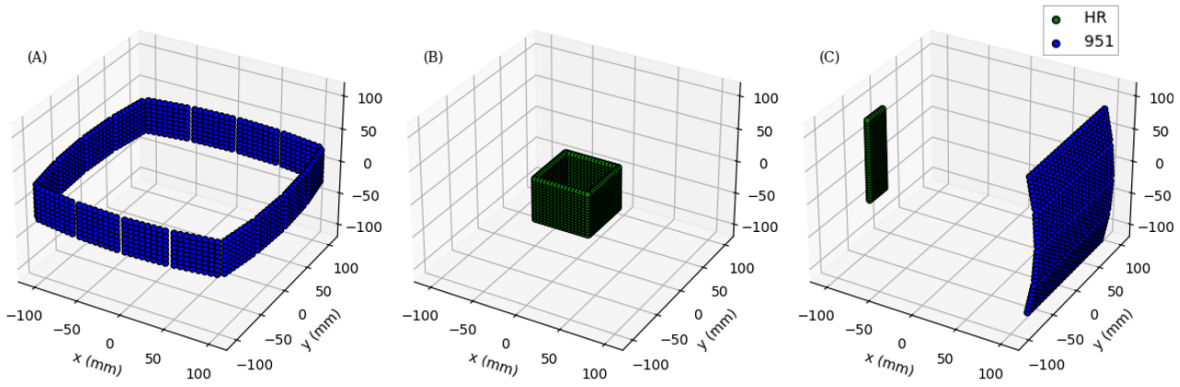

Figure 4.3: Three possible modular array geometries for application-specific constraints, with each detector crystal displayed as a separate point coloured corresponding to block type. In geometry A, a large FOV (approximately 2000 cm^3) is available with 951 blocks, whereas a much smaller FOV (approximately 108 cm^3) is available in geometry B with HR+ blocks. The absolute efficiency and spatial resolution of geometry B is significantly greater than in geometry A. Geometry C could be used in physically limited systems, for example where there is little space on one side of the system such that only a few of the smaller HR+ blocks could fit, coupled with a larger array of 951 blocks to increase the FOV and absolute efficiency. In this geometry, individual block event readout is especially important to enable adequate coincidence rates.

As restrictions such as these were not considered in the design of this camera, a generic proof of concept design was opted for, demonstrating the system's potential capabilities as much as possible, with the understanding that specific applications could require changes.

The data acquisition system chosen for this work connects to a maximum of four 951 controllers, so a setup of four modules was selected, each connected to four detector blocks. A mixed setup of eight HR+ blocks and eight 951 blocks was chosen so that optimisation of the spatial resolution/absolute efficiency trade-off could be leveraged, but also to demonstrate that mixed systems were viable and that applications could make use of differing combinations of blocks as mentioned above. As for the placement of the detector blocks, a symmetric setup of two identical tightly packed units placed opposing one another was opted for to reduce complexity and encourage uniformity of the sensitivity profile.

Within these constraints, options remained, and to compare possibilities a simulation code was used.

4.2.1 Simulation

Once the design parameters of the camera were established, a simulation of the modular scintillator array sensitivity profile was used to further optimise the placement of the de-

tector blocks, aiming for a centrally uniform sensitivity profile to avoid deadtime limiting hotspots and to allow uniformity of PEPT measurements over the volume.

The simulation code draws lines between each crystal element of an arbitrary system geometry, generating a heatmap of the system FOV indicating the number of lines passing through each point, which correlates to the sensitivity. Coincident modules are defined to prevent lines from being drawn between crystals either within the same detector module or between adjacent modules, as these lines correspond to a tracer particle placed outside of the operating FOV of the system.

As opposed to typical sensitivity profile simulations, this code does not simulate the decay of a tracer particle, nor does it simulate detection processes within each crystal. Therefore, more complex features of the sensitivity profile need to be accounted for. A Gaussian blurring effect was applied to the endpoints of each line, accounting for the volume effects of the crystals. The line endpoint was sampled from a Gaussian distribution, using the centre of the crystal as the mean of the distribution and the dimensions of the pixel as the 3D standard deviation, with the result constrained to lie within the crystal. Since each detector type has a different detection efficiency, the line intensity is scaled to account for coincidence detection probabilities. This scaling is achieved by multiplying the intensity of each line with the intrinsic efficiencies of both detector types at each line endpoint.

Finally, each detector block type has differing pixel densities. Since lines are drawn between each pixel, a greater pixel density implies a greater number of lines drawn from the corresponding block. Since these lines generate a heatmap, the more lines drawn the greater the simulated sensitivity. However, simply increasing the pixel density of a detector should not directly improve its efficiency, and with this simulation a small detector with a large pixel density will appear to have much greater efficiency than a larger detector with a small pixel density, regardless of the true efficiency of the detector. By dividing the intensity of each line by the sum of the corresponding pixel area-densities, this effect is accounted for. This is a simple fix, working in the case of same-type coincidences, however, this over-simplifies the case of coincidences between different detector types. Since the pixel area-densities of the HR+ and 951 blocks are similar and coincidences between the Polaris system and the BGO system were not considered at this stage, as a physical timing system enabling cross-system coincidence was not yet developed, possible solutions to this issue were not explored.

Specific simulated geometries

From the design limitations previously decided on, systems consisting of two units (four modules) with four HR+ and four 951 detector blocks on each side were considered.

Units consisting of alternating HR+ and 951 blocks were unlikely to offer satisfactory uniformity of the sensitivity profile in the centre of the FOV, since reflection symmetry would be broken, and would likely complicate the characteristics of the profile. To maintain two axes of reflection symmetry with the aim of improving the uniformity of the sensitivity profile, two blocks of one block type would be placed centrally in each module, surrounded by the other block type. Therefore, the other module in the unit could be placed on top of or alongside the first to create a central 2x2 square of a single block type.

This restriction led to several options for the placement of the surrounding detectors. If the blocks were not tightly packed, i.e. spaces were left between blocks, the FOV of the system may be increased. However, sensitivity profile uniformity and simplicity would suffer due to areas of higher and lower sensitivity formed by the spaces, as opposed to simpler sensitivity gradients expected from tightly packed geometries. Opting for simplicity in the sensitivity profile, only tightly packed geometries were considered to maintain horizontal reflection symmetry.

Finally, these restrictions left only two options in the design of the system; one option with 951 blocks placed centrally with tightly packed HR+ blocks placed surrounding them, or the opposite. Both options were simulated with predicted geometries, shown in Figure 4.4, and it was found that in the case of the central 951 blocks the high sensitivity central region was smaller, and the overall profile was less uniform, than that of the central HR+ blocks case. In addition, the spatial resolution offered by the HR+ is greater than that of the 951 blocks by virtue of their pixel densities, and placing them centrally leverages this benefit.

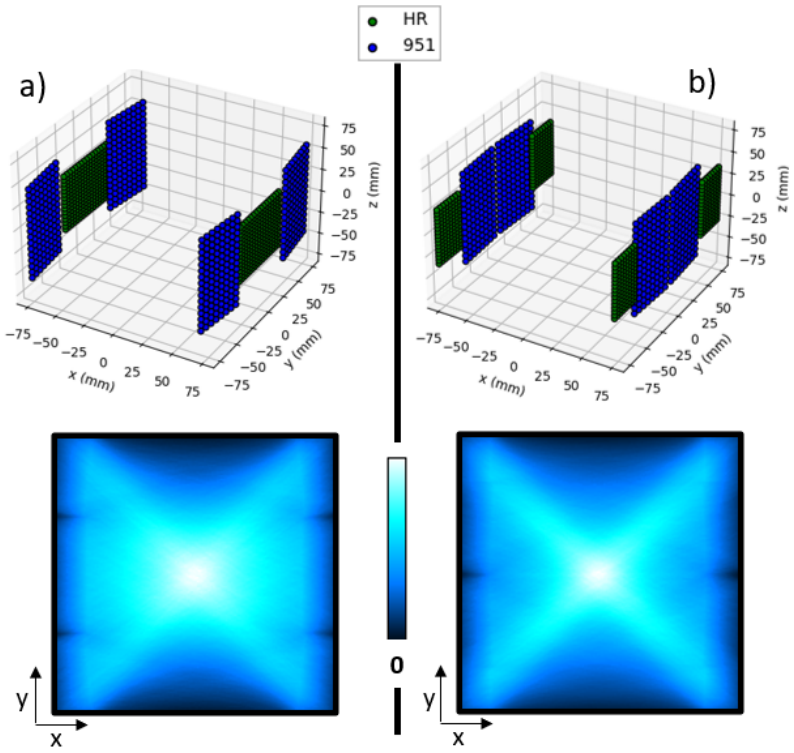

Figure 4.4: The possible modular scintillator camera geometry with the simulated sensitivity profile for a central 2x2 square of HR blocks (a) and 951 blocks (b). Along the top row, the geometries are shown as individual pixels demonstrating the location of each crystal centre. Along the bottom row, the sensitivity profile is simulated for a plan view of the corresponding geometry, integrated along the depth axis (z). A colour bar is shown illustrating the colour gradient of increasing sensitivity.

Optimal geometry simulation

The final optimised geometry is shown in Figure 4.5, with a high spatial resolution region of $42 \times 62 \times 20$ mm^3 corresponding to that of the eventual inclusion of the Polaris system shown within the larger modular camera FOV of approximately $120 \times 174 \times 102$ mm^3. Each BGO detector crystal is shown as a separate coloured pixel. At this stage, more care was taken in the calculation and measurement of the crystal positions, accounting for both light guide spacing between crystals as well as overall detector block angles on account of their trapezoidal shielding.

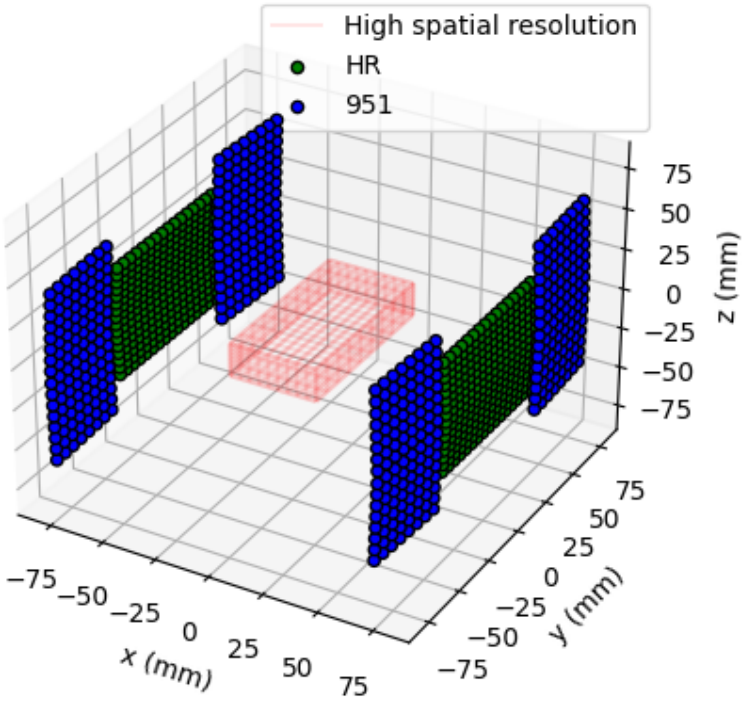

Figure 4.5: The geometry of the hybrid camera, showing each segmented BGO detector crystal as a separate pixel with colour corresponding to the detector block type. The shaded high-resolution region as expected from the Polaris system in the future hybrid camera is shown in the center.

The simulated sensitivity profile of the scintillator elements for the optimal geometry is shown as a plan view heat map in Figure 4.6. Since this simulation does not deal with absolute values of the sensitivity, relative sensitivities are displayed instead.

Qualitatively from the heat map, many of the expected characteristics of the profile are visible. The centre offers high sensitivity, as expected, overlapping with the high sensitivity region expected from Polaris in the future hybrid camera. In a larger region

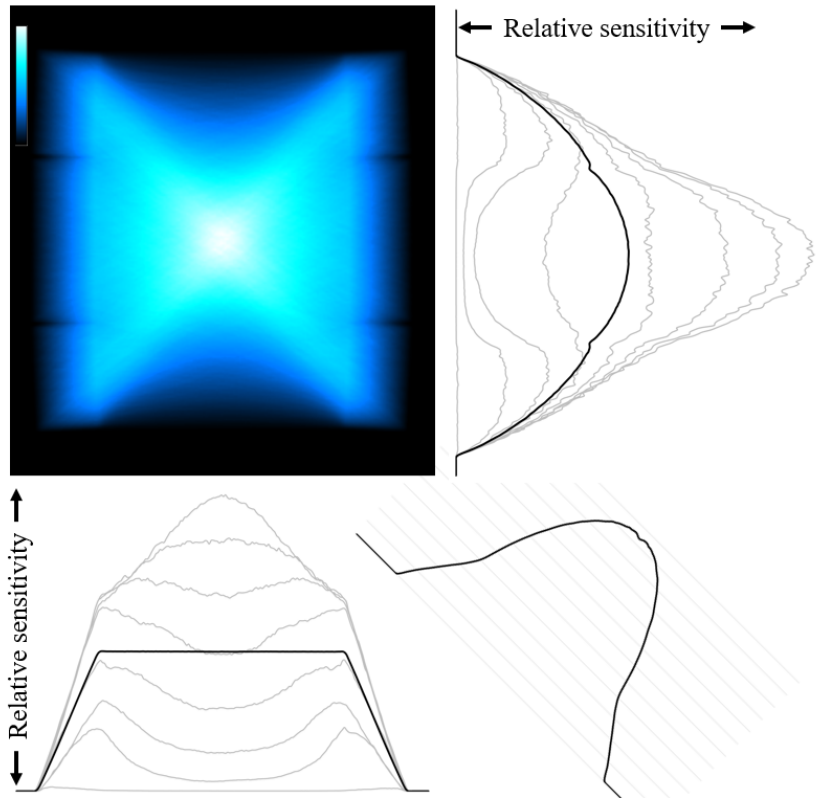

Figure 4.6: A plan view of the simulated sensitivity profile of the optimised modular scintillator camera, with the sensitivity integrated along the depth of the image. The colour scale is placed in the top left, demonstrating increasing sensitivity. Along the x and y axes, the sensitivity profile is integrated along the opposite axis and plotted at varying depths, with the mean profile shown in bold. In the bottom right, the mean sensitivity along both the x and y axes is shown as a function of depth.

surrounding the centre, a roughly uniform moderately sensitive region can be seen, enabling experiments to operate outside of the small high-sensitivity region of interest at the cost of sensitivity.

To confirm these qualitative observations, the sensitivity profile is integrated along each axis and displayed at varying depths, or z coordinates. Along the y axis (right) the highly sensitivity centre can be seen, as well as a notable drop in sensitivity at the depth extremities. This sharp change visible in the profiles along both the x and y axes is caused by the sampling depth crossing the boundary of the central HR+ block FOV, outside of which no coincidences between HR+ blocks are possible. Within the FOV of the central HR+ blocks the sensitivity increases significantly, as expected.

The main feature of the geometry is visible in the mean sensitivity along the x axis, where it appears to be constant. Of course, this has contributions from all depths but still demonstrates that a large, fairly uniform central FOV has been achieved along the x axis.

4.2.2 Construction

Following the decision on the final system geometry, several additional supporting pieces needed to be produced or acquired to ready the system for use.

The primary supports needed were those used to align the detector blocks into the correct geometry. The 951 and HR+ blocks are trapezoidal prisms with differing dimensions, and precise detector placement is required, especially for micro-scale tracking. To position the blocks such that their faces were aligned with one another as defined by the geometry, a 3D printed frame was used to support the base of each unit, as seen in Figure 4.7. These frames were then positioned with graphing paper approximately 12 cm apart, aligning the front of the frames with the lines of the paper to ensure positioning uncertainty of < 0.5 mm.

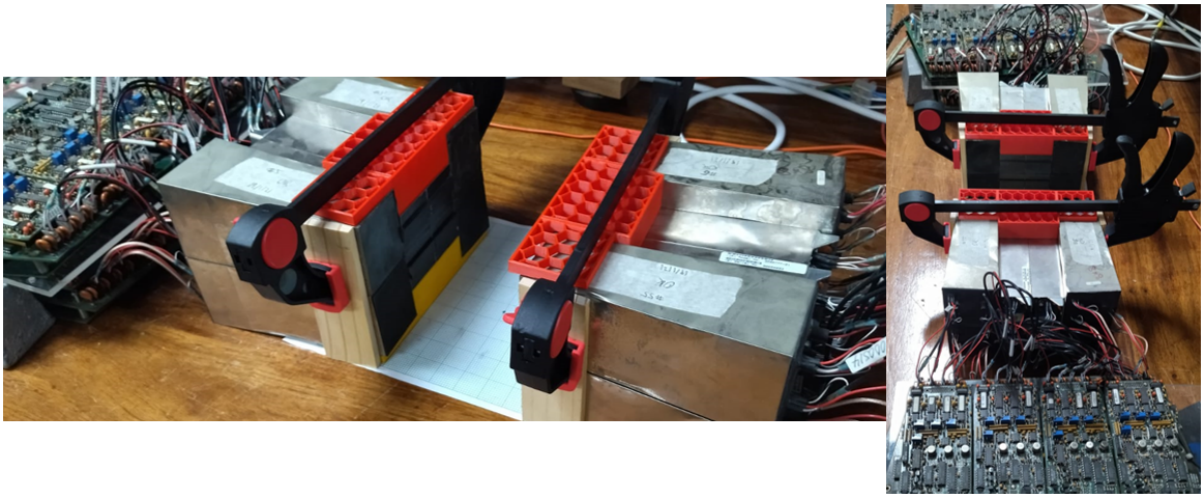

Figure 4.7: Two perspectives of the constructed scintillator array, showing each detection unit as well as the support structures and clamps.

For module controller support, large plates of Plexiglas were used, with dimensions arbitrarily larger than the controller. The lower controllers were placed directly onto the experimental surface, typically a table, and lead bricks were used to raise a Plexiglas plate above the lower controller such that additional controllers could be placed above without damaging their electronics.

From the geometry definition the placement of each detector block was set, but not the order in which they were connected to the controllers. To make this decision, the block cable lengths were considered, as the 951 blocks have very short cables limiting connection options. Therefore, modules of two 951 blocks connected to the outer channels on each controller and two HR+ blocks connected to the inner channels were used as this caused the least strain on the cables, mimicking the placement of the blocks themselves.

Finally, clamps were used to account for slight deformities in each block, as well as to secure each block in place, since the block cables tended to pull the detector blocks apart. To distribute the clamping force along the blocks, ensuring improved alignment and reducing the force on the fairly malleable block casing, small wooden blocks were placed on the sides of each unit.

Following the full construction of the system, the module controllers were connected to power supplies, using a split rail 5.0 V, -5.2 V and reference ground supply for the electronics, as well as a 1500 V high voltage supply for the PMTs. Every block and controller was reset to default parameters, and the upper and lower level energy discriminators were set as determined in Section 3.1.

Following this, a full calibration of each detector block was performed in terms of crystal uniformity, aiming to produce uniform block histograms. A Na-22 calibration source was placed approximately 6 cm from the centre of each block, and the built-in calibration process was run as described in Section 2.2.2, using 30-second histograms for the calibration. With sixteen BGO detector blocks each having four PMTs, 64 individual PMT gains were adjusted through this calibration.

Following an initial execution of the calibration process on each detector block, calibration success was evaluated through the acquisition of 10-second histograms of each block. In each case, the standard deviation of the number of events recorded in each crystal was compared to the uncertainty of the mean value and a block was considered successfully calibrated if the standard deviation was lower than the uncertainty. All HR+ detector blocks were considered successfully calibrated after a single execution of the built-in calibration process, typically offering a standard deviation of approximately half the uncertainty of the mean value, requiring no further adjustment. In comparison, of the eight 951 detector blocks only half were considered successfully calibrated after a single execution, with the difference in calibration performance likely resulting from the inconsistent, poorer construction quality of the older 951 blocks and PMTs in comparison to the newer HR+ blocks.

As a first additional calibration step, the built-in process was repeated on the unsuccessful blocks, with improvements expected as the gain adjustment procedure is iterative and subject to the choice of initial values. Following this repeat, two of the remaining four blocks were considered successfully calibrated. Finally, to address the remaining uncalibrated blocks, manual adjustments to the PMT gains were made through the study of their histograms following a 30-second acquisition. For regions in which lower or higher count rates were clearly visible, the corresponding PMT gain was adjusted accordingly. Through this process noticeable improvements were made to both blocks, however neither was considered fully successful.

With one block, a standard deviation within 10% of the mean uncertainty was achievable and was considered sufficient for this work. However, with the second block, a standard deviation 50% greater than the mean uncertainty was achieved. Additionally, through built-in and manual calibration, the optimal PMT gains were found to be the maximum possible value achievable through the module controller. This indicated potential hardware issues, and as such the block casing was removed and the block internals were repaired. With this repair, a slight improvement in calibration was achieved, but significant non-uniformity was still visible. Unfortunately, the calibration of these blocks could not be improved further and no additional 951 blocks were available for use with this system. As a first step in future work with the modular camera, these blocks should be repaired further or replaced.

Chapter 5

System characterisation results

5.1 System setup

Following construction as described in the previous section, the Anet A8 was placed above the setup as a positioning stage, enabling measurements in the system FOV through the use of the source holder, in which a Na-22 source with activity 20.11 ± 0.26 kBq, as of 24 July 2023, was placed. The final setup is shown in Figure 5.1.

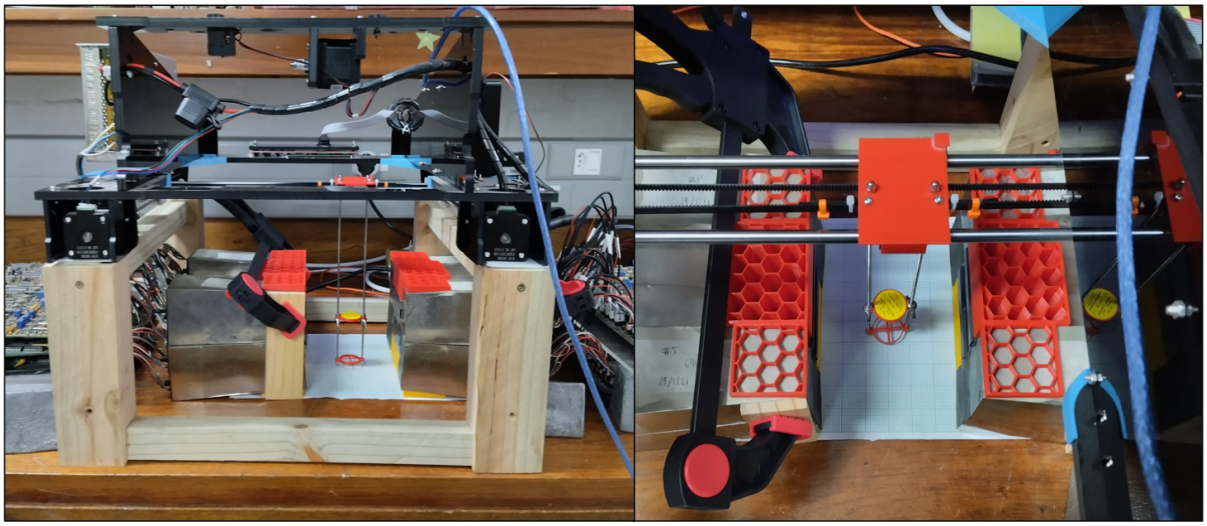

Figure 5.1: The Anet A8 placed on a custom wooden frame above the scintillator array, viewed as side-on (left) and top-down (right). Clearly visible is the wooden support structure holding the Anet, the 3D printed frames (red and yellow hexagonal honeycomb structures), the clamps used and the Na-22 calibration source (yellow disc).

Positioning uncertainty

The Anet is used to precisely position the source to reduce tracer positioning uncertainty and improve upon measurement consistency. However, there are still several sources of positioning uncertainty to consider.

The Anet itself has a quoted ±200 µm print head positioning resolution. However, the print head positioning resolution is dominated by the positioning and alignment uncertainty of the Anet as a whole with respect to the detector array. The positioning and alignment of the Anet relied on graph paper attached to the experimental surface, used for verification by positioning the source at various test positions before measurement. By confirming the accuracy of these positions by eye, any necessary adjustments can be made to the position of the Anet. However, this introduces additional uncertainty, partially due to graph paper inconsistencies, as it was not perfectly flat across its entire surface, and partially due to parallax error in confirming the positions. Finally, the position of the source within the calibration disk is assumed to be central in the horizontal plane, with an active radius of approximately 3 mm [45]. In the vertical direction, the source height is less than 1 mm, with the 3 mm thickness of the calibration disk introducing uncertainty as the vertical position of the source within the disk cannot be easily verified.

A separate positioning uncertainty factor, this time on the reconstructed positions from measurement as opposed to the expected positions from the Anet, arises due to the positioning and alignment of the detector blocks with respect to each other. Through the use of graph paper, 3D printed frames and clamps, much of the positioning and alignment uncertainty, estimated to be within a single detector crystal length for each corresponding block, has been reduced, however many of the effects from above apply in the same manner for the detector array. The uncertainty of measured positions arising from the detector array positioning is not analysed here, but several methods for reducing and accounting for the positioning and alignment uncertainty are mentioned in Section 6.2.4.

The above factors contribute to a positioning uncertainty roughly estimated to be on the order of 2 mm in each coordinate, primarily resulting from the Anet alignment with the external axes and the internal dimensions of the calibration source. This uncertainty is large in comparison to the desired micro-scale precision. However, in this work the majority of characterisation, such as system sensitivity and spatial resolution, is not performed relative to an absolute coordinate system, implying that the effects of this positioning uncertainty are minimal. The measurement of absolute system accuracy and the development of a warping correction map as discussed in Section 6.2.3 may require improved positioning uncertainty to achieve sub-millimetre absolute accuracy.

5.2 f-optimisation

Using the system set up as above, an f-optimisation procedure was performed as described in Section 1.2.1, initially for the centre of the system FOV, representing the high-resolution region, with subsequent investigation into the height dependence of the optimal f-parameter.

5.2.1 High resolution FOV

The calibration source was positioned centrally and acquisition was run first for one hour and then three times for five minutes each for statistical analysis. The data produced from acquisition was then run through the PEPT algorithm for varying values of f and N, outputting PEPT results such as the standard deviation of position and location rate

for each combination. The mean and standard deviation of each relevant PEPT result were then determined from the combination of all measurements and plotted as error bars below. In many cases, the results did not vary notably between measurements and the error bars are indistinguishable from points with the scale used.

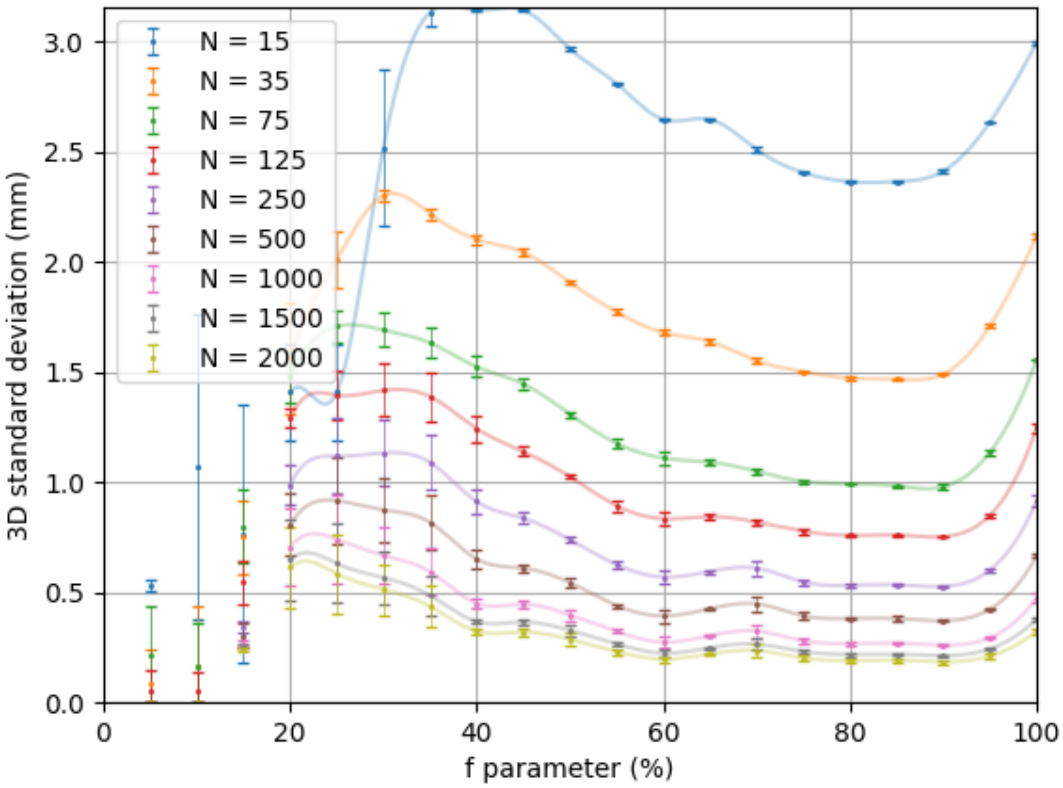

Figure 5.2: Mean 3-dimensional standard deviation of measured positions for a stationary central tracer particle as a function of the PEPT algorithm parameter f, for varying LORs per location N. Interpolating lines have been plotted for each N value from $f = 20\%$ for clarity.

In Figure 5.2, the mean 3-dimensional standard deviation of position is plotted for a selection of f and N values. The purpose of this plot is to identify the f parameter values giving the lowest mean standard deviation of the position in reconstruction such that this parameter can be used in further analysis for optimal accuracy. It can be seen that a value of f between 80% and 90% provides the minimum standard deviation for all choices of N. As such, an optimal f value of 85% was selected. To verify the validity of this choice, the average position determined through tracking was compared for choices of f between 80% and 90% and N between 15 and 2000, and in every case the resulting position agreed with both the expected position and all other reconstructed positions, varying by < 20 µm in each coordinate between different parameter choices.

With the selection of $f = 85\%$, an optimal value of N must still be determined for a

given system. Clearly, when increasing N the standard deviation of position is decreasing. However, an increase in N at fixed activity implies a decrease in location rate, as a larger fraction of LORs are required to produce a single location. Figure 5.3 demonstrates the relationships between the standard deviation and the location rate.

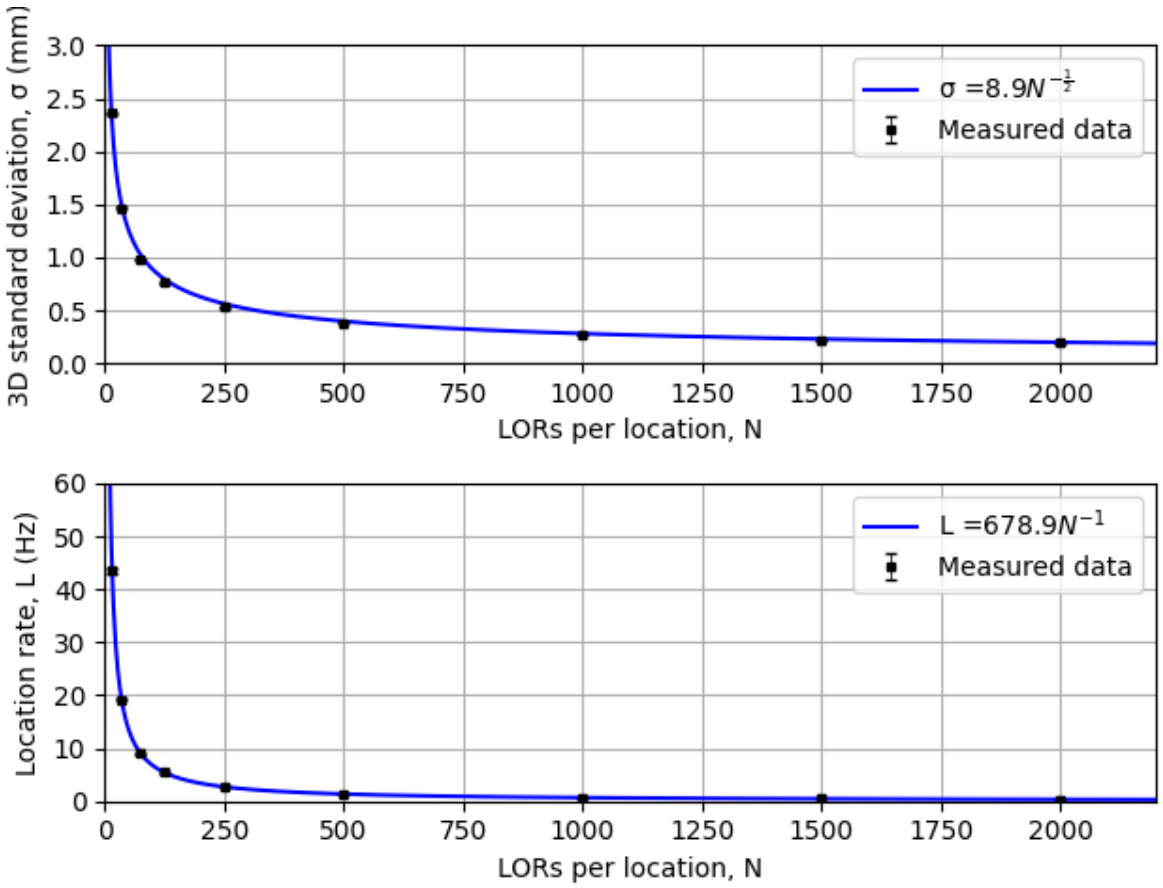

Figure 5.3: Mean 3-dimensional standard deviation (top) and location rate (bottom) plotted against the numbers of LORs used per location N. Fitted curves of expected $\frac{1}{\sqrt{N}}$ (top) and $\frac{1}{N}$ (bottom) dependencies have been overlaid.

As described in Section 1.3, the PEPT location uncertainty has a $\frac{1}{\sqrt{N}}$ dependence, whereas the location rate depends simply on the number of LORs required to produce a single location. For example, requiring $2N$ LORs to produce a location results in a halved location rate, implying the location rate has a $\frac{1}{N}$ dependence. These functional dependencies have been fit to the measured data in Figure 5.3, providing a valuable way of selecting an ideal N value depending on experimental requirements. For example, an experiment with a fast-moving, large tracer particle may require a high location rate and sacrificing spatial resolution may be acceptable, whereas a slow-moving system at very small scales may optimise for spatial resolution at the cost of location rate.

To make this trade-off between spatial resolution and location rate clearer, the factor of N can be eliminated by equating their proportionalities and rearranging, determining a $\sigma \propto \sqrt{L}$ relationship between standard deviation and location rate for the specific

geometry of the modular camera. In Figure 5.4 this relationship is generalised to the location rate per unit activity, L', demonstrating a maximum of 0.45 Hz/kBq for sub-millimetre standard deviation. For given experimental requirements, this curve can be referenced to identify the optimal trade-off between spatial resolution and location rate, and from that decision an optimal value of N can be found.

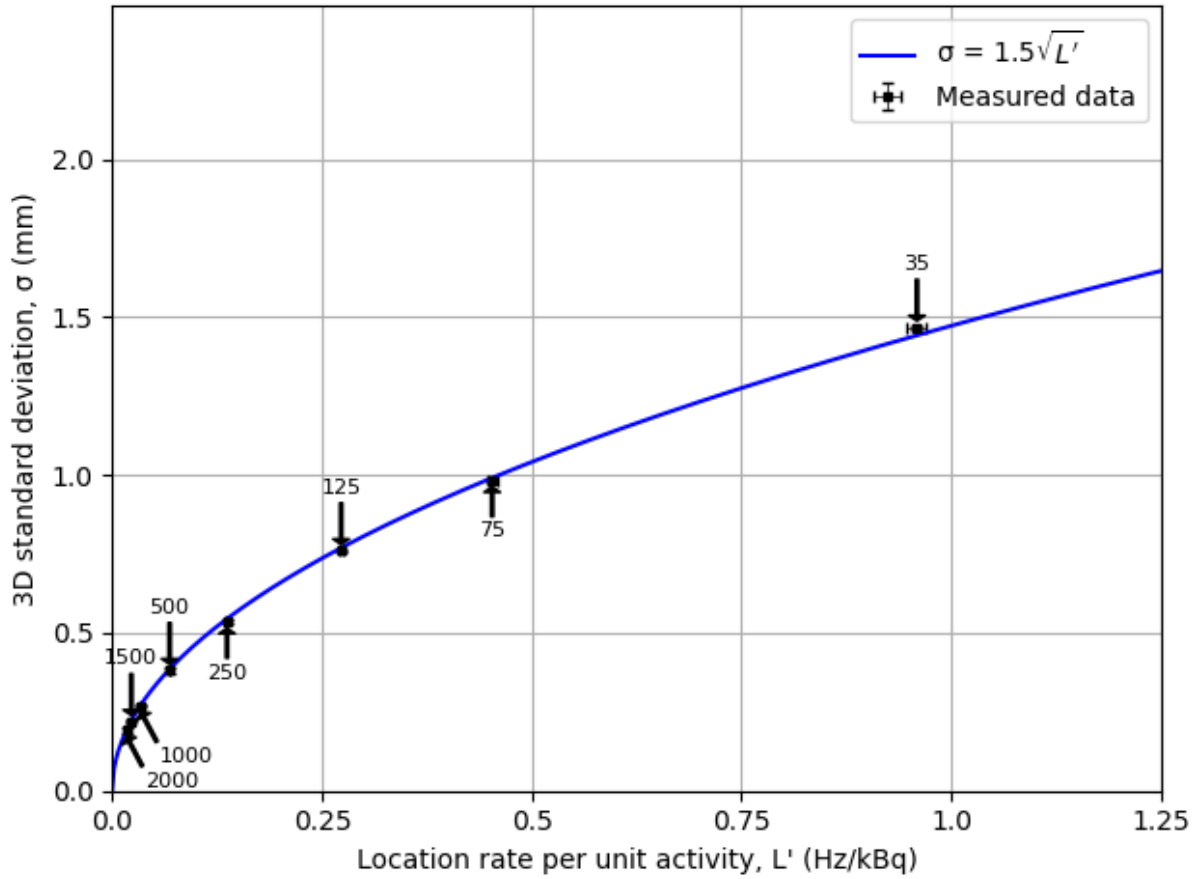

Figure 5.4: Mean 3-dimensional standard deviation, σ, plotted against location rate per unit activity, L', with fitted $\sqrt{L'}$ dependency. From the fitted curve, it can be seen that a sub-millimetre standard deviation is achievable at a maximum of 0.45 Hz/kBq. Each data point is labelled with the N value used to produce the result.

Coordinate dependence

In the above analysis, the 3D standard deviation of measured positions was used to estimate the precision of the system as a function of the tracking parameters. In this case, the standard deviation of each coordinate was summed in quadrature to produce a 3D equivalent. However, an understanding of the system precision in each coordinate may demonstrate the primary contributions to the total system precision, enabling further refinement of the camera design.

To investigate the tracking precision in each coordinate, the above f-optimisation procedure was repeated, using the standard deviation of each measured coordinate sepa-

rately as opposed to the combined 3D standard deviation. Once again, curves of standard deviation are plotted as a function of the tracking parameter f for a selection of N values, shown in Figure 5.5.

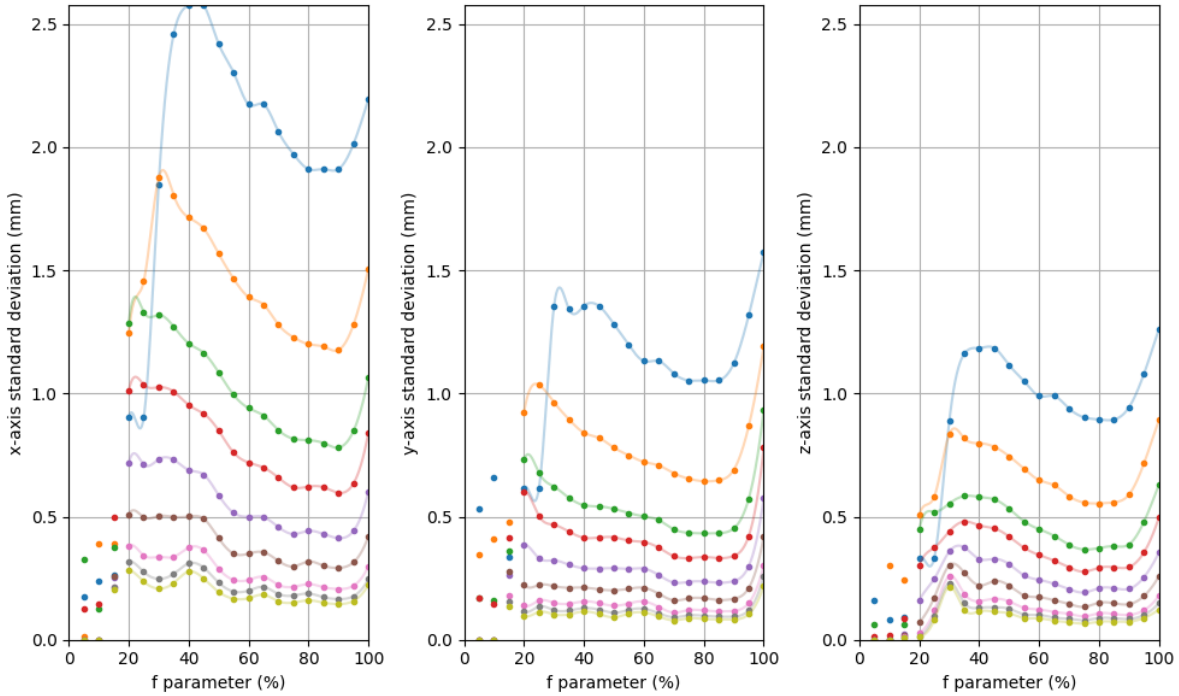

Figure 5.5: Standard deviations of each coordinate for a stationary central tracer particle, plotted as a function of the PEPT algorithm parameter f for varying LORs per location N. Interpolating lines have been plotted for each N value from $f = 20\%$ for clarity. Each coordinate axis is defined by the geometry shown in Figure 4.5.

Between each coordinate, approximately the same relative dependence on tracking parameters is seen, achieving optimal values of f between 75% to 90% as expected from the 3-dimensional analysis above. The primary difference between each coordinate is therefore the magnitude of the standard deviation for a given set of tracking parameters, in which the y and z coordinates are similar but the x coordinate is markedly larger.

To compare the standard deviation magnitudes of each coordinate more clearly, the $N = 500$ case is plotted in Figure 5.6, with each coordinate curve plotted on the same axis. The noted magnitude differences are visible here, with the standard deviation of the x coordinate approximately twice that of the y and z coordinates for most choices of f. For all choices of N with f values between 60% and 90%, representing the region in which the standard deviation is approximately uniform, the standard deviation in the x coordinate was determined to be approximately 90% greater than that of the y coordinate on average. In comparison, the standard deviation in the y coordinate was determined to be approximately 15% greater than that of the z coordinate on average.

Therefore, this discrepancy indicates that tracking is achievable to higher precision in the y and z coordinates than the x coordinate, which is defined as the axis between the detector faces. For parallel plate PEPT systems and other related geometries, such

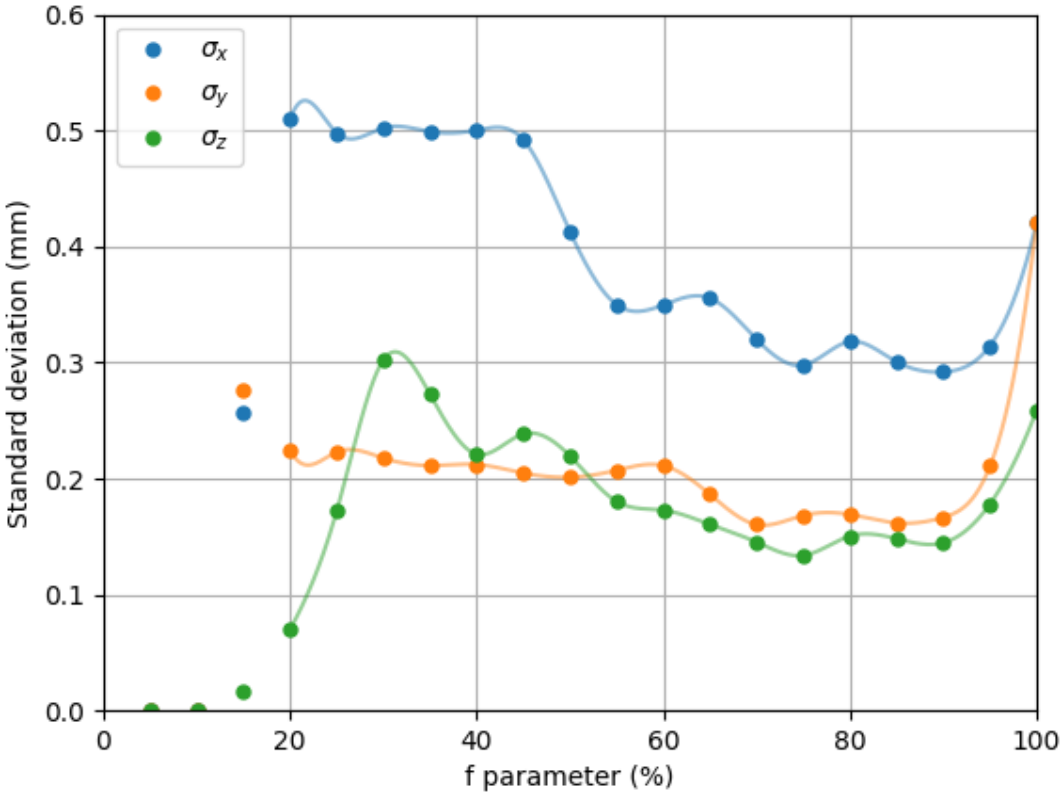

Figure 5.6: The standard deviation of each coordinate for a stationary central tracer particle, plotted as a function of the PEPT algorithm parameter f for 500 LORs per location, $N = 500$. Interpolating lines have been plotted for each N value from $f = 20\%$ for clarity. The coordinate axes are defined by the geometry shown in Figure 4.5.

as the modular camera, this discrepancy is expected as a result of angular sampling considerations. For any measured true coincidence, a right-angled triangle can be defined with sides α, β and opening angle θ, as shown in Figure 5.7. Through a collection of such LORs, the measured x coordinate is therefore found as the value of α, determined by the values of β and θ which can be calculated through knowledge of the spacing and dimensions of the detectors. The corresponding uncertainty of the x coordinate can therefore be calculated, identifying a term dependent on $\tan^{-1}(\theta)$ which grows to infinity as the detector spacing is increased, or the opening angle θ is decreased. In the y and z coordinates the inverse tangent term does not appear, instead replaced by a tangent term which grows to infinity as the detector separation is reduced. Therefore, low precision in the coordinate between the detector faces is expected as the detector separation is typically large in comparison to β.

In the design of experimental applications, this precision discrepancy may be handled through the optimisation of application orientation, such that optimal precision is achieved in the relevant positions and coordinates. Alternatively, to improve upon the

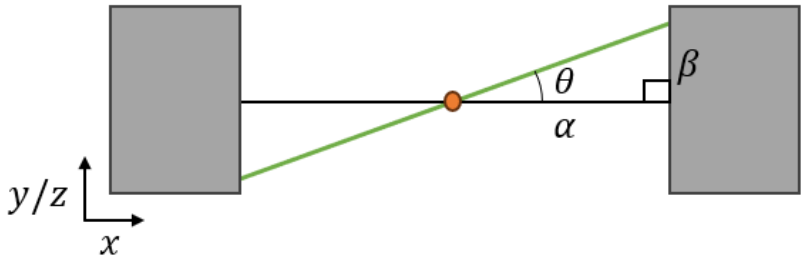

Figure 5.7: The right-angled triangle defined by a measured LOR (green) between two arbitrary detector blocks (grey). The distances α, defined as the distance along the centre line between the detector and the tracer, and β, defined as the distance between the detection crystal and the centre line, are shown as well as the corresponding opening angle θ. The figure is plotted in two dimensions for simplicity but can similarly be extended to three dimensions.

precision discrepancy, detector spacing may be optimised, or additional detector units may be used in future systems. Additional units should be placed perpendicular to those of Figure 4.5, such that optimal precision may be achieved in each coordinate through each opposing pair. This possible solution further motivates the use of the Polaris system in a hybrid camera, as an optimised geometry enables Polaris to be placed perpendicular to the current modular camera, ensuring an optimal central spatial resolution in each coordinate.

5.2.2 Height dependence

The above analysis is typical of larger, continuous geometries as in existing PEPT systems. However, with small modular geometries, especially those with FOV discontinuities caused by irregular detector block positioning, the optimal f value is expected to vary significantly as regions of considerably higher and lower sensitivity are explored by the tracer. In addition, with such few detector blocks, slight defects in detector response contribute more noticeably, especially in regions of low sensitivity.

To investigate the height dependence within the system FOV of the optimal f parameter, the calibration source was placed centrally in horizontal planes of varying height, between $z = -4$ cm and $z = 4$ cm in steps of 2 cm. The same f optimisation was performed as above with 30-minute measurements, generating Figure 5.8. For the $z = -2$ cm and $z = 2$ cm planes, it can be seen that the optimal f parameter does not vary significantly with the $z = 0$ cm case, remaining approximately around 80% to 85%.

However, notable variation occurs where the tracer particle leaves the FOV of the HR+ detector blocks, resulting in a reduction of the number of coincident pairs of crystals detecting true coincidences, markedly reducing the system sensitivity. With $z = 4$ cm the optimal f value reduces to between 45% and 55%, and with $z = -4$ cm the optimal f value reduces to between 60% and 70%, implying an increased random to true coincidence ratio in these regions.

This result implies that the choice of f needs to take into account the experimental

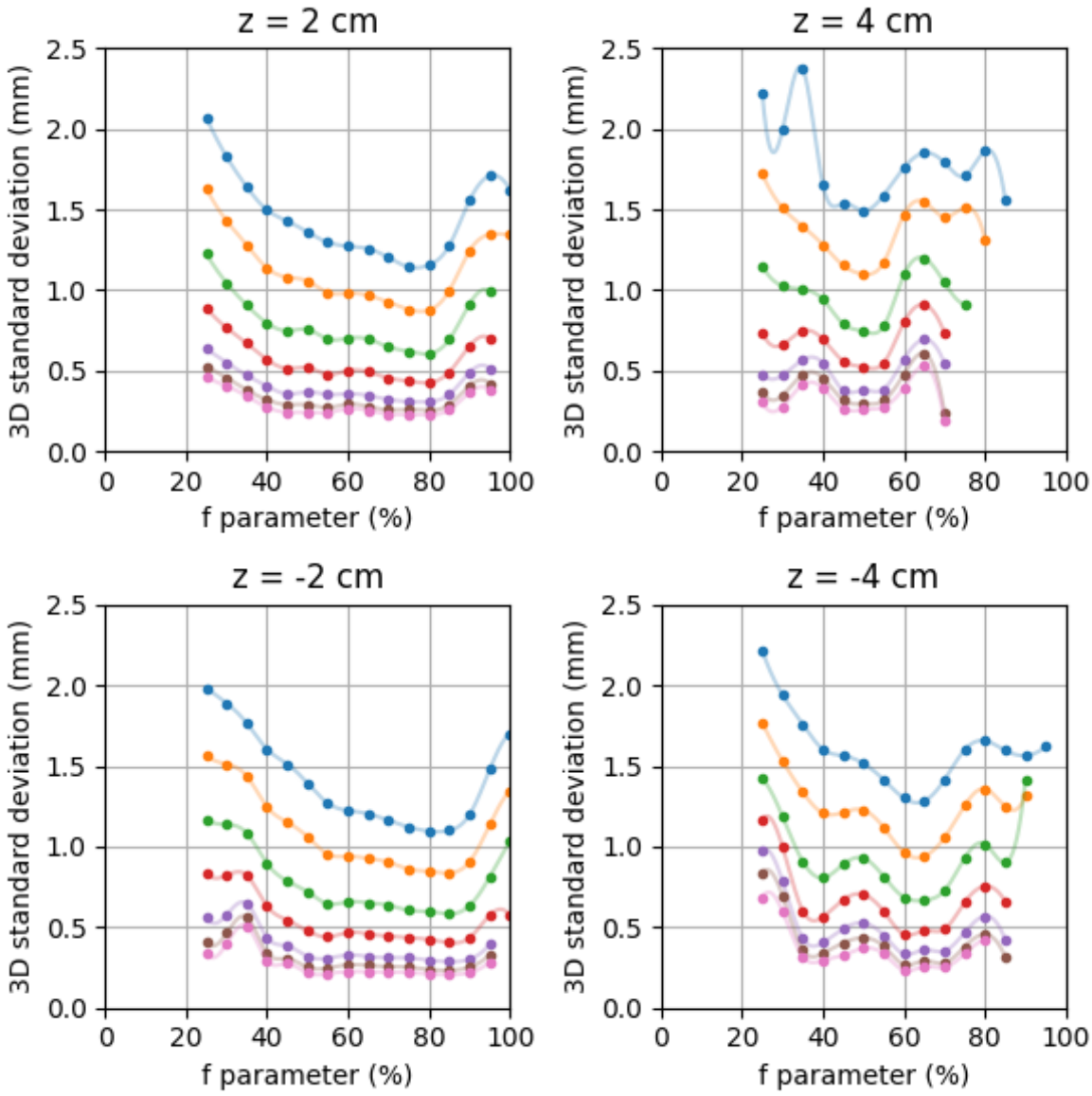

Figure 5.8: Mean 3-dimensional standard deviation of measured positions for a stationary tracer particle at various heights as a function of the PEPT algorithm parameter f, for varying LORs per location N. Interpolating lines have been plotted for each N value for clarity. In the $z = \pm 4$ cm cases, the PEPT algorithm could not converge on locations for large f, likely a result of an increase in random coincidences from the HR+ blocks.

FOV. For an application remaining within the HR+ FOV, an f parameter of approximately 85% may be used, achieving the optimal spatial resolution at all heights. If the required FOV is larger, including regions that are not within the HR+ FOV, the f parameter drops to approximately 55%, producing a consistent response throughout the system FOV, but at a lower precision for the high-sensitivity regions. One way around this issue may be the use of alternative tracking algorithms or dynamic, spatial-dependent

f parameter calculation, discussed in Section 6.2.5.

5.3 Characterisation profiles

5.3.1 Experimental procedure and analysis

With the system set up as previously described, three-dimensional profiles of various characterisation parameters such as sensitivity and spatial resolution were required. To achieve this, the Anet positioning stage was used to position the source throughout the system FOV at predefined positions.

A 5×7 grid, equally spaced in the ranges $x = (-32, 32)$ mm and $y = (-70, 70)$ mm, was used in horizontal planes, with 300 seconds of stationary data acquisition at each point. The bounds of the measured planes in the x direction (between each unit) were limited by the extent of the source holder, whereas the bounds in the y direction were limited by the Anet mechanism positioning in relation to each detector unit's clamps. Similarly to the f-optimisation procedure above, five separate, equally spaced horizontal planes were used in the range $z = (-40, 40)$ mm, with only three planes within the FOV of the HR+ blocks. Despite the FOV limitations, the primary region of interest for the system was addressed and may be extrapolated to the edges of the system FOV.

In each plane, the full grid of 35 positions was measured in a single acquisition to reduce additional positioning uncertainties arising from the movement of any system elements between runs. The measurement of each plane was repeated 3 times to provide information on the systematic uncertainties involved. In all analyses the uncertainties arising from Poisson counting, for measurements of rates such as singles or sensitivity, or spatial resolution, for measurements of system accuracy or precision, dominated the uncertainties arising from repeat measurements. Despite this, uncertainties from all sources were propagated through analysis. These repeat measurements were performed without the movement of the system, however, in the adjustment from one plane to another Anet movement was required and system recalibration was performed in terms of the positioning and alignment of the Anet.

Once acquisition at every position had been performed, singles, prompt coincidence and random coincidence rates were extracted at each position. In addition, the PEPT tracking algorithm was applied to each dataset, from which location rates, measured average position and standard deviations were extracted for each position. Throughout the full FOV, values of $f = 55\%$ and $N = 500$ were used in tracking as determined by the f-optimisation above to produce comparable results throughout the entire system. For a more precise investigation of the HR+ FOV, values of $f = 85\%$ and $N = 1000$ were used in additional analysis, leveraging the improved spatial resolution of the region while maintaining useful location rates.

Since the effects of the tracking algorithm parameters f, N have been discussed and demonstrated in Section 5.2 for the central position, the results obtained through tracking were normalised such that the positional dependence could be investigated independently, noting that the absolute values may vary depending on parameter choices.

Profile plotting

From the measurements as described above, figures of a similar format to those of the simulation (see Figure 4.6) were generated. These figures feature a two-dimensional plan view contour plot, illustrating values of a specific characterisation parameter, such as sensitivity, averaged along the depth of the system. Detector block faces, highlighted in blue (951 blocks) and green (HR+ blocks), are overlaid on the contour plot for clarity.

Along the x and y axes of the contour plot, corresponding profiles for each horizontal plane of measurement are plotted, with each point averaged along the opposite axis. For example, the top profile presents the x dependence of the characterisation parameter for each horizontal plane, averaged along the y-axis at each point. The mean profile, averaged across all horizontal planes, is depicted as an interpolated solid black line in each profile.

Where normalisation has been performed, such as for the standard deviation, each measured value is divided by that of the central position ($\vec{x} = (0, 0, 0)$ mm) before averaging or plotting. As the central position typically represents optimal performance, such as maximal sensitivity or minimal standard deviation of measured positions, the corresponding averaged profiles are unlikely to have a value of 1 at any point, as the contributions of several positions are included in the averaging process.

5.3.2 Singles rate

While single detections are not typically used for tracking in PEPT, an understanding of the singles event rate can provide a general understanding of the prompt and random coincidence rate, being functions of the single event rates in each coincident detector pair, as well as being useful in verifying the operation of each detector block.

The singles rate at any position in the system FOV is the summed contribution of singles events from all detector blocks, corrected for background detections with corresponding uncertainty propagation. To measure the background singles rate, data was acquired for one hour with no source present, with the summed rate from all detector blocks determined to be 166.93 ± 0.22 Hz, much lower than the singles rate measured with a source present of approximately 3 kHz.

For each block, the singles rate depends on the source distance from the block as well as the block calibration, varying between block types and between blocks of the same type due to manufacturing tolerances and lifetime wear.

As a summed total, the singles rate also depends on the effective geometric efficiency of the detector system in relation to the position of the tracer particle. Considering the response of a single unit, or one side, of the modular camera, the geometric efficiency is expected to be the largest close to the centre of the unit face, decreasing as a function of the radial distance to this point. In Figure 5.9 this expectation is met, with the contribution of both sides of the system leading to a fairly consistent singles rate throughout the measured FOV, decreasing by a maximum of 20% within the HR+ FOV and a maximum of 40% towards the outer edges of the full measured FOV.

Of note however is the difference between the -40 and 40 mm planes, visible in the negative y direction of the corresponding profiles. This is likely caused by the contribution of the poorly calibrated 951 block on this side, which was noticed in the original setup

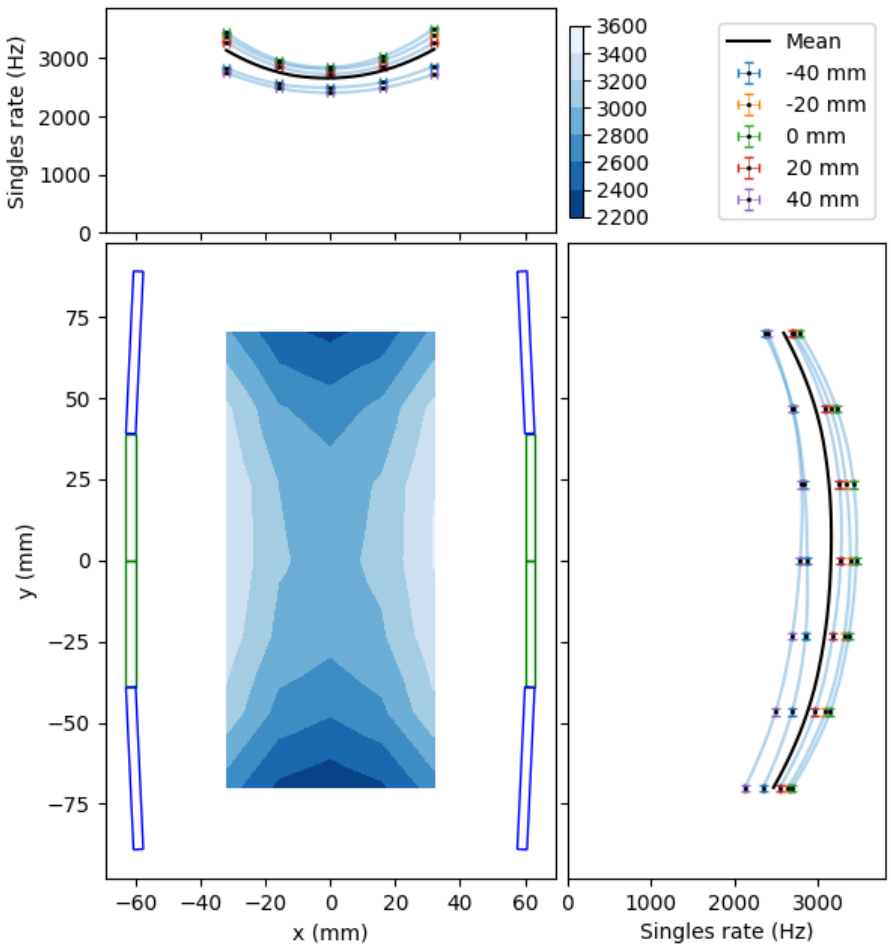

Figure 5.9: The singles event detection rate in Hz as a function of position in mm, plotted as described in Section 5.3.1.

and calibration of the system. Throughout further characterisation, the contribution of this block will be studied, possibly requiring replacement if results are shown to be insufficient.

5.3.3 Sensitivity profile

System sensitivity is of significant importance to the performance of a PEPT system. Typically given as a ratio of the true coincidence detection rate and the corresponding source activity, in a PEPT context the sensitivity determines the frequency of LOR measurements for a given source strength. Since tracking is performed with these LORs, a larger sensitivity implies an improvement in tracking capabilities for a given source strength, and as such a good understanding of the sensitivity profile of a system is required, both for system calibration and experimental planning or analysis purposes.

Since the sensitivity of a system involves only true coincidences, the coincidence rate was corrected for random coincidences, accounting for events in which one or both of

the detected photons either did not originate from the same annihilation event within the tracer, or did not originate from the tracer at all as in background events. Random coincidence count rates were determined using a variable timing shift on one side of the detector system, such that any detected coincidences were random detections. In all cases, the random coincidence rate was less than 1 Hz, which was expected due to the low activity of the tracer and the optimised short coincidence window.

To compute the sensitivity the tracer activity was required, which was determined for the calibration Na-22 source with uncertainty in Section 2.3 to be 20.11 ± 0.26 kBq as of 24 July 2023. For each following measurement, the measurement date was recorded and the expected activity of the tracer was determined with propagated uncertainty.

From the above, the system sensitivity at a given position was determined as a function of the total number of prompt (P) and random (R) coincidences, as well as the tracer activity at measurement time (A_t) and the duration of measurement (t), to be $S = \frac{P-R}{tA_t}$. In the central position ($\vec{x} = (0, 0, 0)$ mm) the measured maximum sensitivity was determined to be 34.8 ± 0.6 cps/kBq. Profiles of the system sensitivity S are plotted in Figure 5.10 as described in Section 5.3.1, and can be compared to the simulated results of Figure 4.6.

Qualitatively, the sensitivity contour plot approximately matches that of simulation and expectation within the limited measurement FOV, peaking towards the centre position with a slow decrease of sensitivity while within the HR+ FOV, dropping off considerably as the source leaves this higher resolution region.

A fairly uniform x dependence of the sensitivity can be seen in all planes besides the central plane, producing an approximately uniform x dependence of the mean sensitivity as expected from the simulation. In the central plane, a pronounced peak of the sensitivity is visible about $x = 0$ mm, also expected from the simulation.

Within the HR+ FOV, peaking of the sensitivity about $y = 0$ mm is visible and expected, with the sensitivity dropping off considerably as the tracer moves out of this region whether in the horizontal or vertical direction.

Unexpectedly, varying the source height in the positive z direction leads to a greater decrease in sensitivity than in the negative z direction, as can be seen in each of the corresponding profiles. In addition, the sensitivity decrease in the negative y direction is greater for these planes, as seen in the contour plot and the corresponding y-axis profiles. If the system were truly symmetric in detector response, these profiles for $\pm z$ would overlap.

At this stage, since tracking is not yet being performed, errors in system geometry and detector block placement are unlikely to cause these differences, with minimal detector block positioning uncertainty in the vertical direction. Instead, these differences are likely a result of the previously mentioned block calibration issues, causing a maximum reduction in sensitivity of the planes at positive heights of approximately 15% in comparison to the planes at negative heights.

Location rate

To identify the effects of the sensitivity profile on the tracking capabilities of the system, the PEPT tracking algorithm was applied at each measured position. The location rate of the system, or how frequently the tracking algorithm can produce a measured location

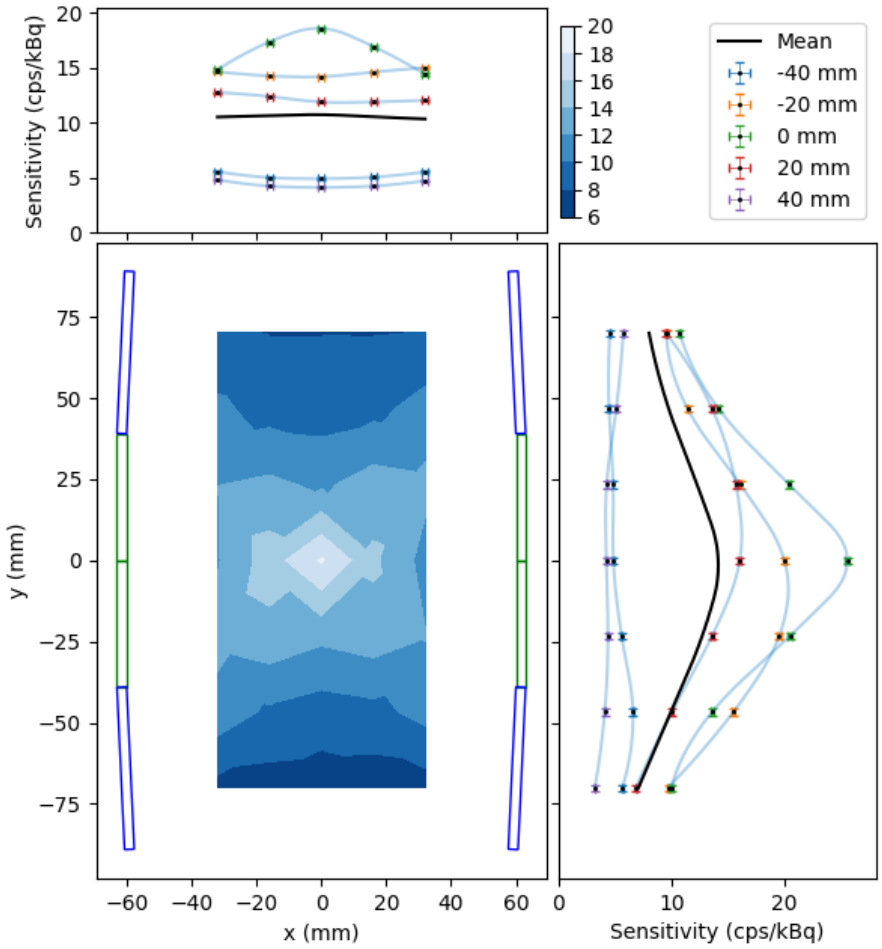

Figure 5.10: The system sensitivity, given as counts per second per kBq of source activity, as a function of position in mm, plotted as described in Section 5.3.1.

for a given set of LORs, was determined and normalised to the value at the central position. Since the location rate depends upon the true coincidence rate, the structure of the location rate profiles, plotted in Figure 5.11, are expected to be approximately identical to that of the sensitivity profile. In comparison to the sensitivity profile in Figure 5.10, the expected similarities are visible, with both plots containing much of the same structure.

However, a slight difference is visible between the sensitivity and location rate profiles at the top and bottom of the system FOV ($z = \pm 40$ mm), outside the FOV of the HR+ detector blocks. Specifically, the location rate is slightly lower than expected about $y = 0$ mm for x values closest to the detector faces, causing a slight drop in the corresponding profiles. In these positions, true coincidences are only measured between a few 951 detector crystals at high incident angles. As such, an increased fraction of random coincidences is expected, as the singles rates in the nearest HR+ detector blocks are expected to remain high while contributing no true coincidences. Therefore, the optimal value of f in these positions may be lower than the value used, with infrequent

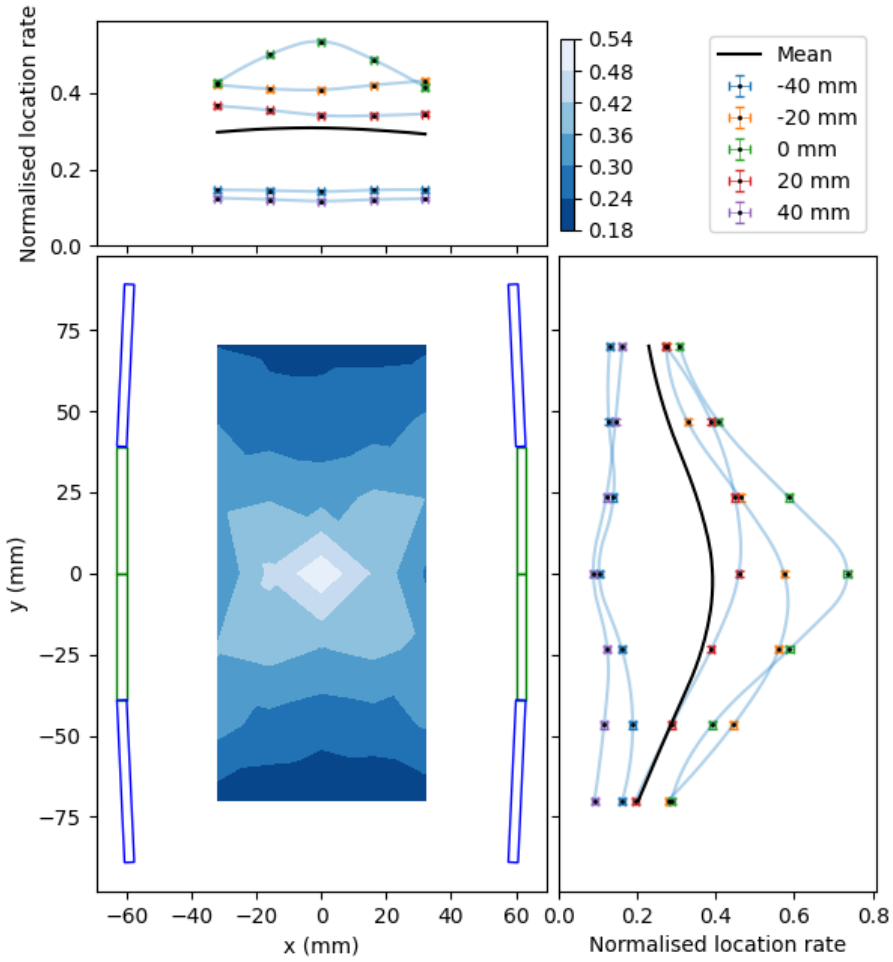

Figure 5.11: The normalised location rate as a function of position, plotted as described in Section 5.3.1. Normalisation was performed in relation to the location rate in the central position ($\vec{x} = (0, 0, 0)$ mm).

position convergence difficulties causing a slight reduction in location rate. In addition, at large angles, incident photons may penetrate into adjacent detector crystals as photon attenuation is optimal for rays perpendicular to the detector faces. This phenomenon effectively broadens the point spread function of the block, reducing the spatial resolution at high detection angles, and possibly also causing infrequent convergence issues in these low spatial resolution positions.

Summary and discussion

The sensitivity profile of the modular camera has been measured and analysed above. A maximum central sensitivity of 34.8 ± 0.6 cps/kBq has been achieved, several orders of magnitude greater than the Polaris system which achieved < 1 cps/kBq. In addition, the structure of the sensitivity profile approximately matched that of the simulation, remaining sufficiently uniform such that potential deadtime limiting hotspots were avoided.

Considering the full system FOV, a mean sensitivity of approximately 10 cps/kBq was achieved. As described in Section 1.2.2, a micro-scale tracer particle of 50 µm diameter may achieve a maximum activity of approximately 600 kBq through ion exchange methods. Assuming no deadtime effects and therefore a linear response, a mean true coincidence rate of approximately 6 kHz may be achieved with this tracer, with a maximum central rate of approximately 21 kHz. For a precise measurement of the optimal tracer particle activity, analysis of the system deadtime parameters must be performed as described in Section 6.2.2.

Following analysis of the sensitivity profile, the location rate profile was determined through the application of the PEPT algorithm. Since the location rate strongly depends on the corresponding true coincidence rate, these profiles were nearly identical in structure, with slight differences attributed to infrequent position convergence issues caused by notable reductions in spatial resolution.

With the calibration tracer particle of 20.11 ± 0.26 kBq, a maximum sub-millimetre location rate of 11.1 Hz was achieved in the central position, as seen in Figure 5.4. To estimate achievable location rates a linear response is again assumed, achieving a maximum central location rate per unit activity of 0.55 Hz/kBq. Therefore, with the above 600 kBq micro-scale tracer particle, a central sub-millimetre location rate of approximately 330 Hz may be achievable. However, a linear assumption may not accurately describe the activity dependence of the location rate, with increased random coincidences affecting the achievable spatial resolution and location rates. Through analysis of the system deadtime parameters, an accurate measurement of the maximum location rate may be performed in future.

5.3.4 Spatial resolution

To address phenomena on the micro-scale, a PEPT system must be able to locate the tracer particle with micro-scale precision. To quantify the spatial resolution of the system, the standard deviation of measured tracer positions is used, determining the three-dimensional spread in measured locations for a given position.

As discussed in Section 1.3, the spatial resolution is a function of the true coincidence rate and the underlying spatial resolution of the detector blocks. Therefore, regions of higher sensitivity, which can be determined through Figure 5.10, are expected to have improved spatial resolution or lower standard deviation in repeated position measurements. However, the extremities of the measured FOV are expected to have less predictable behaviour with varying contributions of different detector blocks, each with different underlying spatial resolutions as a result of their differing pixel densities, calibration and angles relative to the source position.

Looking first at the full measured FOV, tracking parameters of $f = 55\%, N = 500$ were used to produce consistent results throughout the system. With these parameters, a minimal standard deviation of 0.467 ± 0.005 mm was found in the central position, to which each other position was normalised. In this section, the structure of the horizontal planes outside the HR+ FOV will be discussed, as those within the higher resolution FOV will be focused on in the following subsection, making use of improved tracking parameters.

For the $z = \pm 40$ mm planes, a significant increase in standard deviation can be seen

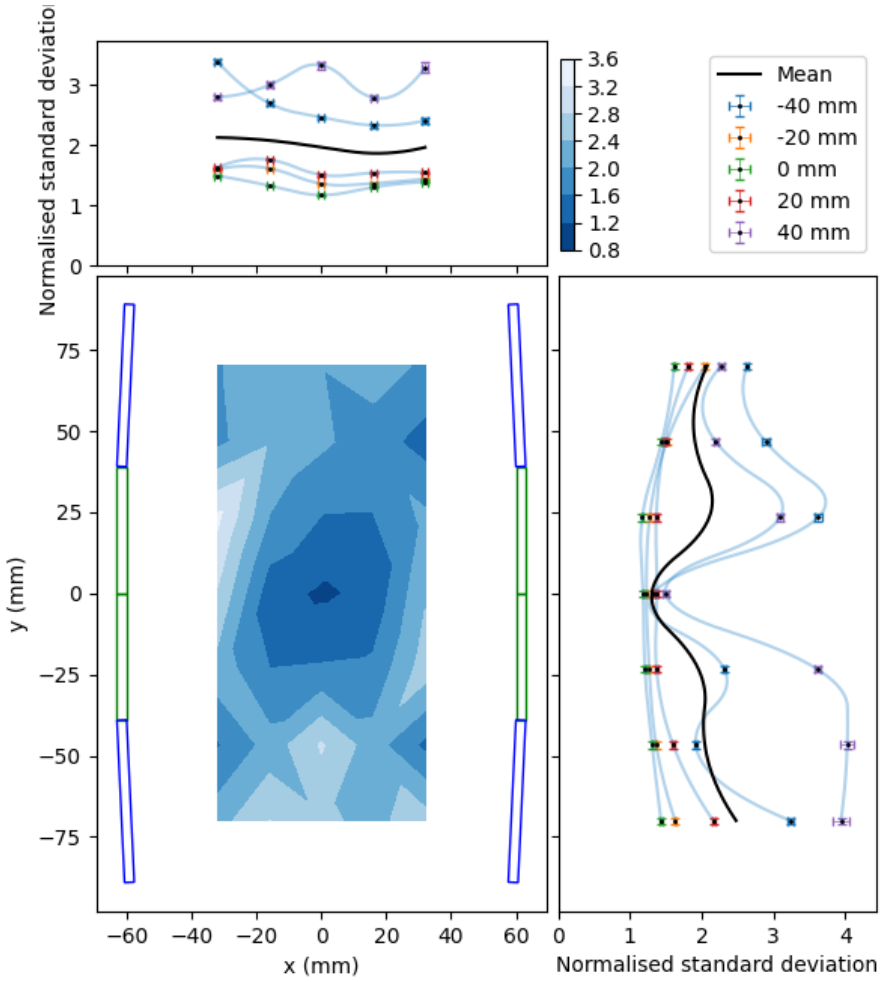

Figure 5.12: The normalised 3D standard deviation as a function of position, plotted as described in Section 5.3.1. Normalisation was performed in relation to the standard deviation of the central position ($\vec{x} = (0, 0, 0)$ mm).

in Figure 5.12 in comparison to those planes within the HR+ FOV. This is expected, as much fewer detector elements contribute to position reconstruction in these planes, with only a few crystal rows of four 951 detector blocks contributing. As such, these planes are more sensitive to small variations in detector block calibration and positioning uncertainties. Therefore, it is not particularly illustrative to analyse finer details in the structure of these planes, and instead general trends and extreme behaviours will be noted.

For instance, a minimal standard deviation is achieved about $y = 0$ mm in each plane, approximately matching those planes within the HR+ FOV. This indicates that the system would maintain approximately uniform precision for a tall experimental region of interest. However, as y is increased from zero the standard deviation of these planes increases notably and unpredictably, indicating that a tall experimental region would need to be narrow in the y direction.

Once again, in the negative y direction a large increase of the standard deviation is

visible within the positive plane, offering significantly reduced precision, likely as a result of the previously discussed detector block issues. However, this can now be seen to a lesser extent in the opposite direction, with the positive plane offering improved precision over the negative plane. Similarly, in the negative x direction, the standard deviation of the negative z plane reaches a maximum above that of the positive plane at the approximate position of the other poorly calibrated 951 block, as discussed previously.

Towards the extremities of the FOV, the standard deviation peaks at approximately four times the central value, indicating that the upper limit on system precision can now be determined following f-optimisation in the central position.

High resolution region

For clarity, the planes within the HR+ FOV are focused on in Figure 5.13 to demonstrate the capabilities of the system within this higher resolution region, using the tracking parameters $f = 85\%, N = 1000$ as earlier determined. With these parameters, a minimal standard deviation of 0.279 ± 0.002 mm was found in the central position, to which each other position was normalised.

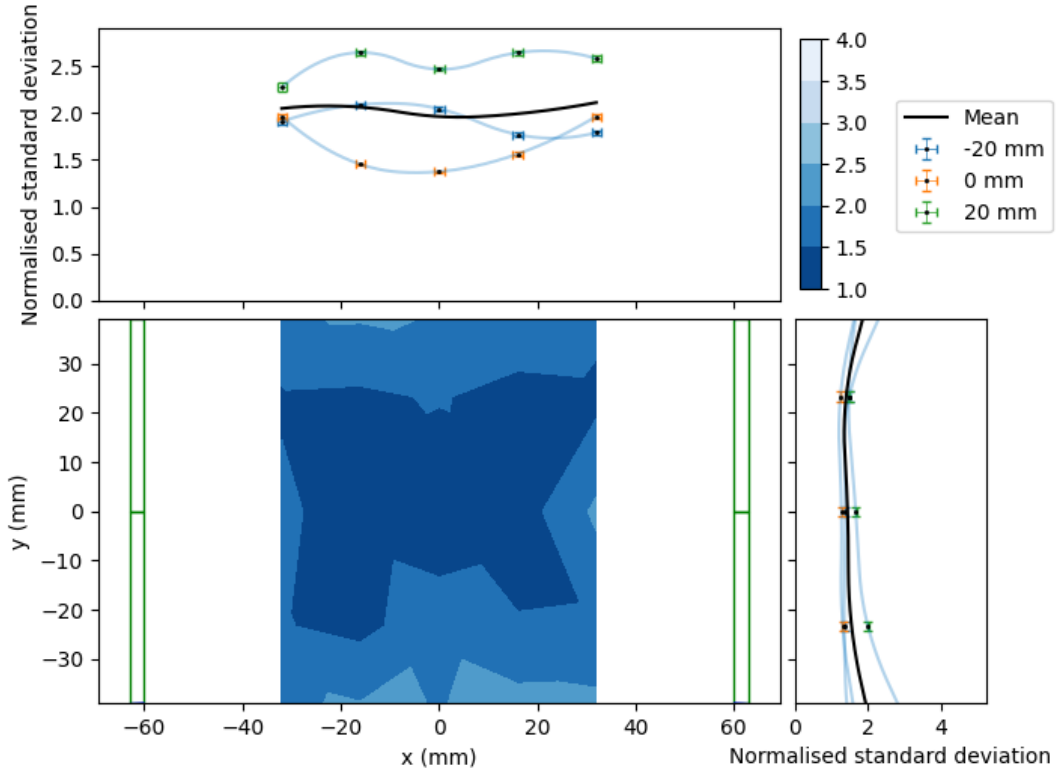

Figure 5.13: The normalised 3D standard deviation as a function of position, plotted as described in Section 5.3.1 for the high resolution HR+ FOV. Normalisation was performed in relation to the standard deviation of the central position ($\vec{x} = (0, 0, 0)$ mm).

In the contour plot, a large region of relatively uniform minimal standard deviation is visible in the centre, covering much of the HR+ FOV, as desired for a micro-scale sys-

tem. The uniformity is confirmed in both horizontal coordinates, with an approximately uniform mean standard deviation achieved at twice the central value in both coordinates.

As expected, the central plane produces the minimum standard deviation across most of its plane. A worsening of the standard deviation is expected as the z coordinate is varied, however, the $z = 20$ mm plane performs approximately 25% worse than the negative z plane. Once again, this performance difference begins in the negative y direction, towards the previously noted poor quality block.

Summary and discussion

System spatial resolution was analysed above, using the standard deviation to inform on the system precision in reproducing measured locations. As the modular camera has been designed for use in a hybrid camera, aiming to combine its high efficiency and large FOV with the high spatial resolution of the Polaris system, the primary goal was to achieve a uniform, sub-millimetre spatial resolution in the central HR+ FOV of the camera. Within the central FOV, a minimum standard deviation of 0.279 ± 0.002 mm was achieved for the selected tracking parameters. Variations in the standard deviation as a function of position were minimal, varying by a factor of 2 on average, achieving notable uniformity. These results indicate that locations measured through the modular camera may be used to supplement those of the Polaris system precisely within the central FOV as desired.

As a secondary goal, a larger detection FOV than that of the Polaris system was desired. Experimental regions of interest requiring micro-scale precision were still intended to remain within the Polaris and HR+ FOVs, but the larger, lower resolution extremities of the modular camera FOV were desired to enable the study of larger systems on the small scale. Beyond the central HR+ FOV of the modular camera, there is a substantial increase in the standard deviation. However, even at the edges of the modular camera FOV, the maximum standard deviation is only four times the central value. With careful selection of tracking parameters, it is feasible to maintain a sub-millimetre standard deviation, although reducing the precision to 1-2 mm is more likely to produce useful location rates. The results in this region indicate that the modular camera may be used to increase the achievable FOV of the hybrid camera beyond the limiting FOV of the Polaris system, enabling the study of larger experimental systems at the moderate cost of spatial resolution, while maintaining the high spatial resolution central region.

5.3.5 System accuracy

While system precision is of utmost importance to micro-scale analysis, system accuracy plays a crucial role in the quality of tracking that can be performed. Incorrectly reconstructed positions will lead to large uncertainties, or even errors, in all following trajectory analyses, increasing in complexity as derivatives are taken to produce higher order measurands. However, with a well-understood and sufficiently precise system, positional correction maps may be produced, ranging from simple linear shifts and rotations of coordinate axes to more complex procedures such as dewarping.

To determine these corrections, knowledge of the system accuracy is required. To quantify the accuracy, three-dimensional position residuals were determined throughout the system FOV.

At each point on the $5 \times 7 \times 5$ grid within the modular camera FOV, an expected position, given by the positioning of the Anet with corresponding spatial resolution, and a measured position, determined through PEPT tracking with a corresponding uncertainty, is known. These positions are shown as a two-dimensional projection overlaid on the contour plot of Figure 5.14 as black and red points for the expected and measured positions respectively. To reduce the inaccuracy contribution of the Anet's placement relative to the modular camera, the coordinate systems of both the Anet and the modular camera were redefined such that the central expected and measured positions were both the overlapping zero position, $\vec{x} = (0, 0, 0)$ mm.

At each position within the grid, the magnitude of the expected distance to the origin position was calculated, with both positions given by the Anet coordinate system. Similarly, the magnitude of the measured distance to the origin position was calculated, with both positions measured through PEPT using the modular camera coordinate system. By subtracting the expected distance from the measured distance, the position residual was determined, with positive values indicating that the measured position was further away from the origin than expected and negative values indicating the opposite.

These position residuals are plotted in Figure 5.14 for the full system FOV. This section will again focus on the structure of the horizontal planes outside the HR+ FOV, with a discussion on the higher resolution FOV in the following subsection.

In these planes, large residuals are visible in the negative x direction. From the previously mentioned issues arising in the top and bottom left of the contour plots, visible in the plotted positions, this loss of accuracy is expected.

Towards $y = 0$ an inward biasing of the positions is visible in both the contour plots and the corresponding profiles, implying that the tracer is typically measured to be closer to the centre of the system than it truly is. As the y coordinate is varied away from zero, this inward biasing changes to an outwards biasing. This is a common artefact of small PEPT systems, requiring correction through a dewarping method, discussed in Section 6.2.3. In particular, these effects are amplified for the planes outside of the HR+ FOV, requiring correction to be viable for use in experiment.

High resolution region

Looking now at the higher resolution region within the HR+ FOV in Figure 5.15, it can be seen that with improved tracking parameters the system accuracy is significantly improved in comparison to Figure 5.14, with a mean positional residual in the x direction of less than 0.5 mm.

In the y direction, the same inward warping effect can be easily seen in both the contour plot and the corresponding y-axis profiles. These profiles are fairly consistent between horizontal planes, indicating an artefact of the system to be corrected (see Section 6.2.3) as opposed to an issue in system construction.

One peculiarity, seen in the negative x direction, is the difference between the ± 20 mm horizontal planes and the central plane. As on the opposing positive x side, it would be expected that these residuals decrease as they move away from zero, but the opposite is seen. In this case, a plausible explanation is the rotation of the Anet coordinate axes in the positioning of the tracer particle. While the initial placement accuracy of the Anet is accounted for by adjusting the zero position, rotation of the printer coordinate

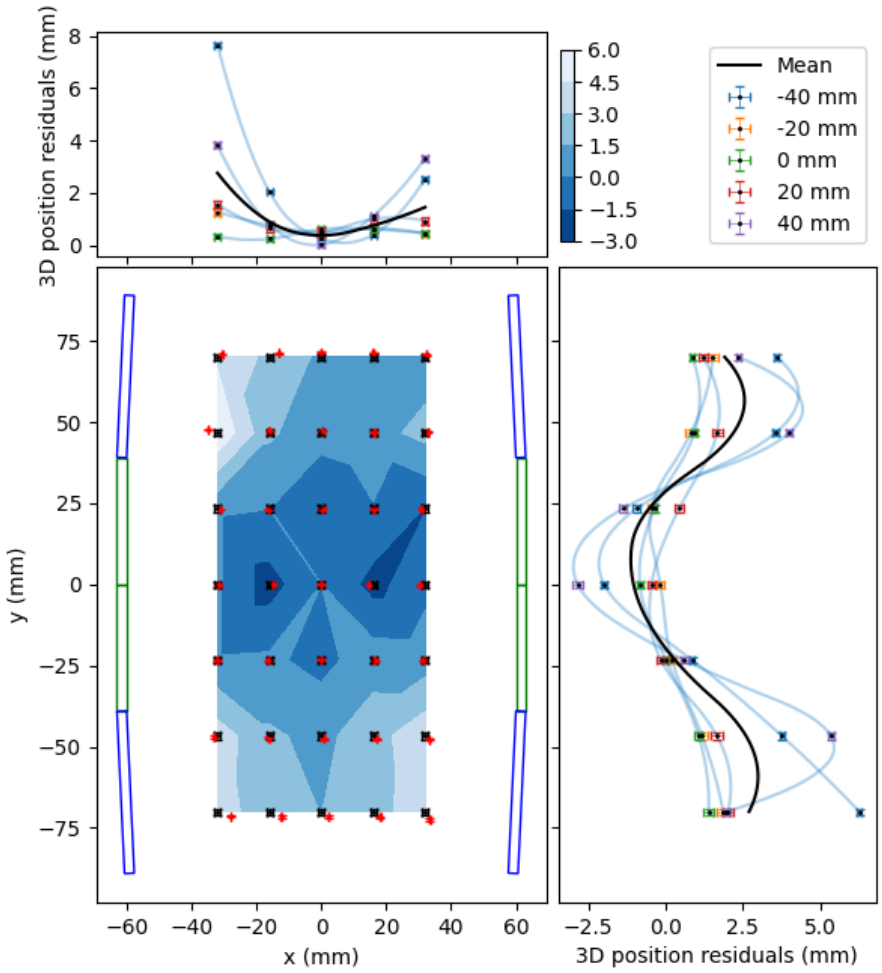

Figure 5.14: The 3D positional residuals plotted as a function of position as described in Section 5.3.1. Each residual is determined through comparison of each expected and measured location with the central position. The expected (black) and measured (red) positions of the central plane are shown as error bars on the contour plot.

system with respect to the camera coordinate system has not been taken into account. The possible rotation angles are small, but positioning uncertainties are large enough to cause such a difference. To produce more accurate correction maps, this possible rotation would need to be accounted for, either through analysis of predefined motions within the system or perhaps with a more robust, fixed positioning system.

Relative accuracy

While an understanding of system accuracy as defined above is useful in characterisation, knowledge of absolute positioning relative to a physical coordinate system is typically difficult to achieve in PEPT measurement, especially when considering the uncertainties involved in the positioning of both the detector system and the tracer particle as discussed above in Section 5.1. Instead, the use of relative positioning is conventional, tracking

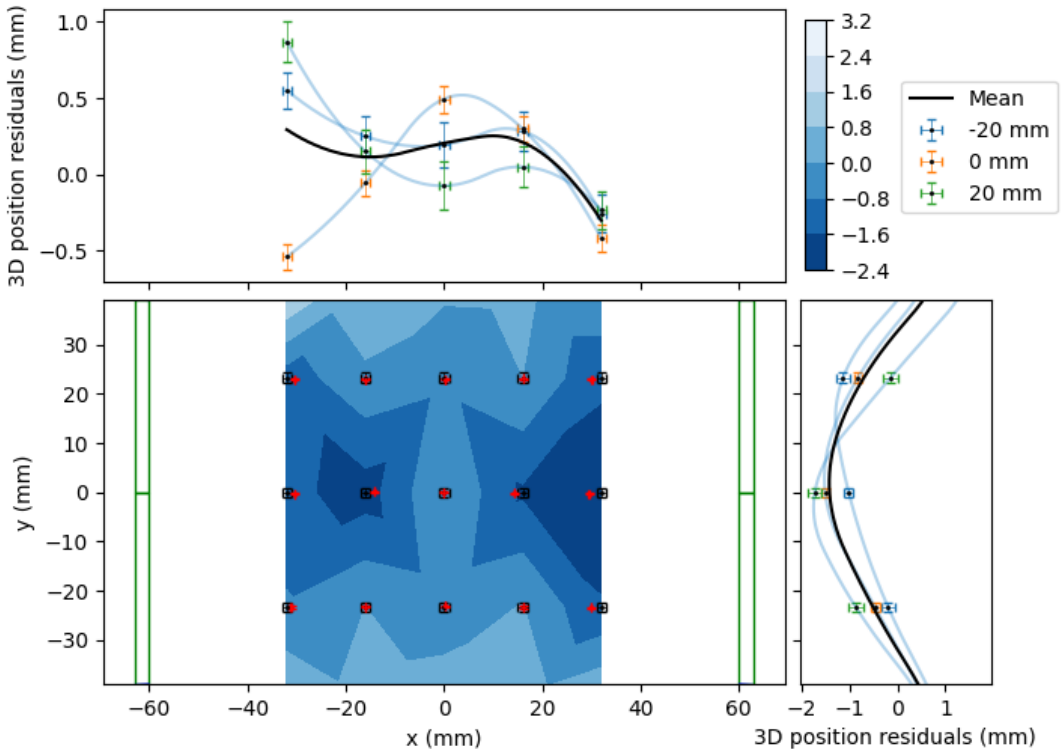

Figure 5.15: The 3D positional residuals plotted as a function of position as described in Section 5.3.1 for the high resolution HR+ FOV. Each residual is determined through comparison of each expected and measured location with the central position. The expected (black) and measured (red) positions of the central plane are shown as error bars on the contour plot.

changes in position to high precision. As such, relative accuracy may be used to quantify system performance in relative positioning.

Three-dimensional position residuals were calculated between each measurement position and its neighbouring positions, as opposed to a central origin, with the mean residual defined as the relative accuracy. Within the high-resolution HR+ FOV, a mean relative accuracy of 0.8 ± 0.1 mm was achieved, dropping to 2.5 ± 0.2 mm towards the extremities of the system FOV. In addition, the relative accuracy profiles were approximately uniform and continuous in each horizontal plane of measurement.

To estimate the total uncertainty of each measured position, contributions from both the system precision and accuracy are required. However, system precision, given as the standard error on each measured position, is suppressed by the relative accuracy contribution, implying that the total uncertainty may be approximated by the relative accuracy.

These results indicate that tracking can be performed reliably within quoted uncertainties in each localised region of the FOV, and there are no large discontinuities between each region.

5.3.6 Comments on characterisation behaviour

The first notable feature of the modular scintillator system characterised above is the large value of f_{opt} at an optimal central value of 85%, implying that a significant majority of measured LORs are used in position reconstruction. An improvement in comparison to the HR+ system 70% is achieved due to an increased geometric efficiency, a lack of scattering material minimising scattered coincidences and a low activity tracer particle producing minimal random coincidences. If higher activity tracer particles are used in experiment to study systems with increased scattering or attenuating material, it is expected that the optimal f value will decrease, and as such this f-optimisation procedure must be repeated in situ for a given experimental system.

When considering the contribution of each coordinate to the spatial resolution, the same optimal value of f was found in each axis. However, the magnitude of the corresponding spatial resolution varied, with the axis between the detector faces found to have the lowest precision by a factor of $> 90\%$ in comparison to each other coordinate. This discrepancy was expected for the modular camera geometry, and further motivated the inclusion and proposed positioning of the Polaris system in a hybrid camera to ensure optimal spatial resolution within the central FOV.

Due to the non-uniformity of the system FOV, the value of f_{opt} also depends on tracer height, rapidly dropping to approximately 55% as the tracer particle leaves the high-resolution HR+ block FOV. This drop is not unexpected, as fewer detector elements contribute to coincidence measurement outside of this FOV, but it indicates the need for careful treatment of the experimental FOV. For small systems that can remain within the high-resolution region, the optimal value of 85% may be used. For larger experimental systems the lower 55% value should be used, compromising on achievable spatial resolution, or a different tracking algorithm should be used as discussed in Section 6.2.5. In addition, a lower f_{opt} value will likely be required to study systems with increased scattering or attenuating material, as mentioned above.

Another feature noted in characterisation was the greatly improved central sensitivity in comparison to the Polaris system. With a fairly uniform profile structure, approximately matching that of simulation as desired, a central sensitivity of 34.8 ± 0.6 cps/kBq was achieved, many times greater than the < 1 cps/kBq sensitivity of the Polaris system. As a result, an order of magnitude improvement to the location rate was achieved with a similarly active calibration source without a large reduction in spatial resolution. Being a function of tracking parameters, the central spatial resolution was determined to follow a $\sigma = 1.5\sqrt{L'}$ relationship for generalised location rate per unit activity, L', producing a maximum rate of approximately 0.45 Hz/kBq for sub-millimetre location uncertainty. With the used 20.11 ± 0.26 kBq tracer the maximum location rate was approximately 11 Hz, but with, for example, the 50 µm 600 kBq tracer described in Section 1.2.2 the maximum location rate could reach approximately 270 Hz.

When assessing the spatial resolution and accuracy of the system, the desired uniformity was successfully achieved in the high-resolution central region. However, moving outside of this region in any coordinate direction resulted in a noticeable decline in system performance, as expected from the considerations of f_{opt} mentioned above. Therefore, careful selection of the experimental region of interest is required in the application of the system, preferably remaining within the high-resolution region to avoid notable variations

in system performance. For larger systems requiring the full modular camera FOV, the performance variations must be managed precisely to ensure precise measurement. For instance, correction maps may be produced making use of the system's high precision to address positional inaccuracy. In particular, an inward biasing effect was noted between the detector units, in which measured positions were closer to the origin than expected by a factor of approximately twice the positional uncertainty. This biasing was expected and is discussed in Section 6.2.3, proposing corrections to enable accurate measurement.

Finally, a noted difference in system performance between the planes measured at positive and negative heights must be corrected in regions in which the performance drop is notable. Alternatively, the underlying issue, suggested to be caused by the poorly calibrated 951 detector blocks, must be solved.

Considering the full characterisation performed here, the developed modular scintillator system demonstrated significantly improved sensitivity, and therefore location rates, in comparison to the Polaris system, without sacrificing achievable spatial resolution and system accuracy. While similarly minimal location uncertainties were not feasible with the scintillator system, these results indicate the feasibility of a hybrid camera combining and leveraging the minimal precision offered by the Polaris system with the demonstrated location rates of the modular scintillator system.

Chapter 6

Conclusions and further work

6.1 Modular camera development

A desire to study phenomena at micro-scale precision led to the development of advanced PEPT instrumentation. Previous work with the UCT Polaris system, a room-temperature semiconductor CZT system, demonstrated the applicability of PEPT on the micro-scale, however, the achievable location rates and system FOV were limited. As such, a modular BGO scintillator array offering a larger FOV with improved absolute efficiency was proposed, designed, constructed and characterised here to supplement the Polaris system.

Design and simulation

At UCT, a selection of BGO scintillator detector blocks, taken from Siemens HR+ and ECAT 951 PET systems, were available for use in a modular scintillator system. A novel data acquisition system was previously developed, interfacing with the 951 electronics to enable modular PEPT systems. However, the supply of 951 detector blocks was limited, with a surplus of HR+ blocks available for use. Therefore, to make use of all available resources, a combined HR+/951 BGO system was investigated. As a possible benefit to this combined system, the differences in spatial resolution and absolute efficiency between the HR+ and 951 blocks offered a trade-off that could be optimised, potentially producing improved results.

The compatibility of the HR+ blocks was tested with the 951 electronics. Few difficulties were expected as the block connections and outputs were very similar to the 951 blocks, differing only in the supply of high voltage. A trial system of four HR+ and four 951 detector blocks was used for testing and sub-millimeter location uncertainty was achieved, indicating viability.

As no specific application was being designed, a general proof-of-concept geometry was desired for the scintillator array. To identify an optimal geometry, a Monte Carlo simulation of the system sensitivity profile was used, with the goal of achieving a uniform central sensitivity to avoid deadtime limiting hotspots and to allow uniformity of PEPT measurements throughout the system FOV. Several options were considered and simulated, and a final symmetric system of two units of four HR+ and four 951 detector

blocks was decided on, offering a system FOV of approximately $120 \times 174 \times 102$ mm^3 with the HR+ blocks placed centrally.

Construction

Each of the four photomultiplier tubes of each of the 16 detector blocks was separately calibrated for position uniformity, ensuring a uniform response across the block to an approximately uniform radiation field. This was achieved by placing a low activity Na-22 source approximately 6 cm from each block face, followed by the use of the built-in calibration routine which adjusted each PMT gain accordingly to achieve similar count rates in each detector crystal. Certain blocks were more easily calibrated than others, with some requiring significant manual gain adjustments to achieve reasonable results and two 951 blocks remaining unsuccessful. Calibration was also performed in terms of individual crystal energy and timing responses, again making use of the built-in calibration routine.

To ensure each detector block was aligned correctly, two 3D-printed bases were produced, one for each unit, taking the HR+ and 951 dimensions into account. Each unit was then placed into the correct configuration and clamped, ensuring minimal movement of each block, reducing the positioning uncertainty.

To enable later characterisation of the system, a 3D printer, the Anet A8, was modified to replace the typical printing element with a custom 3D printed source holder, designed to hold the available calibration sources and move them within horizontal planes. To support the Anet a wooden base was constructed, lifting the system above the scintillator array.

Characterisation

With the system fully constructed, characterisation was performed of each element involved in detection, including the sources used, the detector blocks and the system itself.

For accurate measurements of system sensitivity, a well-known Na-22 source activity was required. At UCT, a set of calibration sources were available, having initial activities of approximately 1 µCi in October 2020. Through theoretical calculation, the activity of the Na-22 source was estimated to be 17.8 ± 3.6 kBq on 24 July 2023. Through singles and coincidence measurements, and subsequent analysis, the activity was measured to be 20.11 ± 0.26 kBq, agreeing with the calculated value at the necessary higher precision.

Since PEPT relies on the 511 keV emissions from positron annihilation, an understanding of the detector energy resolution was required to select optimal lower and upper level energy discriminators, filtering out detections arising from background radiation, scatters, or secondary gamma emissions. Using a selection of calibration sources, standard gamma spectroscopy techniques were performed with a 951 detector block to determine the energy resolution to be $30.51 \pm 0.48\%$ at 511 keV. Similar analysis with the HR+ detector blocks produced results in agreement. From this, optimal lower and upper level discriminators were determined to be 338.9 ± 3.3 keV and 678.4 ± 3.3 keV respectively.

In addition to the energy window, an understanding of the system coincidence timing resolution was required to accurately identify events that were detected from the same positron annihilation. Through the measurements of the time differences between detection events, with and without a variable time delay added to one side of the detection

system, possible optimal coincidence windows of $2\tau = 8$, 16 and 24 ns were identified, containing the majority of true coincidence events. For comparison, these coincidence windows were used in the PEPT reconstruction of a stationary tracer, with the 16 ns coincidence window found to offer a greatly improved location rate with only a slight reduction in spatial resolution. For all further analysis, this coincidence window was used in tracking.

In the Birmingham method, used for tracking in PEPT, parameters of f and N needed to be optimised for the system such that the minimal 3-dimensional standard deviation of each measured position could be achieved. Through the measurement of a stationary Na-22 tracer in the centre of the system FOV, these parameters were varied and within the high-resolution central HR+ FOV of the system the optimal f value was found to be approximately 85% for most values of N. As the tracer was moved outside of the HR+ FOV, into the lower spatial resolution regions of the system, the optimal f value dropped to approximately 55%. The contribution of each coordinate to the 3-dimensional standard deviation was investigated, identifying tracking precision to be the lowest for the axis between the detector faces, as expected from similar parallel plate PEPT system geometries. This further motivated the proposed perpendicular positioning of the Polaris system in the hybrid camera, ensuring optimal spatial resolution within the central FOV. The relationship between N, the 3-dimensional standard deviation and the location rate was investigated, demonstrating both the standard deviation and location rate to decrease with increasing N. The relationship between the standard deviation and the generalised location rate per unit activity, L', in the central position was calculated as $\sigma = 1.5\sqrt{L'}$, identifying a trade-off that can be optimised in future applications. For exclusive characterisation within the HR+ FOV, an N value of 1000 was used, while for analysis of the full system FOV an N value of 500 was used to maintain sufficient location rates.

To perform further characterisation of the system, the Anet was used to position the Na-22 calibration source in an equally spaced $5 \times 7 \times 5$ grid, covering a FOV of $64 \times 140 \times 80$ mm^3 with the measurement FOV limited by the extent of the source holder. Acquisition was performed at each position for five minutes, with three repeat measurements at each position performed non-consecutively. These measurements were analysed in terms of the measured singles rate, sensitivity, spatial precision and accuracy throughout the system FOV.

To determine the singles rate, every event in each detector element was summed at each position, with the measured source-less background rate of 166.93 ± 0.22 Hz subtracted from the total. As expected, the maximal singles rate was achieved in each unit at the centre of its face, decreasing as the source moved radially outwards. The contribution of the opposing unit summed to produce a fairly uniform profile throughout the measurement FOV, decreasing by a maximum of 40% towards the outer edges.

The sensitivity of the system was determined by dividing the true coincidence rate by the measured source activity. To determine the true coincidence rate, the random coincidence rate, being less than 1 Hz, was subtracted from the measured prompt coincidence rate. Through this calculation, the maximum sensitivity of the central position was determined to be 34.8 ± 0.6 cps/kBq, with the measured sensitivity profile qualitatively agreeing with that of the simulation. As expected, the central planes offered significantly

higher sensitivity in comparison to the planes outside of the HR+ FOV, with an approximately uniform mean sensitivity along one horizontal coordinate and a peaked mean sensitivity along the other.

In the case of the characterisation relying on the PEPT algorithm, analysis was separated into the higher resolution central region and the lower resolution region towards the edges of the measured FOV.

In the high-resolution region, the spatial resolution of the central position, as given by the 3D standard deviation of measured positions for a stationary source, was determined to be 0.279 ± 0.002 mm for the selected values of f and N. The corresponding profiles were approximately uniform throughout the region, maintaining a mean value of approximately twice that of the central position. The system absolute accuracy, given by the magnitude of the 3D difference between the expected and measured positions in relation to the central position, maintained an approximately uniform sub-millimetre profile in one horizontal coordinate. However, the other coordinate, defined between the detector units, indicated a warping effect to be discussed in Section 6.2.3. In all cases, the high precision of the system implies that a correction map can be calculated in future work to correct for system inaccuracy.

In the lower resolution regions, primarily determined by those planes outside of the HR+ FOV, notable drops in system spatial resolution and accuracy were visible, with often unpredictable structure. This drop in performance was expected due to the contribution of much fewer detector elements in these regions, but implied that most experimental regions of interest should remain within the central FOV for best results, aligning well with the desire to include the Polaris system in a hybrid system.

In all of the above characterisations, poor results were noticed in regions close to the unsuccessfully calibrated 951 detector blocks. It was proposed that the calibration issues were the cause of the poor performance, but further analysis of the effects of block alignment and calibration is required to confirm this.

6.2 Future work

6.2.1 Hybrid system

Following the characterisation of the scintillator array in this work and the characterisation of the Polaris system in previous work, an immediate next step would be the combination of the two in a hybrid system. As proposed here, placing the Polaris system centrally within the scintillator array would overlap the high-resolution FOV of the Polaris system with the surrounding large, lower-resolution FOV of the BGO system. Conveniently, both systems could fit within the PEPT Cape Town ADAC Vertex camera, adding an additional larger, lower-resolution FOV following the development of the initial hybrid camera.

In the hybrid camera, the coordinate dependence of the system spatial resolution and the noted warping effects may be partially accounted for through the perpendicular alignment of the Polaris system, as shown in Figure 4.5. In addition, this configuration aims to limit scattering within the system, as forward angle scattering is favoured at 511 keV [47]. However, the inclusion of the Polaris system will nevertheless lead to

the increased detection of scattered coincidences, requiring a reduced value of f in the Birmingham method when using the scintillator array.

With each measurement, the tracked positions may be independently analysed, with results such as velocity and acceleration from each system compared and combined. Alternatively, the tracked positions may be combined before analysis, producing a trajectory with infrequent high-precision locations, as measured by Polaris, interpolated with lower-precision, more frequent locations from the scintillator array.

To enable this analysis, some measures may be put in place to ensure the timing of each measurement is closely aligned, such as beginning acquisition with the same code on the same computer. However, a degree of post-processing will be required to accurately align the timing of the two systems, introducing additional uncertainty in trajectory analysis. In addition, characterisation and co-registration of the measurement axes of each system will be required, such that measured trajectories and corresponding results may be accurately compared as functions of position.

To develop the combined system towards true hybrid operation, a novel timing circuit will be required to link events such that coincidence measurements can be made between the semiconductor and scintillator elements. Despite not adding additional detector elements, an increased number of possible coincident pairs will improve the sensitivity of the system, likely leading to improved performance. However, with a perpendicular alignment of the Polaris system, coincident pairs between semiconductor and scintillator elements are unlikely to offer improvements as the primary addressed FOV lies between the Polaris units. In this case, a parallel alignment of the Polaris units may improve sensitivity and performance within the central FOV at the cost of increased scatter.

6.2.2 Deadtime characterisation

In all previous analyses and characterisation of the scintillator system, a low activity Na-22 calibration source was used, with activity of 20.11 ± 0.26 kBq. However, as described in earlier chapters, the spatial resolution of a PEPT system relies in part on the true coincidence rate achievable with the system. While modifications to tracer characteristics and activity were not investigated here, one initial step in future work would be to characterise the scintillator array in terms of its deadtime parameters, such that an optimal activity tracer particle may be used in future analysis for optimal system performance.

To perform deadtime characterisation, a high-activity, short-lived tracer particle should be placed in the system and be allowed to decay over several half-lives. Through data acquisition over this time, prompt singles and coincidence events may be measured, and from these the true and random coincidence contributions may be determined. Through the plotting and fitting of these curves as functions of source activity, deadtime parameters and an optimal source activity for coincidence detection may be determined.

Investigations into the deadtime behaviour of the Polaris system were performed in previous work [1]. The Polaris modules exhibited primarily non-paralysable deadtime behaviour, with a measured deadtime parameter of 24.177 ± 0.096 µs. The system reached a maximum true coincidence rate of 600 Hz with an optimal source activity of 0.8 - 1.5 MBq, having a corresponding singles event rate of approximately 15-20 kHz per module. At

a maximum, the singles event rate per module was deadtime limited at approximately 25 kHz.

In comparison, each module of the BGO scintillator array is limited by a maximum singles rate of approximately 1.5 - 2 MHz with an estimated deadtime of 0.5 - 1 µs per event. Therefore, the optimal activity tracer particle for the BGO system is expected to be much greater than that of the Polaris system, although the increasing random coincidence contribution to the system spatial resolution would require investigation.

For the Polaris system, an increase in tracer activity above the calculated optimal value led to decreased performance, with an increase in random but not true coincidences. However, the performance gain of the scintillator system may offset this, implying a trade-off between the two systems. This would need to be investigated further, through analysis of the spatial resolution of each system, and the combined hybrid results, as a function of source activity and position within the system FOV.

6.2.3 Warping corrections

With measurement of the system spatial resolution and accuracy throughout its FOV, correction maps may be produced to account for reconstruction inaccuracy at each position. Correcting for every position throughout the system FOV may be a difficult process requiring precise positioning apparatus, with a complex uncertainty budget. However, due to the limited number of detector crystals in the scintillator array, limiting possible coincident pairs, the FOV will be undersampled in various regions leading to seemingly random variations in system accuracy. In combination with the spatial warping noted in Section 5.3.5, these effects necessitate the use of a precise correction map.

As a first step towards improving the system accuracy, the noted warping effects may be partially or fully corrected. Due to the depth of interaction effects involved with gamma-ray detection, a biasing towards the centre of the system FOV is expected in PEPT reconstruction [48]. With the scintillator array, this effect was most prominent close to the centre of the detector faces, with an inward biasing of up to approximately twice the system positional uncertainty measured for the positions furthest from the centre of the FOV.

In typical PEPT ring systems, their radial geometries may be leveraged to simplify the correction process, as the warping effects depend primarily on the radial position of the tracer particle. In these cases, simple cubic functions of the radial position of the tracer particle have been used to successfully correct for the inward biasing [49].

In the case of smaller, non-uniform geometries, as in this work, more complex correction maps may be required, for example, fitting to the six coordinates describing the 3D radial distance of the tracer particle from the centre of each detector unit face. However, in the high-resolution FOV of this system, it appears that the warping effect primarily depends on the x coordinate of the tracer, describing the distance between each detector unit face, and a simple polynomial fit applied to this coordinate may be sufficient for most applications. The data measured in this work, in particular the measurements of Section 5.3.5, may be used to build a correction map prior to use of the system.

6.2.4 Positioning uncertainty

In the construction of the system, many sources of positioning and alignment uncertainty contributed to the overall spatial resolution and accuracy of the system. However, many of these sources can be easily addressed, and future work should take steps to reduce these sources of uncertainty before experimental applications.

In the case of the detector blocks, these could be screwed directly into a solid frame, as in the UCT modular system, instead of relying on clamping and 3D-printed frames for support. At present, limited movement of each block relative to the unit itself, and more significant movement of each unit relative to the opposite, is possible, indicating potentially large sources of uncertainty in position measurements. A fixed unit would markedly reduce these uncertainties and lead to reproducible system construction. In addition, some detector block casings had noticeable deformities, slightly affecting their alignment when stacked. Smoothing of these casings would improve block placement.

The Anet positioning stage also contributed positioning uncertainty to each measurement in the location of the tracer particle. The Anet was positioned loosely on top of a wooden frame, which itself was placed on a table, and was highly susceptible to movement. To account for this, calibration was performed before each run in terms of the positioning and alignment of its axes in relation to the scintillator array, but alignment uncertainty was large. By fixing the Anet to its frame, and its frame to the experimental surface, many of the calibration requirements would be eliminated, improving the positioning accuracy of the system.

Finally, much of the positioning of the detector units and the Anet was achieved using graphing paper attached to the experimental surface. While sufficient for these purposes, the paper was not perfectly flat and parallax error played a significant role in the calibration of the Anet. By attaching the system to a solid surface designed for accurate positioning, such as an optical bench, much of this uncertainty could be reduced.

As all of the above factors contributed to the quoted uncertainty budget, any improvements made in future work will increase system precision. For deeper analysis, the effects of relative detector block positioning can be studied, investigating the relationship between the offset of a block from its expected position and system precision and accuracy. Analysis of this type has been performed with modular systems previously [50], and it may demonstrate the extent to which detector block positioning affects the achievable performance of the system, as well as confirm whether the system description is accurate.

6.2.5 Improved tracking and filtering

Due to the non-uniformity of the system geometry and its relatively low number of detector elements in comparison to typical PEPT systems, the achievable performance varied significantly throughout the measurement FOV. In addition, large variations in system sensitivity throughout its FOV led to the optimal tracking parameters and achievable location rates varying considerably as functions of position. A possible remedy for these issues may be the use of alternative PEPT algorithms [21]. Each algorithm offers advantages and disadvantages in comparison to the Birmingham method used here, but certain algorithms may be better equipped to handle system non-uniformity, and may also improve on system precision with low coincidence rates.

Of particular interest within UCT is the machine learning (PEPT-ML) tracking algorithm. Recent investigation into its capabilities has demonstrated improved performance over the Birmingham method in particular circumstances, such as in the tracking of turbulent flow paths [51]. Another potential alternative algorithm is the spatiotemporal B-spline reconstruction (SBSR) method, designed for tracking low-activity tracer particles with few LORs through the minimisation of an objective function. Having been used for the tracking of single cells *in vivo* [52], this method may lend itself well to the potential applications of micro-scale PEPT.

Beyond alternative tracking algorithms, enhanced filtering and data processing methods may be employed to improve upon the analysis of measured trajectories. One such method, previously applied to the Polaris system in initial testing, is the Savitzky-Golay filter [53], making use of interpolation and local polynomial least squares fitting to simultaneously compute higher order measurands, such as velocity and acceleration, and improve upon the PEPT uncertainty budget, enabling higher precision measurement.

Bibliography

[1] N. Hyslop. Sub-millimetre positron-emission particle tracking using a CdZnTe semiconductor array. Master's thesis, University of Cape Town, 2021.

[2] T.W. Leadbeater, D. J. Parker, and J. Gargiuli. Positron imaging systems for studying particulate, granular and multiphase flows. *Particuology*, 10:146–153, 2012.

[3] K.E. Waters, N.A. Rowson, X. Fan, D.J. Parker, and J.J. Cilliers. Positron emission particle tracking as a method to map the movement of particles in the pulp and froth phases. *Minerals Engineering*, 21:877–882, 2008.

[4] J.J. Cilliers and K. Cole, 2013. UK Intellectual Property Office Patent 1319600.1.

[5] T.W. Martin, J.P.K. Seville, and D.J. Parker. A general method for quantifying dispersion in multiscale systems using trajectory analysis. *Chemical Engineering Science*, 62:3419–3428, 2007.

[6] J.R. Jones and J. Bridgwater. A case study of particle mixing in a ploughshare mixer using Positron Emission Particle Tracking. *International Journal of Mineral Processing*, 53(1):29–38, 1998. doi: https://doi.org/10.1016/S0301-7516(97)00054-9.

[7] L.S. Bbosa, I. Govender, A.N. Mainza, and M.S. Powell. Power draw estimations in experimental tumbling mills using PEPT. *Minerals Engineering*, 24(3):319–324, 2011. doi: https://doi.org/10.1016/j.mineng.2010.10.005.

[8] W.R. Ketterhagen, M.T. am Ende, and B.C. Hancock. Process modeling in the Pharmaceutical Industry using the Discrete Element Method. *Journal of Pharmaceutical Sciences*, 98(2):442–470, 2009. doi: https://doi.org/10.1002/jps.21466.

[9] K. Cole, D.J. Barker, P.R. Brito-Parada, A. Buffler, K. Hadler, I. Mackay, D. Mesa, A.J. Morrison, S. Neethling, A. Norori-McCormac, B. Shean, and J. Cilliers. Standard method for performing positron emission particle tracking (PEPT) measurements of froth flotation at PEPT Cape Town. *MethodsX*, 9:101680, 2022. doi: https://doi.org/10.1016/j.mex.2022.101680.

[10] M.R. Hawkesworth, D.J. Parker, P. Fowles, J.F. Crilly, N.L. Jefferies, and G. Jonkers. Nonmedical applications of a positron camera. *Nuclear Instruments and Methods in Physics Research Section A: Accelerators, Spectrometers, Detectors and Associated Equipment*, 310(1):423–434, 1991.

[11] D.J. Parker, C. Broadbent, P. Fowles, M. Hawkesworth, and P. McNeil. Positron emission particle tracking - a technique for studying flow within engineering equipment. *Nuclear Instruments and Methods in Physics Research Section A: Accelerators, Spectrometers, Detectors and Associated Equipment*, 326(3):592–607, 1993.

[12] D.J. Parker et al. Developments in particle tracking using the Birmingham Positron Camera. *Nuclear Instruments and Methods in Physics Research Section A: Accelerators, Spectrometers, Detectors and Associated Equipment*, A392:421–426, 1997.

[13] Y.S. Fangary. A Lagrangian study of solids suspension in a stirred tank vessel by Positron Emission Particle Tracking (PEPT). *Chemical Engineering and Technology*, 25:521–528, 2002.

[14] R.D. Wildman et al. Single-particle motion in three-dimensional vibrofluidized granular beds. *Physical Review E*, 62:3826–3835, 2000.

[15] A. Sadrmomtaz, D.J. Parker, and L.G. Byars. Modification of a medical PET scanner for PEPT studies. *Nuclear Instruments and Methods in Physics Research Section A: Accelerators, Spectrometers, Detectors and Associated Equipment*, 573(1):91–94, 2007. Proceedings of the 7th International Conference on Position-Sensitive Detectors.

[16] A. Buffler, I. Govender, J. Cilliers, D. Parker, J-P. Franzidis, A. Mainza, R. Newman, M. Powell, and A. Van der Westhuizen. PEPT Cape Town: A new positron emission particle tracking facility at iThemba LABS. *Int. Topical Meeting on Nuclear Research Applications and Utilization of Accelerators*, 2009.

[17] N. Hyslop. Sub-millimetre positron-emission particle tracking using a CdZnTe semiconductor array. Master's thesis, University of Cape Town, 2021. Figures 3.3, 3.6 and 4.1 reproduced or adapted from [1].

[18] A. McKnight, T. Leadbeater, and R. van der Merwe. Characterisation of a new LSO block detector for Positron Emission Particle Tracking. In *Proc. of SAIP2022, the 66th Annual Conf. of the South African Institute of Physics (July 1-8 Gqeberha)*, pages 224–229, 2022.

[19] R. Pérez-Mohedano, N. Letzelter, C. Amador, C.T. VanderRoest, and S. Bakalis. Positron Emission Particle Tracking (PEPT) for the analysis of water motion in a domestic dishwasher. *Chemical Engineering Journal*, 259:724–736, 2015. doi: https://doi.org/10.1016/j.cej.2014.08.033.

[20] C.Y. Wu, X.F. Fan, F. Motazedian, J.P.K. Seville, D.J. Parker, and A.C.F. Cocks. An experimental study of die filling using positron emission particle tracking. *Proceedings of the Euro Powder Metallurgy Congress and Exhibition, Euro PM 2007*, 3: 335 – 340, 2007.

[21] CRK. Windows-Yule et al. Recent advances in positron emission particle tracking: a comparative review. *Reports on Progress in Physics*, 85(1), 2022.

[22] D. Ritchie, L. Mileshkin, and D .Wall et al. In vivo tracking of macrophage activated killer cells to sites of metastatic ovarian carcinoma. *Cancer Immunology, Immunotherapy*, 56:155–163, 2007.

[23] X. Song, H.G. Wood, and D. Olsen. Computational Fluid Dynamics (CFD) study of the 4th generation prototype of a continuous flow Ventricular Assist Device (VAD). *Journal of Biomechanical Engineering*, 126(2):180–187, 2004.

[24] H. Tashima, T. Yamaya, E. Yoshida, S. Kinouchi, M. Watanabe, and E. Tanaka. A single-ring OpenPET enabling PET imaging during radiotherapy. *Physics in Medicine and Biology*, 57(14):4705, 2012. doi: 10.1088/0031-9155/57/14/4705.

[25] S.A. Nehmeh and Y.E. Erdi. Respiratory Motion in Positron Emission Tomography/Computed Tomography: A Review. *Seminars in Nuclear Medicine*, 38(3):167–176, 2008. doi: https://doi.org/10.1053/j.semnuclmed.2008.01.002. Developments in Instrumentation.

[26] A. Kaushik, A. Jaimini, M. Tripathi, M. D'Souza, R. Sharma, A. Mondal, A.K. Mishra, and B.S. Dwarakanath. Estimation of radiation dose to patients from (18) FDG whole body PET/CT investigations using dynamic PET scan protocol. *The Indian Journal of Medical Research*, 142(6):721–731, 2015.

[27] Y. He, Y. Gu, and H. Yu et al. Optimizing acquisition times for total-body positron emission tomography/computed tomography with half-dose 18F-fluorodeoxyglucose in oncology patients. *EJNMMI Physics*, 9(45), 2022.

[28] B. Hsu. PET tracers and techniques for measuring myocardial blood flow in patients with coronary artery disease. *Journal of Biomedical Research*, 27(6):452–459, 2013.

[29] D.J. Parker, R.N. Forster, P. Fowles, and P.S Takhar. Positron emission particle tracking using the new Birmingham positron camera. *Nuclear Instruments and Methods in Physics Research Section A: Accelerators, Spectrometers, Detectors and Associated Equipment*, 477(1):540–545, 2002. doi: https://doi.org/10.1016/S0168-9002(01)01919-2. 5th Int. Conf. on Position-Sensitive Detectors.

[30] D. Parker, T. Leadbeater, X. Fan, M. Hausard, A. Ingram, and Z. Yang. Positron imaging techniques for process engineering: Recent developments at Birmingham. *Measurement Science and Technology*, 19:094004, 07 2008.

[31] CRK. Windows-Yule et al. Recent advances in positron emission particle tracking: a comparative review. *Reports on progress in physics*, 85(1):12, 2022. Figure 11 reproduced from [21].

[32] A. Buffler, K. Cole, T.W. Leadbeater, and M.R. van Heerden. Positron emission particle tracking: A powerful technique for flow studies. *International Journal of Modern Physics: Conference Series*, 48:1860113, 2018.

[33] *National Nuclear Data Center*. NuDat database. URL `https://www.nndc.bnl.gov/nudat/`.

[34] J.H Kim, J.S Lee, J.S Kim, J-K. Chung, M.C Lee, and D.S Lee. Physical performance comparison of Ga-68 and F-18 in small animal PET system. *Journal of Nuclear Medicine*, 51(supplement 2):1423–1423, 2010.

[35] A. Camroodien, M. van Heerden, S. Nair, and T. Leadbeater. Development of 18F radiochemistry for Positron Emission Particle Tracking (PEPT). In *Proc. of SAIP2021, the 65th Annual Conf. of the South African Institute of Physics (July 22-30 Gqeberha)*, 2022.

[36] T. Leadbeater, M. van Heerden, A. Buffler, A. Camroodien, and G Steyn. Targetry for the in-beam activation of tracer particles for positron emission particle tracking. *EPJ Web of Conferences*, 285, 06 2023. doi: 10.1051/epjconf/202328509004.

[37] K.E. Cole, A. Buffler, N.P. van der Meulen, J.J. Cilliers, J-P. Franzidis, I. Govender, C. Liu, and M.R. van Heerden. Positron emission particle tracking measurements with 50 micron tracers. *Chemical Engineering Science*, 75:235–242, 2012.

[38] R. Raylman, B. Hammer, and N. Christensen. Combined MRI-PET scanner: a Monte Carlo evaluation of the improvements in PET resolution due to the effects of a static homogeneous magnetic field. *IEEE Transactions on Nuclear Science*, 43(4): 2406–2412, 1996.

[39] P. Colombino, B. Fiscella, and L. Trossi. Study of positronium in water and ice from 22 to -144 C by annihilation quanta measurements. *Il Nuovo Cimento (1955-1965)*, 38:707–723, 1965.

[40] T. Leadbeater, D.J. Parker, and J Gargiuli. Characterization of the latest Birmingham modular positron camera. *Measurement Science and Technology*, 22, 2011.

[41] G.F. Knoll. *Radiation Detection and Measurement*, pages 12–13, 113–116, 310, 354–368, 668–673. John Wiley, third edition, 2009.

[42] D.J. Parker and T.W. Leadbeater. New life in old PETs – the work of the University of Birmingham Positron Imaging Centre. In *6th World Congress on Industrial Process Tomography. WCIPT6, 06-09 Sep 2010, Beijing, China. International Society for Industrial Process Tomography*, 2010.

[43] H. Yang, F. Zhang, Y. Zhu, and Z. He. Efficiency measurement on 6.0 cm3 3-D CdZnTe detectors. *IEEE Nuclear Science Symposium conference record. Nuclear Science Symposium*, 10 2010. doi: 10.1109/NSSMIC.2010.5874513.

[44] T Leadbeater. *The Development of Positron Imaging Systems for Applications in Industrial Process Tomography*. PhD thesis, The University of Birmingham, 2009. Figure 3.3 reproduced from [50].

[45] Spectrum Techniques. Type D and type M gamma radiation disc sources. `https://www.drct.com/dss/sources/gammasources.htm` [Accessed: 9 August 2023].

[46] D.M. Hampel, S. Manger, D.J. Parker, and Tz. Kokalova Wheldon. SuperPEPT: A new tool for positron emission particle tracking; first results. *Nuclear Instruments and Methods in Physics Research Section A: Accelerators, Spectrometers, Detectors and Associated Equipment*, A1028:166254, 2022.

[47] O. Klein and Y. Nishina. Über die streuung von strahlung durch freie elektronen nach der neuen relativistischen quantendynamik von dirac. *Zeitschrift für Physik*, 52:853–868, 11 1929. doi: 10.1007/BF01366453.

[48] W. Moses. Fundamental limits of spatial resolution in PET. *Nuclear Instruments and Methods in Physics Research Section A: Accelerators, Spectrometers, Detectors and Associated Equipment*, A648:S236–S240, 2011.

[49] C. Wiggins, N. Patel, Z. Bingham, and A. Ruggles. Qualification of multiple-particle positron emission particle tracking (M-PEPT) technique for measurements in turbulent wall-bounded flow. *Chemical Engineering Science*, 204:246–256, 2019.

[50] T. Leadbeater. *The Development of Positron Imaging Systems for Applications in Industrial Process Tomography*. PhD thesis, The University of Birmingham, 2009.

[51] R. Perin, K. Cole, M.R. van Heerden, A. Buffler, Y-Y. Lin, J. Zhang, P.R. Brito-Parada, J. Shock, and S.W. Peterson. On the ability of Positron Emission Particle Tracking (PEPT) to track turbulent flow paths with Monte Carlo simulations in GATE. *Applied Sciences*, 13(11), 2023.

[52] K.O. Jung, T.J. Kim, Yu J.H., S. Rhee, W. Zhao, B. Ha, K. Red-Horse, S.S. Gambhir, and G. Pratx. Whole-body tracking of single cells via positron emission tomography. *Nature Biomedical Engineering*, 4:835–844, 2020.

[53] R. van der Merwe and T. Leadbeater. Enhancing PEPT: high fidelity analysis with augmented detection. In *Proc. of SAIP2021, the 65th Annual Conf. of the South African Institute of Physics (July 22-30 Gqeberha)*, 2022.

Appendix A

Related publications

A.1 SAIP 2022, van der Merwe

Conference proceedings produced as the primary author following an oral presentation at the 66th Annual Conference of the South African Institute of Physics (SAIP 2022), published December 2022.

Citation:
R. van der Merwe et al., MicroPEPT: A step toward hybrid PEPT detectors, in The Proceedings of SAIP2022, the 66th Annual Conference of the South African Institute of Physics, edited by Prof. Aletta Prinsloo, (UJ), pp. 588 - 593. ISBN: 978-0-6397-4426-1. Available online at http://events.saip.org.za

MicroPEPT: A step towards hybrid PEPT detectors

R van der Merwe*, S Peterson, A Buffler, M van Heerden, A McKnight and T Leadbeater

Department of Physics, University of Cape Town, South Africa

E-mail: * VMRROB003@myuct.ac.za

Abstract. Positron Emission Particle Tracking (PEPT) measures the trajectory of a freely moving radioactive tracer particle, and enables the non-invasive study of dynamic systems from engineering to medicine. PEPT performance is limited by the activity achievable in radiolabelling a suitable tracer particle, and the fixed geometry of conventional detector systems. In investigating phenomena on micro-scales, recent development of advanced instrumentation has been required to offset these limitations. A modular bismuth germanate oxide (BGO) scintillator array, with detection modules derived from CTI/Siemens PET scanners, has been constructed and coupled to a recently developed data acquisition system. This array consists of 1024 detector elements (512 pixels of 6.75 x 6.25 x 30 mm and 512 pixels of 4.1 x 4.0 x 30 mm) giving a field of view of 150 mm x 196 mm x 101 mm. Energy and timing resolutions of this system were determined and sensitivity profiles were modelled numerically, informing on optimal system parameters to enable future characterisation of the detector efficiency, spatial resolution and deadtime parameters. These initial results indicate the applicability of modular BGO scintillator arrays in addressing small scale flow phenomena, and lead the direction of future work in combining the BGO system with a pair of high resolution pixelated semiconductor detectors for the first time.

1. Introduction

The Positron Emission Particle Tracking (PEPT) technique can be used to non-invasively study dynamic systems, with applications in fields from engineering to medicine [1, 2, 3]. By radiolabeling a suitable tracer particle, tracking can be performed to high spatial and temporal resolution over an extended time, from which the trajectory of the tracer can be determined with an associated uncertainty. Recently, a need to examine more challenging systems on the micro-scale has arisen with PEPT applications in the study of micro-scale flows, such as the flows in biological systems and microfluidic devices, as well as potential applications in beam line tracking in proton radiotherapy [4]. However, PEPT performance of existing systems is limited by the absolute efficiencies of fixed geometries, compounded by low activity in radiolabeling suitable small tracer particles, leading to the requirement of advanced instrumentation development. Previous work with semiconductor detectors has demonstrated the feasibility of applying PEPT to micro-scale systems [4], but the achievable field-of-view (FOV) and location rates were limiting, promoting the benefits of development towards a hybrid detection system accounting for these limitations. In this paper, the development and characterization of a modular scintillator array designed to support a semiconductor detection system is performed, serving as a first step towards the development of hybrid detection systems optimised for micro-scale particle tracking.

2. The PEPT technique and spatial resolution

The PEPT technique makes use of proton rich radioisotopes to label a suitable tracer particle for the system of interest. Emitted positrons annihilate with free electrons to produce two approximately back-to-back 511 keV photons due to momentum conservation [5]. When these photons are detected in coincidence, a 3-dimensional line-of-response (LOR) is defined along which the annihilation event occurred. Through the measurement of many such LORs, the position of the tracer can be determined with an associated uncertainty.

However, not all recorded LORs arise from true coincidence events. Random coincidences can occur when a photon originating from another unassociated source is detected within the coincidence window forming one or both parts of a coincident pair. Similarly, scattered LORs occur when one or both coincident photons scattered in surrounding materials before being detected. To account for these issues, an iterative least-squares minimisation algorithm [1] is used to remove corrupt LORs, finding the most likely location of the tracer at a given time.

The spatial resolution of a PEPT system operating as described can be estimated with $u(\bar{P}) = \frac{w}{\sqrt{T}}$ where $u(\bar{P})$ is the 3-dimensional location uncertainty on a measured PEPT location $\bar{P}$, w is the spatial resolution of the positron camera, and T is the true coincidence rate [6]. For micro-scale tracking, PEPT location uncertainty must be reduced, achieved by either reducing w or increasing T. Considering significant changes to tracer choice and production to be beyond the scope of this work, reducing w can be achieved by reducing the pixel size of the detection system, and improving its energy resolution. Increasing T can be achieved by increasing the data rate, by increasing either the activity of the tracer or by increasing the absolute efficiency of the detection system. Absolute efficiency is determined by the intrinsic efficiencies of the detector materials and the geometric efficiency of the whole system, assuming no deadtime.

Typical PEPT systems have fixed geometries and detector materials implying fixed efficiencies, energy resolution, and pixel sizes. Significant improvements to the spatial resolution of a PEPT system are achieved with the development of a new detection system optimising these properties for micro-scale measurement, with an emphasis on reduced pixel size and increased energy resolution. Typically however, energy resolution and pixel size improvement is accompanied with reduction in absolute efficiency. A modular detection system allowing adjustment of its geometry and therefore absolute efficiency is ideal, and the use of multiple detection systems with different materials and properties as a hybrid camera allows for the highest degree of optimisation.

3. Detector technologies

Noting the significant dependence of the PEPT spatial resolution on pixel size and energy resolution, semiconductor detectors typically offer the best performance. Previous work [4] has investigated the feasibility of the University of Cape Town (UCT) Polaris system [7], consisting of a pair of pixelated room-temperature cadmium zinc telluride (CZT) semiconductor crystals shown in figure 1, with promising results demonstrating sub-millimeter tracking of low activity tracer particles [4]. However, the absolute efficiency and timing resolution of the semiconductor system are both relatively low, negatively impacting the achievable coincidence rates, and hence location frequency. The achievable FOV dimensions of the system were limited by the small detector scale, preventing its use in applications requiring micron precision where system scales are on the order of centimeters. To improve on the FOV scale and location rates, it is natural to turn to larger scintillator detectors, offering improved absolute efficiencies and timing resolutions.

UCT has detector components from a Siemens ECAT 951 and EXACT HR++ PET scanners retired from clinical use, both comprised of detector blocks of bismuth germanate oxide (BGO) segmented into 8x8 scintillator crystals, shown in figure 1. The detector blocks from the HR++ camera are smaller than those from the 951, having pixel dimensions of 4.1 x 4.0 x 30 mm^3 and 6.75 x 6.25 x 30 mm^3 respectively, where the difference implies a trade-off between spatial

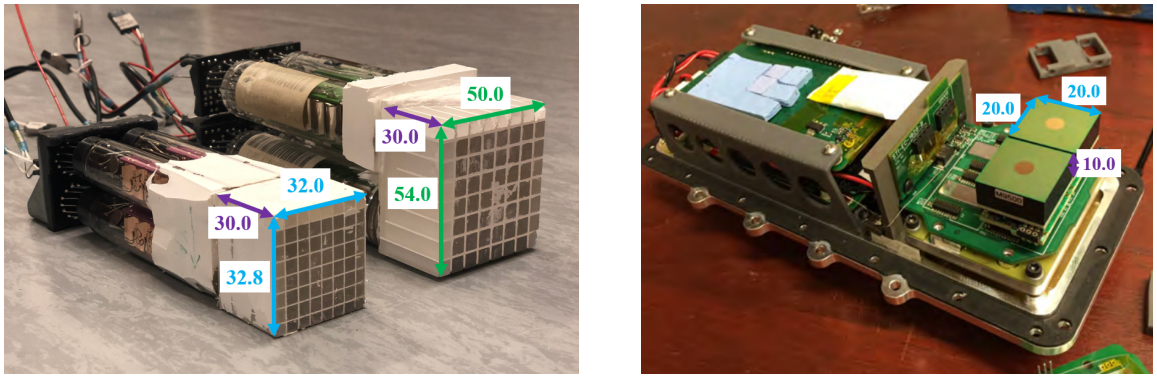

Figure 1. (Left) Detector blocks from the EXACT HR++ (left) and ECAT 951 (right) without protective casing. In each, four photomultiplier tubes and their 8x8 segmented crystals can be seen. (Right) The internals of the PolarisJ module, showing the two CZT crystals as the green squares on the right. All dimensions are given in mm.

resolution and absolute efficiency by virtue of their relative pixel densities and overall sizes.

Both of these detector types offer at minimum an intrinsic detection efficiency of 55% at 511 keV, whereas the Polaris system, with its much smaller pixels of 1.8 x 1.8 x 0.5 mm^3, offers only 15% detection efficiency. Through the development of a modular hybrid system, the trade-offs between all three detector types can be optimised for micro-scale tracking, achieving micro-scale location precision mostly through the use of the semiconductor system while maintaining useful location rates and larger volume FOV through the scintillators.

4. Detector characterisation

4.1. Energy resolution

Important elements of the PEPT detection system are the lower and upper level discriminators (LLD and ULD respectively), determining the allowed range of measured energy values describing a valid annihilation photon. Setting these limits accurately reduces noise by removing scattered events that are corrupt LORs. The energy resolution of the corresponding detector block is determined by measuring the width of the appropriate 511 keV photopeak. The energy resolution of a 951 detector block was determined in this paper, and similar calculations have been performed for both the HR++ blocks [8] and the Polaris system [4].

The four photomultiplier tubes (PMTs) from each detector block were connected to individual NIM pre-amplifiers and amplifiers, with the signal from each summed and digitised, using a multi-channel analyzer to produce pulse height spectra. However, since the detector PMTs do not provide uniform outputs due to manufacturing and component tolerances, a process of gain-matching was performed with photopeaks from each PMT aligned in pulse height by adjusting the gains of the separate amplifiers producing a single photopeak in the summed output.

Using three calibration sources, Na-22 (511 and 1275 keV), Cs-137 (662 keV) and Co-60 (1173 and 1332 keV)[9], an energy calibration was performed by Gaussian fitting to the appropriate photopeaks and relating them to their expected energies. Due to the poor energy resolution of the BGO crystals, the two independent photopeaks of the Co-60 source could not be separately identified as their Gaussian peaks overlapped. To account for this in the calibration, a single Gaussian was fit to the combined peak using a weighted mean centroid.

The fitting parameters of the 511 keV peak of Na-22 were determined from figure 2 and the energy resolution was calculated to be $30.51 \pm 0.48\%$ at 511 keV. Repeating the process for the 1275 keV photopeak, an energy resolution of $28.9 \pm 2.2\%$ was found. Using the computed energy resolution, the optimal lower and upper level discriminators were selected to be the centroid

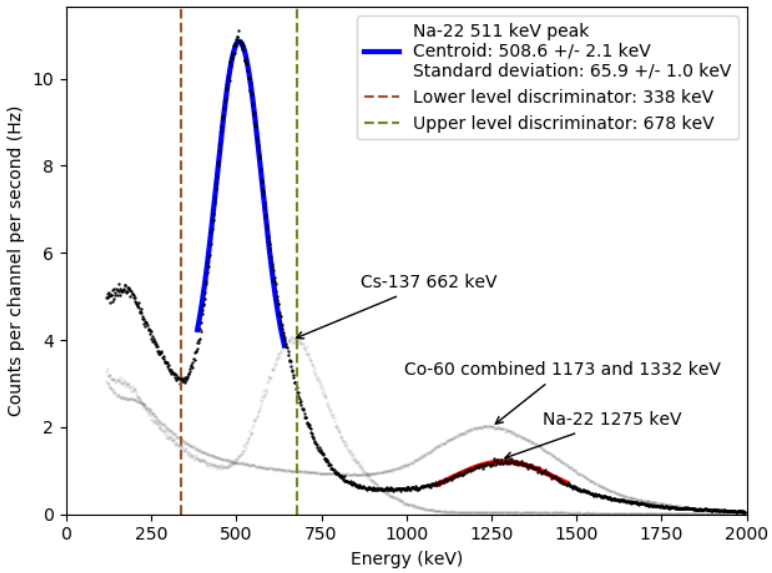

Figure 2. Calibrated energy spectra of the three sources as measured by a 951 detector block. The Na-22 spectrum is shown in bold, with Gaussian peaks fitted to each photopeak. Optimal lower and upper level discriminators are shown as dashed vertical lines.

energy $\mu \pm N\sigma$, where N was chosen to include 99% of the photopeak, giving 338.9 ± 3.3 keV and 678.4 ± 3.3 keV respectively. The LLD agrees with the expected energy of the Compton edge, indicating that this choice of N excludes the Compton scattered photons from the 511 keV peak, reducing the fraction of corrupt LORs.

4.2. Temporal resolution

The temporal resolution describes the precision at which the system can measure the time of arrival for a single detection event. Two single events are regarded as simultaneous, or coincident, if they both occur within a coincidence window of time period 2τ, where τ is limited by the time resolution in resolving an event. When τ is greater than the time resolution of the system, all true coincidences will be recorded, and the number of recorded random coincidences increases linearly with τ. Knowledge of the time resolution allows for the careful selection of 2τ which maximises the true coincidence rate while limiting the random coincidence rate, minimising the inclusion of corrupt LORs from random events.

Singles events were recorded for a positron source central to a pair of detector modules operating in coincidence, and a time delay was added to the events in one module. By varying this delay and determining the number of events that were within the same coincidence window, a Gaussian curve representing the system's coincidence timing resolution was plotted. As the delay is increased from zero, fewer true coincidences are detected and beyond a point all measured coincidences are random coincidences. As the size of the coincidence window is increased beyond the system's intrinsic timing resolution, the Gaussian curves reach a maximum and plateau as all true coincidences are fully covered by the chosen window. Increasing the coincidence window beyond that point leads to the inclusion of a higher fraction of corrupt LORs.

In figure 3, these curves are shown for varying coincidence windows, with the flat top visible at large values of 2τ. Fitting a Gaussian function to each of the curves with coincidence windows of 8 and 24 ns, being the curves with typical Gaussian shapes, the standard deviation of each

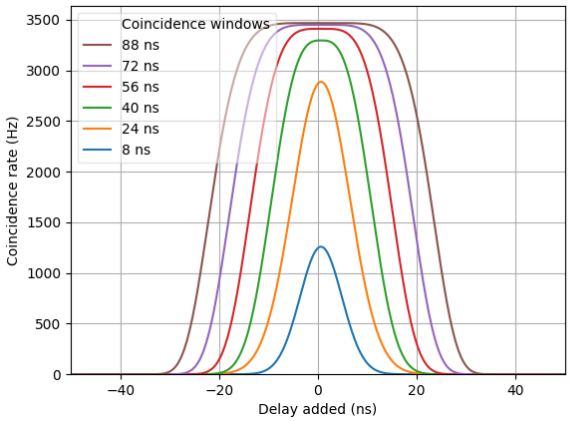

Figure 3. The coincidence rate as a function of time delay added to one of the coincident modules. Each curve represents a different coincidence window, 2τ.

was determined to be 4.24 ± 0.03 ns and 5.78 ± 0.03 ns respectively. The difference arises from the use of different coincidence windows. In the $2\tau = 24$ ns case, τ is greater than the time resolution of the system and the window width is included in the peak, whereas in the 8 ns case τ is less than the system's time resolution, being approximately 4.24 ns.

The temporal resolution of PEPT locations can be estimated using the uncertainty estimator. Assuming $w = 5$ mm for the BGO system, at a 1 MHz acquisition rate a location period of 2.5 ms can be estimated, achieving $u(\bar{P}) = 100$ µm. This location period implies systems under investigation must be slow moving, which is unsurprising as this system has not been optimised for high rate applications, which may be investigated in future work.

4.3. Geometry definition

The hybrid camera geometry needs to be carefully optimised to leverage the benefits of each detector type if it is to be used for micro-scale PEPT. A BGO system consisting of two modules of four 951-series detector blocks and two modules of HR++ detector blocks was developed.

Clearly, the central region of the detector system is the most significant in measurements of micro-scale phenomena and the Polaris system must be placed there. The placement of the BGO modules is more flexible, and their individual characteristics must be considered. To do this, a Monte Carlo simulation of the sensitivity profile of the system was used for further optimisation, where the Monte Carlo aspects handled the volume effects of the crystals and their intrinsic efficiencies. A uniform sensitivity profile is desired in the central region of interest to avoid dead time limiting hot spots and to allow uniformity of PEPT measurements over the volume, but absolute uniformity is difficult to achieve due to the number of detector types.

In figure 4, the geometry of the hybrid camera system is shown, consisting of 1024 BGO pixels and 9680 CZT pixels, giving a high resolution region of interest between the Polaris modules of $(62 \times 42 \times 20)$ mm^3 shown as a shaded red region, and a larger FOV between the BGO modules of $(150 \times 196 \times 101)$ mm^3. This geometry was selected as the HR++ blocks placed between the 951 blocks allow for the improved spatial resolution of the HR++ blocks to contribute significantly to the central region of interest, while also maintaining improved absolute efficiencies and an increased FOV as offered by the 951 blocks.

The uniformity of the sensitivity profile was validated using the simulation in figure 4, where sensitivity profiles as functions of their corresponding coordinates are shown at different depths along the Z axis in grey, with the mean sensitivity over all depths shown in bold. The uniformity of the central region can be seen in these profiles, although notable variation in uniformity can be seen at varying depths. Several other possible geometries were also tested, with none achieving

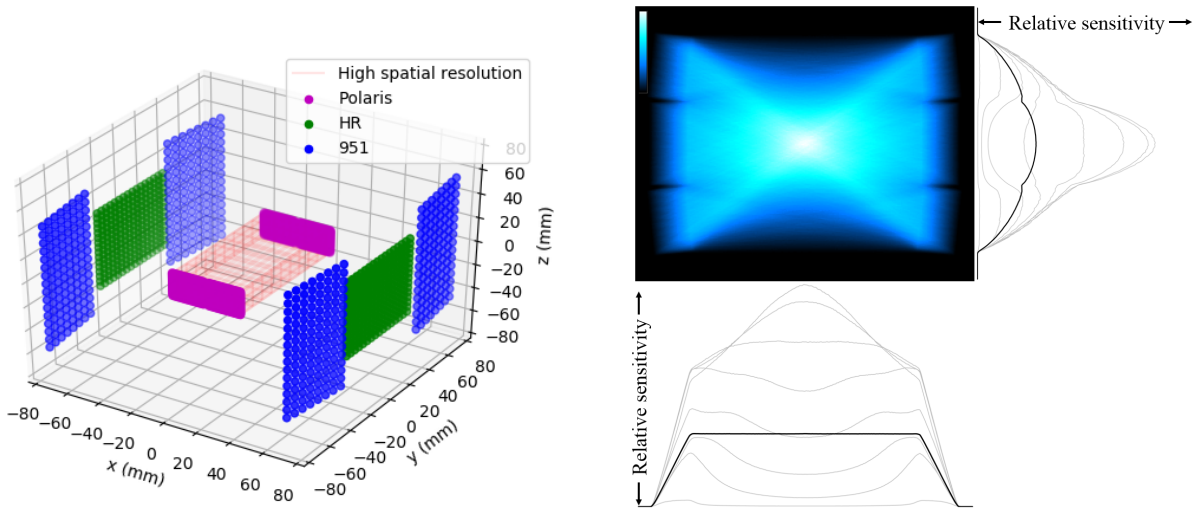

Figure 4. (Left) The geometry of the hybrid camera, showing each segmented detector element as a separate pixel with the central shaded high resolution region. (Right) The simulated sensitivity profile in the XY plane integrated along the Z axis, with corresponding profiles along the Y (side) and X (bottom) axis shown at varying depths. All profiles are drawn to scale.

similar central uniformity as in the chosen geometry. Using known deadtime limits of the BGO modules and their estimated efficiencies, a practical activity range of tracer particles was determined for the system, from 50 kBq to deadtime limiting 15 MBq particles.

5. Conclusions and future work

A modular BGO scintillator array was constructed to enable the application of PEPT to systems on the small scale, at micron precision. A numerical model of the sensitivity profile of the system was used to optimise the chosen geometry for uniformity within its field of view. Energy and timing resolutions were determined, allowing for the optimisation of system parameters for low noise detection. Precise characterisation of the detection efficiency, spatial resolution and deadtime parameters of the system in the future will lead into the development of a hybrid detector system combining the modular BGO array with a pair of high resolution pixelated semiconductor detectors, enabling the application of PEPT in the study of micro-scale phenomena for the first time.

References

[1] Parker D, Broadbent C, Fowles P, Hawkesworth M and McNeil P 1993 *Nuclear Instruments and Methods in Physics Research Section A: Accelerators, Spectrometers, Detectors and Assoc. Equipment* **326** 592 – 607
[2] Buffler A, Govender I, Cilliers J, Parker D, Franzidis J P, Mainza A, Newman R, Powell M and Van der Westhuizen A 2009 *Int. Topical Meeting on Nuclear Research Applications and Utilization of Accelerators*
[3] Leadbeater T, Parker D J and Gargiuli J 2012 *Particuology* **10**(2) 146–153
[4] Hyslop N 2021 *Sub-Millimetre Positron-Emission Particle Tracking Using a CdZnTe Semiconductor Array* Master's thesis
[5] Knoll G F 2009 *Radiation Detection and Measurement* (John Wiley) pp 12–13 3rd ed
[6] Leadbeater T and Parker D 2013 *7th World Congress in Industrial Process Tomography* pp 85–94 ISBN 0853163235
[7] H3D Inc. 2018 *J6400 High-Energy High-Flux Spectrometer* URL `https://h3dgamma.com/J6400Specs.pdf`
[8] McKnight A, Leadbeater T and van der Merwe R 2022 *Characterisation of a new LSO block detector for Positron Emission Particle Tracking* The Proceedings of SAIP2022
[9] NuDat database *National Nuclear Data Center* URL `https://www.nndc.bnl.gov/nudat/`

A.2 SAIP 2022, McKnight

Conference proceedings produced as a co-author following a poster presentation by Alice McKnight at the 66th Annual Conference of the South African Institute of Physics (SAIP 2022), published December 2022.

Citation:
A. McKnight, R. van der Merwe and T. Leadbeater, Characterisation of a new LSO block detector for Positron Emission Particle Tracking, in The Proceedings of SAIP2022, the 66th Annual Conference of the South African Institute of Physics, edited by Prof. Aletta Prinsloo, (UJ), pp. 224 - 229. ISBN: 978-0-6397-4426-1. Available online at http://events.saip.org.za

Characterisation of a new LSO block detector for Positron Emission Particle Tracking

Alice McKnight, R S van der Merwe and T W Leadbeater
Department of Physics, University of Cape Town, South Africa
E-mail: MCKALI012@myuct.ac.za

Abstract. The University of Cape Town Physics Department recently acquired a Siemens Biograph 16 HiRez combined PET/CT scanner manufactured in 2005. Unlike older scanner models utilized by the department in Positron Emission Particle Tracking (PEPT), the Biograph scanner uses modern lutetium oxyorthosilicate (LSO) scintillators with a rapid response time, pixelated into a finer spatial grid. The new scintillating material promises an increased light output and faster decay time resulting in improved spatial resolution and reduced dead time compared to the conventional bismuth germanium oxide (BGO) crystals. Advanced front end data acquisition and processing compliment the new detector physics enabling high (energy, timing, & spatial) resolution measurements with low distortion. The LSO crystal dimensions are 4 x 4 x 20 mm^3 arranged in blocks of 13 x 13 optically coupled to 4 photomultiplier tubes. Groups of 12 blocks are serviced by a detector controller responsible for analogue front end data acquisition and digitisation. The full scanner contains 12 controllers totalling 24336 crystals arranged in rings of 39 axially and 624 transaxially. Detector blocks and controllers have been extracted from the original device and reconfigured with a customised data acquisition system. Characteristics such as detector efficiency, temporal resolution, energy resolution, and spatial resolution have been investigated and are compared to performance of previous models for further use in PEPT and positron imaging applications.

1. Introduction

Positron Emission Particle Tracking (PEPT) is a nuclear radiation imaging-based technique to measure the dynamics of physical processes [1]. The University of Cape Town Physics Department has a dedicated facility for PEPT at iThemba Labs which currently employs a Siemens HR++ PET camera. The department recently acquired a Siemens Biograph 16 HiRez combined PET/CT scanner manufactured in 2005. Unlike older scanner models, such as the HR++, the Biograph uses modern lutetium oxyorthosilicate (LSO) scintillators with a rapid response time, pixelated into a finer spatial grid. This new scanner will ultimately replace the HR++ at iThemba Labs but must first be characterised and studied to understand its performance from a physics perspective. Once this is achieved the scanner can be modified for further PEPT research, such modifications include developing a means of acquiring list-mode data, implementing higher resolution timestamping, and encoding other data streams such as telemetry from pumps and mass flow controllers [2].

The Siemens 2005 Biograph 16 HiRez is a combined Positron Emitting Tomograph (PET) and X-ray Computed Tomography (CT) scanner which uses advanced gamma ray detection technology to image not only the structure of a system (CT), but also its function (such as metabolic

activity in a medical scenario - PET). The PEPT facility at iThemba labs has historically used positron imaging implemented on modified ex-clinical PET systems to study and characterise functional processes, granular systems, and multiphase flow. By replacing the HR++ scanner at the lab with the newer Biograph, future PEPT research will have access to more advanced PET technology with higher spatial, temporal and energy resolutions and the ability to correlate structure (CT) and function (PET/PEPT) for the first time [3].

To characterise the scanner, detector blocks and controllers were extracted from the original device and reconfigured with a customised data acquisition system. Characteristics such as detector efficiency, temporal, energy, and spatial resolution were investigated and compared to performance of existing detector systems used in PEPT and positron imaging applications.

2. Functional Description

The key physical process that PET technology relies on is the electron-positron annihilation. Positrons are emitted by the breakdown of a proton rich radionuclide taking the form of a substance administered to the patient for conventional PET scans, or the tracer particles used in PEPT. Positrons collide with an electron and annihilate near the site of the decay, with the positron range between emission and annihilation contributing a fundamental limit to the spatial resolution in imaging. The annihilation results in two gamma rays, conserving energy and momentum with emission in opposite directions in the reference frame of the electron-positron system. The angle with which the photons are observed in the laboratory frame has slight variability ($\pm$ 0.5°) known as noncollinearity, contributing further spatial resolution limits. The emitted gamma rays are measured by the rings of detectors surrounding the system, enabling the time of arrival (ns), energy (keV), and position (mm) of incidence to be determined and stored as raw data from which an image or PEPT analysis can be reconstructed [4].

Each individual detector block within the scanner utilizes a scintillating material which, when ionized by incoming radiation, produces a high energy electron via the photoelectric effect. Energy deposition by this electron excites the atoms in the material to luminescence. A segmented array of these crystals is connected to 4 photomultiplier tubes which output an electronic pulse proportional to the absorbed scintillation light intensity (and hence energy). The crystal elements are optically separated by a reflecting material, the depth of which is empirically determined to share the scintillation light linearly between the four photomultiplier tubes [5]. Comparison of the relative scintillation light intensities enables the exact crystal element illuminated to be determined. A flood histogram illustrating the crystal array of the new LSO detector can be seen in figure (1a) below. The composite signal from the block detector is passed through a single channel analyser (SCA) to determine energy qualified events valid in the range 425 - 650 keV as set by the upper and lower level discriminators. A fast branch of the composite signal is passed to a constant fraction discriminator (CFD) to determine the time of arrival for the event at ns resolution. Singles event data are transmitted to a central coincidence processing unit, where a timing gate system is used on energy qualified events to determine pairs of events assumed to be from the same annihilation. Events from different detectors are regarded as simultaneous (in coincidence) if they both occur within a fixed time window 2τ, with the rate of random coincidences scaling linearly with the gate duration τ [3]. Simultaneous events are known as coincidence pairs and allow the reconstruction of a line of response drawn between the two detectors. Many pairs allow an image map to be created by localising the position of annihilation corresponding to the activity in the organ of the patient, or the location of the tracer particle allowing for particle tracking.

3. Experimental Method

A single module consisting of twelve detectors and the associated readout electronics was extracted from the scanner and reconfigured in the lab. The detectors require a split rail power supply providing reference ground (0 V), positive 5.0 V, and negative 5.2 V. Once functional, a means of communicating with the module was developed. The electronics board utilises three communication ports. One is for communications between the detector and the main controller board, carrying a master synchronisation clock (62.5 MHz), a strobe used to parse data words (8.00 MHz), and RS232 standard serial communications enabling calibration and event statistics readout. The other two ports carry singles event data from the module in emitter coupled logic (ECL) over twisted pair conductors. Each event is digitised and transmitted as a parallel set of six 8-bit words with each bit presented at the master clock frequency, and end of word parsed by the strobe. A dedicated translating circuit was built to convert from ECL to transistor transitor logic (TTL) and event words were captured using a custom data acquisition system [6]. Each of the six 8-bit words contains the data representation of a single event in the module, including the time of arrival (ns) relative to the master clock, the energy of the event (keV), and position of the event (block in module; row in block; column in block). The energy calibration and position correction table are determined from the data as presented in figure 1 below.

The front-end electronic processing system was used to query the LSO block detectors for event information. These data included pulse height spectra which was subsequently calibrated in terms of photon energy, position calculations per event used to calculate the absolute crystal positions, and CFD timing encoding time of arrival of energy qualified events. In order for comparison, Nuclear Instrumentation Modules (NIM) were used to obtain singles data for the BGO block detector; signals from each PMT were read-out with individual NIM pre-amplifiers and amplifiers and then summed and digitised. The summed signals were digitised using a multichannel analyser and the pulse height spectrum generated for multiple radioactive sources including ^{22}Na (511 keV), ^{137}Cs (662 keV) and ^{60}Co (1173 and 1332 keV).

4. Results

Characteristics of the LSO crystals used in the Biograph are compared directly against those of the BGO crystals used in the HR++ in order to gauge the similarities and differences expected in their behaviour. Table 1 shows that the LSO detectors have a factor of three higher light output and are expected to yield a correspondingly higher energy resolution of order 1.75 ($\sqrt{3}$). The scintillation light decay time is a factor of six improved on BGO with similar factor improvement expected in time resolution and dead-time factors. Despite the higher material density, LSO is expected to have lower intrinsic photopeak efficiency due to the lower effective atomic number and higher proportion of Compton events relative to photoelectric absorption.

Table 1. Crystal properties for both BGO and LSO [7] [4].

Material property	BGO	LSO
Density (g/cc)	7.13	7.40
Effective atomic number	75	66
Decay time (ns)	300	∼47
Linear attenuation at 511 keV (cm^{-1})	0.96	0.88
Ratio between photoelectric and Compton at 511 keV	0.78	0.52
Light output (photons/511 keV)	4200	∼13000

Results using the on-board analysis capability were retrieved from the Biograph detector controllers and are illustrated in figure 1. The figure contains a flood histogram (a, left) produced by uniformly illuminating the entire face of a detector block, in which each of the 13×13 crystals are clearly distinguishable. The histogram illustrates the selectivity in identifying the excited crystal element, from which a correction table can be built. Figure (1b) contains the calibrated pulse height spectrum for the summed PMT signals from an LSO detector block, illustrating the annihilation photopeak at 511 keV and the upper and lower discriminators applied at 425 keV and 650 keV respectively.

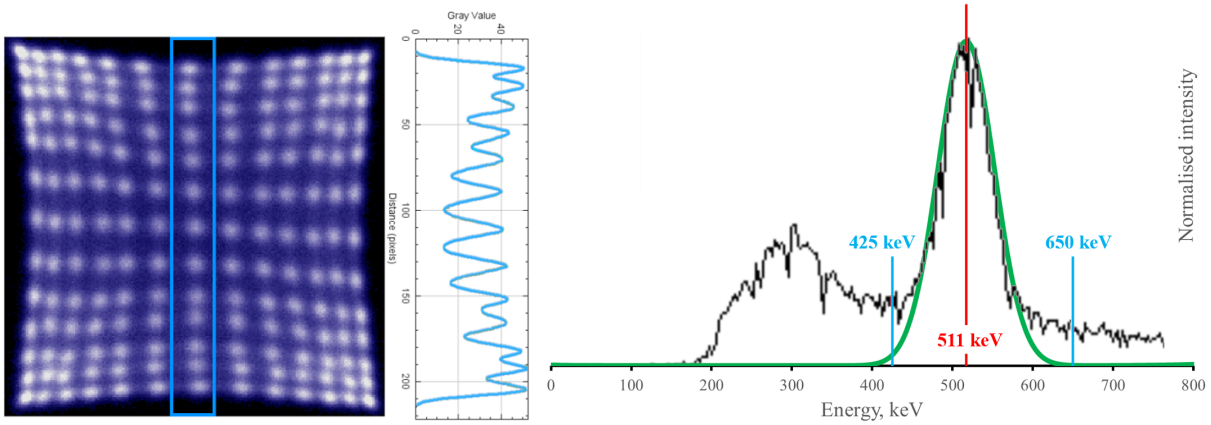

(a) Flood histogram of the 13x13 crystal array in the an LSO detector block.

(b) Calibrated pulse height spectrum of a ^{22}Na source from the summed PMT signals of an LSO detector block.

Figure 1. Results obtained from the on-board analysis of the Biograph system.

Numerical results from analysis of LSO (Biograph) and BGO (HR++) detector blocks are documented in Table 2 below:

Table 2. Results obtained from systematic study of LSO and BGO detector blocks, numerical data from Table 1 where appropriate.

Property (at 511keV)	BGO	LSO
Measured energy resolution (%)	33	17
Calculated energy resolution (%)	30	17
Manufacturer energy resolution (%)	30	16
Calculated intrinsic peak efficiency (%)	41	32
Calculated total interaction efficiency (%)	94	93
Measured intrinsic photopeak efficiency (%)	60	-

The measured 511 keV annihilation photopeaks were characterised by numerically fitting a Gaussian function and parameterising in terms of area, centroid, and standard deviation σ. The energy resolution function was determined as $R = {}^{\Delta E}/_{E}$ and measured as the photopeak FWHM / centroid where the Full Width at Half Maxmium (FWHM) is 2.35 σ. The resolution is reported as a percentage of the full energy at 511 keV.

Photopeak resolutions for BGO and LSO were measured to be 33% and 17% respectively,

in agreement with the expectation calculated using the Poissonian uncertainty relation and a photomultiplier tube quantum efficiency of 25%. The measured and calculated values are in agreement with the manufacturer specifications for these detector materials, which is somewhat supririsingly given the additional complexity of the segmented block detector design.

The measured intrinsic photopeak efficiency for the BGO detector was determined through comparing annihilation photopeak areas over a range of source-detector separation distances allowing normalisation by the projected solid angle. The intrinsic photopeak efficiency was measured to be slightly higher than expected, however these data may include some contribution from Compton scattering over the energy window chosen to define the peak as well as down-scattering from an associated high energy photon. The intrinsic peak efficiencies are in broad agreement within the range expected numerically.

The efficiency of the detector is influenced by the scintillating material density and linear attenuation coefficient, and a high ratio between the photoelectric and Compton interactions. Photoelectric interactions are favoured as they result in the total absorption of the incoming photon energy, while Compton interactions may only absorb a fraction of the energy and the resultant scattered photon might lead to further interactions in the adjacent detectors, making it difficult to locate the primary interaction. The photoelectric microscopic cross-section scales with the effective atomic number to the power of four, while the Compton scattering cross-section being only linearly proportional to it; a material with a higher effective atomic number therefore yields an improved ratio and higher efficiency. The total macroscopic cross-section scales linearly with material density, thus higher density materials are preferred [7].

The integration of the composite light signal is a direct measure of the energy deposited by the annihilation photons, and is dominated by Poisson statistics in the scintillation light intensity. Higher light output scintillators therefore improve the energy resolution of the detector, as evidenced by the improved energy resolution of the LSO scintillator compared to the lower light output BGO devices.

A smaller decay time allows for higher precision in measuring the time of arrival of the incoming radiation, and reduced front end detector deadtime implying overall higher event rates. Advantageously, the faster decay time of the LSO scintillator allows a reduced coincidence window (2τ = 4ns) compared to the BGO system (2τ = 12 ns) thereby reducing the relative fraction of random coincidences in the recorded data stream. High speed timing potentially enables measurement of the time-of-flight for the photon pairs.

5. Conclusion

Properties of the recently acquired Siemens Biograph 16 HiRez combined PET/CT scanner were determined through a systematic investigation of the characteristics possessed by the LSO crystals utilised within the scanner detectors. These properties include the detector energy, spatial, and timing resolution, and efficiency. The results were compared directly against characteristics of BGO crystals used by models preceding the Biograph, such as the HR++ and demonstrated an improved energy resolution in the LSO crystals at 17% compared to 30% in BGO, with a decreased intrinsic photopeak efficiency at 32% compared to 41% in BGO. These results agree with theoretical expectations deduced from physical properties of the crystals as described in Table 1 and 2. Numerical results of the measured characteristics, together with estimated values for other properties such as intrinsic resolution and efficiency are in broad agreement.

References

[1] Parker, D., Broadbent, C., Fowles, P., Hawkesworth, M. and McNeil, P. 1993 Positron emission particle tracking - a technique for studying flow within engineering equipment. *Nuclear Instruments and Methods in Physics Research Section A: Accelerators, Spectrometers, Detectors and Associated Equipment.* **326** 592-607

[2] Buffler, A. & Cole, K. & Leadbeater, T. & van Heerden, M. 2018 Positron emission particle tracking: A powerful technique for flow studies *International Journal of Modern Phys.: Conf. Series 48* 1860113

[3] van der Merwe, R & Peterson, S & Buffler, A & van Heerden, M & McKnight, A & Leadbeater, T. 2022 MicroPEPT: A step towards hybrid PEPT detectors *The Proceedings of SAIP22*

[4] Bailey, D. L., Townsend, D. W., Valk, P. E., Maisey, M. N., 2005 *Positron Emission Tomography, Basic Sciences* 13-39

[5] Casey, M., Nutt, R., 1986 A Multicrystal Two Dimensional BGO Detector System for Positron Emission Tomography *IEEE Transactions on Nuclear Science* **33** 460-463

[6] Leadbeater, T. *et al.* 2012 Positron imaging systems for studying particulate, granular and multiphase flows. *Particuology* **10** 146-153.

[7] Phelps, M. 2004 *PET: Physics, Instrumentation, and Scanners* New York, (Springer), 14-19

A.3 INPC 2022, van der Merwe

Conference proceedings produced as the primary author following an oral presentation at the 28th International Nuclear Physics Conference (INPC 2022), published September 2023.

Citation:
R van der Merwe et al 2023 J. Phys.: Conf. Ser. 2586 012123

Micro-scale particle tracking using hybrid detectors

R van der Merwe*, S Peterson, A Buffler, M van Heerden, N Hyslop, T Hutton, and T Leadbeater

Department of Physics, University of Cape Town (UCT), South Africa

E-mail: * VMRROB003@myuct.ac.za

Abstract. Positron Emission Particle Tracking (PEPT) techniques allow the tracking of a radioactive tracer particle moving within a system of flow, enabling non-invasive study of dynamic systems. On the micro-scale, PEPT performance is limited by the achievable activity in radiolabelling a suitable tracer particle, and the fixed geometry of conventional detector systems. To enable application of PEPT towards these scales advanced instrumentation is required, and a hybrid detection system has been developed combining scintillator and semiconductor devices. A bismuth germanate oxide (BGO) scintillator array consisting of 1024 detector elements derived from CTI/Siemens PET scanners (512 pixels of 6.75 x 6.25 x 30 mm^3 and 512 pixels of 4.1 x 4.0 x 30 mm^3) forms a field of view of 150 x 196 x 101 mm^3. A pair of pixelated cadmium zinc telluride room temperature semiconductors (9680 pixels of 1.8 x 1.8 x 0.5 mm^3) form a high spatial resolution region of 62 x 42 x 20 mm^3 placed within the larger field of view. The design choice maximizes absolute efficiency by merit of the scintillators and enhances spatial resolution through the semiconductors. Energy and timing resolutions of the BGO elements were determined, and sensitivity profiles of the system modelled numerically, enabling the characterization of the system absolute efficiency and spatial resolution. The results suggest the applicability of PEPT in the study of microscale flows for the first time, including investigating flows in capillaries and micro-fluidic devices.

1. Introduction

Positron emission tomography (PET) imaging is a powerful non-invasive technique in which fluid tracer distributions can be imaged over time in biological systems, with use cases in medicine to characterise disease, alongside research into the systems and techniques used [1]. Based on PET, positron emission particle tracking (PEPT) [2] was developed to study dynamic systems, with applications in the fields of engineering to medicine [2, 3, 4]. By labeling a single tracer particle with a positron emitting radionuclide, tracking can be performed within a system to high spatial and temporal resolution, from which the tracer trajectory can be accurately reconstructed with an associated uncertainty. A desire to study micro-scale phenomena in PEPT, e.g. flows, has lead to the development of advanced instrumentation to account for performance limitations of existing systems. The fixed geometries of existing PEPT detection systems limit absolute efficiencies, and micro-scale tracer particles are necessarily limited in their activities given the difficulty in fabrication. As a result, the conventionally achievable location rates are inadequate to study dynamic (fast moving, cm/s) particles. Previous work [5] with semiconductor detectors has demonstrated the applicability of PEPT on the micro-scale, however the achievable location rates and field-of-view (FOV) were limited. In this work, a modular scintillator array offering improved absolute efficiencies has been constructed to supplement the semiconductor array.

Characterisation of the system has been performed, extending previous work [6] and leading towards the development of a hybrid PEPT system for the study of micro-scale phenomena.

2. The Positron Emission Particle Tracking (PEPT) technique

PEPT relies on positron annihilation, where positron emission from a tracer particle is followed by annihilation, producing two approximately back-to-back 511 keV photons. When these photons are detected in time coincidence, a line-of-response (LOR) can be defined, ideally describing the 3D line along which the annihilation occurred. However, not all LORs arise from true coincidence events, and corrupt LORs are reconstructed where one or both photons were detected originating from an unassociated decay, or after scattering. An iterative least-squares minimisation algorithm [2] isolates true coincidences and determines the instantaneous position of the tracer particle over time with an associated uncertainty, using many LORs per location. The spatial resolution of a PEPT system can be described by $u(\bar{P}) = w/\sqrt{T}$ where $u(\bar{P})$ is the 3D location uncertainty on a measured PEPT location $\bar{P}$, w is the spatial resolution of the positron camera, and T is the true coincidence rate [7]. To improve upon the spatial resolution as required for micro-scale PEPT, a detector pixel size reduction or energy resolution improvement can reduce w, whereas an increase in system absolute efficiency or tracer activity can increase T, noting activity is limited in practice. Existing PEPT systems make use of scintillator devices, leveraging their favourable efficiency and time resolution to perform high-speed tracking, with spatial resolution suitable for typical applications. Semiconductor detectors offer smaller pixel sizes and improved energy resolution, although have relatively poor detection efficiency and time resolution. The Polaris system [8] at UCT, consisting of pixelated cadmium zinc telluride (CZT) semiconductor crystals, has been investigated for PEPT, achieving sub-millimetre tracking of a low activity tracer particle [5]. However, event rates and the FOV were limited, leading to the development of a hybrid system combining semiconductor and scintillator devices. Characterisation of a modular scintillator array optimised to support Polaris is reported here, where high quality characterisation allows for dynamic position and timing corrections per crystal, yielding high precision tracking.

3. Detector Geometry

A modular scintillator array has been constructed from detector blocks of segmented 8 x 8 bismuth germanate oxide (BGO) scintillator crystals from Siemens ECAT 951 and EXACT HR+ PET scanners. Both block types have the same pixel count and similar intrinsic efficiency, with differing dimensions. The HR+ detector block has smaller pixels (4.0 x 4.1 x 30 mm^3) than the 951 detector block (6.25 x 6.75 x 30 mm^3), leading to improved spatial resolution, whereas the overall size increase of the 951 detector block improves its geometric efficiency. A hybrid system combining these blocks can therefore optimise their relative advantages for micro-scale tracking. A high spatial resolution central region is achieved by placing the HR+ blocks and the Polaris system centrally, while the achievable system FOV and absolute efficiency is improved by placing the 951 blocks surrounding the central region. One module of the BGO array is shown in figure 1, with the HR+ blocks placed in a central square surrounded by 951 blocks. The full hybrid geometry consists of two such modules opposing to provide a FOV of 150 x 196 x 101 mm^3, with the Polaris system placed perpendicularly between the two to provide a central high spatial resolution region of 62 x 42 x 20 mm^3. A numerical model of the sensitivity profile of the system was used to determine the optimal geometry for the BGO elements of the system, aiming for a centrally uniform sensitivity profile to avoid deadtime limiting hotspots and to allow uniformity of PEPT measurements over the volume. Several detector configurations were tested, and an optimal geometry consisting of four HR+ and four 951 detector blocks per module was found, having the best central uniformity with results shown in figure 1.

A set of 3D printed frames were produced to align the BGO detector modules. A significant

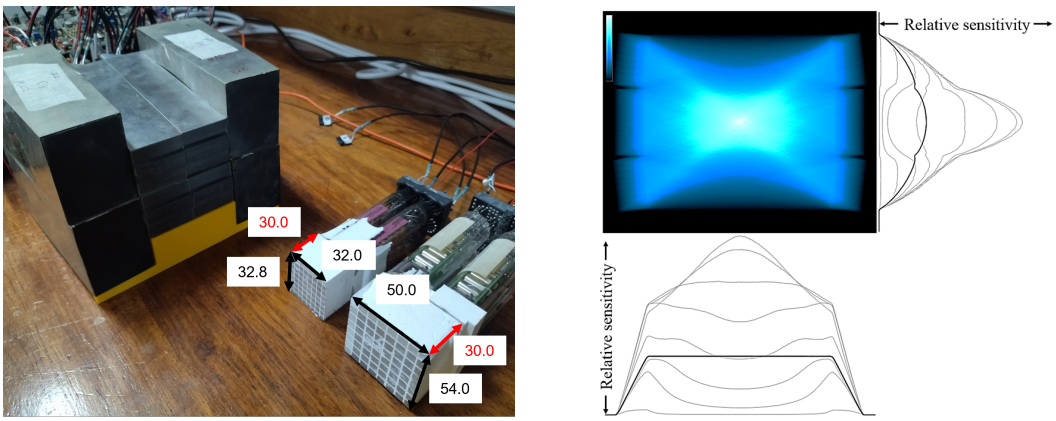

Figure 1. (Left) The geometry of a single optimal BGO detector module placed on its 3D printed frame, with HR+ (left) and 951 (right) detector blocks shown without their protective casing alongside. Dimensions are given in mm. (Right) A plan view of the simulated sensitivity profile integrated along the vertical axis. Corresponding profiles are shown alongside at varying depths, with the uniform mean highlighted in bold. Profiles are drawn to scale.

contribution to the location uncertainty budget is the precision in the relative placement of the individual detector elements, and these frames allow for precise and reproducible block placement. The spatial resolution of the 3D printer, being approximately 0.4 mm and 0.15 mm in the horizontal and vertical directions, is taken into account in LOR reconstruction.

4. Energy and temporal resolutions

To achieve micro-scale spatial resolution, low-noise detection is required. Two parameters ensuring limited noise are the energy and timing coincidence windows, and by optimising these windows the fraction of corrupt LORs can be reduced. The energy window, defined by the lower and upper level discriminators (LLD and ULD), dictates whether a detected photon is discarded based on deposited energy, selecting photons which are likely to have arisen from annihilation. To accurately set the discriminators to minimise the detection of scattered or random photons, an understanding of the detector energy resolution is required. For a single 951 detector block, anodes from the four photomultiplier tubes were connected to preamplifier and amplifier systems, with signals summed and then digitised to produce a pulse height spectrum. An energy calibration was performed using standard gamma photon-emitting calibration sources, and a Gaussian function was fitted to the annihilation photopeak from Na-22. The energy resolution was determined to be $30.51 \pm 0.48\%$ at 511 keV. Choosing the energy window such that 99% of the annihilation photopeak was encompassed, the LLD was set as 338.9 ± 3.3 keV and the ULD as 678.4 ± 3.3 keV. This choice of discriminators excludes most scattered photons, reducing corrupt LORs, with the LLD approximately aligning with the expected 340 keV Compton edge.

When two photons with appropriate energies are detected (i.e. singles events) within a time period of 2τ, with τ limited by the system time resolution, they are considered coincident. The random coincidence rate scales linearly with τ, thus optimisation of this window is required, using the time resolution of the system to select τ to maximise the true coincidence rate while limiting corrupt LORs. To determine the time resolution of the 951 blocks, singles events were recorded in two coincident modules, and a systematic time delay was added to one of the modules. As the delay is varied from zero to ± 256 ns, the number of true coincidences decrease until only random coincidences remain, generating a Gaussian curve when τ is lower than the time resolution of the system. As τ increases, the Gaussian curves plateau as all true coincidences lie within the

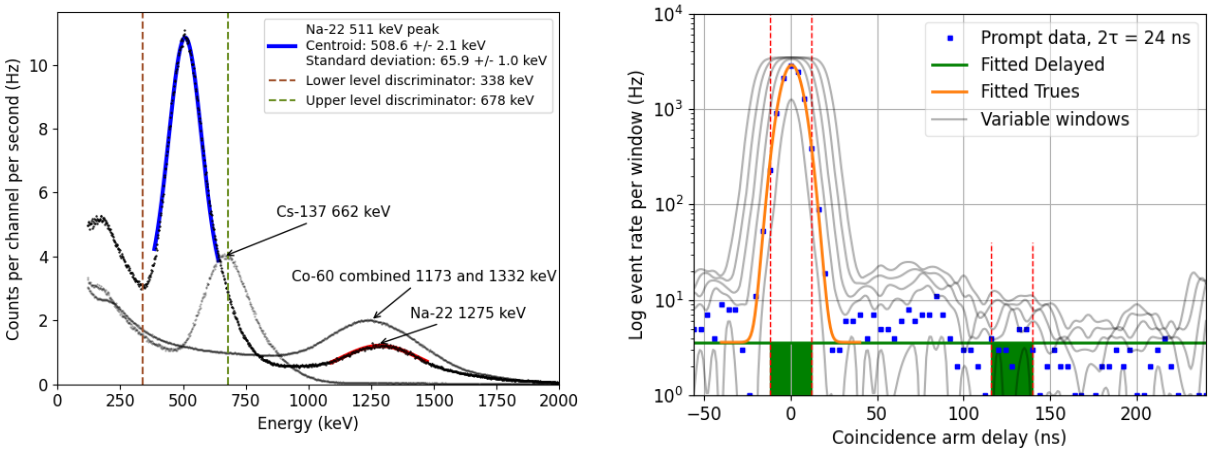

Figure 2. (Left) Calibrated energy spectra of three sources measured by a 951 detector block, with Gaussian curves fitted to the photopeaks. Optimal LLD and ULDs are shown as dashed vertical lines. (Right) The coincidence rate as a function of time delay added to a coincident module, plotted for various coincidence windows 2τ with the 24 ns case fitted in colour. Dashed vertical lines indicate window boundaries and the randoms contribution is shaded green.

window and the proportion of random coincidences increases linearly, as seen in figure 2 (right). Fitting a Gaussian function to the $2\tau = 8$ ns curve, a time resolution, given by the standard deviation of the distribution, of 4.24 ± 0.03 ns was determined. The energy and time resolutions of the HR+ series detector block were determined to agree with the values calculated for the 951 series block [9], implying these parameters are fixed by materials rather than geometry.

5. Conclusions and future work

Advances have been made in the development of a hybrid PEPT camera system, combining scintillator and semiconductor devices, for application to small-scale systems with micron-scale tracking precision. Construction of a modular BGO array has begun, using a numerically modelled sensitivity profile and 3D printed frames to enable the precise placement of detector modules. Energy and timing resolutions of the scintillator elements have been determined, allowing for the optimisation of system parameters for low-noise detection. Characterisation of the hybrid camera spatial resolution and detection efficiency have been made and deadtime parameters will follow, allowing for the study of micro-scale phenomena using PEPT.

References

[1] Alavi A, Werner T, Stepień E and Moskal P 2021 *Bio-Algorithms and Med-Systems* **17**(4) 203–212
[2] Parker D, Broadbent C, Fowles P, Hawkesworth M and McNeil P 1993 *Nucl. Instr. Meth.* **A326**(3) 592 – 607
[3] Buffler A, Govender I, Cilliers J, Parker D, Franzidis J P, Mainza A, Newman R, Powell M and Van der Westhuizen A 2009 *Int. Topical Meeting on Nuclear Research Applications and Utilization of Accelerators*
[4] Leadbeater T, Parker D J and Gargiuli J 2012 *Particuology* **10**(2) 146–153
[5] Hyslop N 2021 *Sub-Millimetre Positron-Emission Particle Tracking Using a CdZnTe Semiconductor Array* MSc thesis University of Cape Town
[6] van der Merwe R, Peterson S, Buffler A, van Heerden M, McKnight A and Leadbeater T 2022 *Proc. of SAIP2022, the 66th Annual Conf. of the South African Institute of Physics (July 1-8 Gqeberha)* submitted
[7] Leadbeater T and Parker D 2013 *7th World Congress in Industrial Process Tomography* pp 85–94
[8] H3D Inc. 2018 *J6400 High-Energy High-Flux Spectrometer* URL `https://h3dgamma.com/J6400Specs.pdf`
[9] McKnight A, Leadbeater T and van der Merwe R 2022 *Proc. of SAIP2022, the 66th Annual Conf. of the South African Institute of Physics (July 1-8 Gqeberha)* accepted

A.4 INPC 2022, Leadbeater

Conference proceedings produced as a co-author following an oral presentation by Tom Leadbeater at the 28th International Nuclear Physics Conference (INPC 2022), published September 2023.

Citation:
T Leadbeater et al 2023 J. Phys.: Conf. Ser. 2586 012127

Dynamics of physical flows measured by positron emission techniques

T Leadbeater, A Buffler, S Peterson, T Hutton, M van Heerden, A Camroodien, R van der Merwe, N Hyslop, and A McKnight

Metrological and Applied Sciences University Research Unit, Department of Physics, University of Cape Town, South Africa.

Tom.Leadbeater@uct.ac.za

Abstract. Short lived positron emitting species are used to produce flow-following tracer particles to study flow dynamics in a technique known as positron emission particle tracking (PEPT). The photon pairs produced by positron annihilation are detected in time coincidence by arrays of high-speed position sensitive detectors. Reconstruction of consecutive annihilations are used to determine the near-instantaneous position of the tracer particle. Hence, the resulting bulk flow dynamics are derived, including residence times, velocities, accelerations, and related kinematic properties. The Department of Physics at the University of Cape Town uses PEPT to study dynamic physical processes, turbulent, and multiphase flows. Studies aim to address global challenge topics including problems in water scarce environments, reducing industrial wastes, and enhancing developments towards sustainable economies through improved process efficiencies and design led approaches. The PEPT Cape Town enterprise is discussed, including the development of flow metrology systems and complementary nuclear measurement techniques. Research encompasses four key themes: radioisotope tracer production, instrumentation & detector development, data acquisition & processing, and flow metrology.

1. Nuclear measurement applications

The practical applications of nuclear research and resultant spin off technologies have had high impact for the benefit of human society. To this end the radioisotope tracer method has become an indispensable tool in practically every field of the physical sciences. The use of nuclear techniques applied to diagnosis and treatment in medical healthcare is illustrative [1]. Diagnostic imaging, combining advantages of distinctly different nuclear technologies, has revolutionised personalised healthcare. Of note, transmission imaging using X-ray CT has enabled internal structures of the body to be non-invasively visualised, being sensitive to density and material (Z) variations. Emission imaging (SPECT and PET) has equal relevance, with an injected substance subject to variations within the chemical and molecular environment informing on metabolic processes and function. Modern diagnostic tomography systems combining PET and X-ray CT allow function and structure to be simultaneously visualised and quantified at unprecedented precision. The use of similar techniques for the study of physical systems and those of industrial interest has been explored by a limited number of research groups [2,3] with potential impact appealing to global challenge issues including minimising energy and resource use, enhancing recycling, and enabling a knowledge led approach to industrial design. The University of Cape Town Department of Physics (UCT) has been active in using nuclear techniques to investigate fundamental, real-world, and industrially relevant flows in a wide variety of applications.

2. Emission imaging

The individual particles or fluid elements, in granular, fluid, and mixed-phase flows, cannot be individually distinguished. Radioisotope tracer techniques offer the best approach to differentiating particles from the bulk, which enables a particle-level study of their dynamic behaviour. The measurement process begins with a source(s) of suitable radioisotope (section 3), necessarily short-lived with correspondingly high specific activity. These must be easy to produce, have suitable emissions for detection (with positron emitters being the focus here), and be quickly and easily chemically synthesised within the short timeframe of their half-lives. The radioisotope must be attached to, or otherwise form, the material of interest for the study, being the equivalent of a radioisotope vector molecule in the medical sciences. Representation is critical, for the process to be non-invasive the material properties of the tracer must match those of the bulk. In studying liquids, a neutrally buoyant particle of small scale is used to represent a differential fluid element. Tracer particles are designed to be directly traceable to their mathematical counterparts in continuum mechanics, thus describing the bulk dynamic behaviour.

Photon emissions from a suitable tracer particle(s) are measured using arrays of position sensitive detectors external to the system under study (section 4). These photons carry information correlated with the tracer particle position and are measured with a form of collimation used to determine the direction of incidence. In positron imaging the photon pairs arising from electron-positron annihilation are detected in time coincidence to determine their flight path. The instrumentation and data acquisition systems are required to have low deadtime and high bandwidth to simultaneously acquire data from many thousands of individual detectors. The combined radioisotope, tracer particle, and detection system, enable a suite of novel experimental techniques suitable for investigating flow dynamics (section 5) [4]. A typical PET imaging protocol acquires emission data, applies a set of corrections, and back-projects (or otherwise reconstructs) the resultant integral image. In principle this approach can be used in studying physical systems, with the resulting image representing a time average of density or gated to represent a specific time sequence within the process. As dynamic quantities (including velocities, accelerations, and etc.) are of interest, a differential approach is preferred: following a freely moving tracer particle traversing the system under study. Over long timescales the average motion is equivalent to the integral approach, with the (near-)instantaneous timescale used to investigate dynamic behaviours.

The imaging system is 3-dimensional and regarded as non-intrusive (provided tracer particle representation). The annihilation photons can penetrate opaque materials and physical containment structures, enabling measurements under industrially relevant conditions including high temperatures and/or pressures. Under optimum conditions, with a tracer particle of sufficient activity and detector systems of high intrinsic efficiency and suitable geometry, the recorded coincidence rates are of the order MHz. From the raw data, locations along the tracer particle trajectory can be determined at 10 - 250 kHz rates, allowing high precision tracking with uncertainty proportional to the inverse square-root of the event rate, and ideally smaller than the tracer particle diameter [3]. For moving particles (benchmarked at 1 ms^{-1}), the displacement between successive locations is typically smaller than the measurement uncertainty. Through validation against standard motions, and including a well understood uncertainty budget, the accuracy of tracking is of the same order as the precision.

3. Radioisotope production and tracer particle fabrication

At the iThemba Laboratory for Accelerator Based Sciences (iThemba LABS), UCT has pioneered the use of $^{68}Ge/^{68}Ga$ radioisotope generators as a source of the high specific activity, short-lived, positron emitters required for PEPT. Germanium-68 (half-life 270.95 days) is produced by $^{nat}Ga(p, xn)^{68}Ge$ reactions using a 66 MeV proton beam impinging on a natural gallium target. Following separation and purification, the resulting ^{68}Ge is loaded onto SnO_2 based columns. The long-lived ^{68}Ge decays via electron capture to the short-lived positron emitting isotope ^{68}Ga (half-life 67.71 minutes) in liquid phase. The two isotopes initially exist in secular equilibrium, with a dilute hydrochloric acid solution used to elute the ^{68}Ga when required for tracer particle production via radiochemical techniques. The Radionuclide Production Department at iThemba LABS produces ^{18}F (half-life 109.8 minutes) using the $^{18}O(p, n)^{18}F$ reaction with enriched ^{18}O water targets, irradiated by an 11 MeV proton beam. The

isotope is synthesised to the ^{18}F-fluorodeoxyglucose molecule (^{18}FDG) via an automated rapid production cell. Both ^{68}Ge and ^{18}F (obtained from water targets or indirectly from ^{18}FDG) ions can be radiochemically manipulated to extract and concentrate the radioisotopic species. Similar (but distinctly different) ion exchange chromatography techniques are used to produce tracer particles with the radio-species exchanging with counter ions initially attached to a long chain resin polymer backbone [5]. The resin base-layer particle (200 – 500 μm diameter) can achieve a typical uptake of 400 μCi – 2 mCi depending on the chemical conditions in the solution. Once an active resin substrate is produced, further processing refines the physical (size, shape, density, elasticity, hardness, friction coefficient, etc.) and chemical (wettability, hydrophobicity or hydrophilicity, chemical potential, solubility, etc.) properties to match the characteristics of the desired bulk media, thereby attaining tracer particle representation.

With naturally occurring materials being of industrial interest, the ability to activate natural oxygen bearing materials (99.757% ^{16}O) to ^{18}F offers the supreme advantage over radiochemical tracer particle production. Possible reactions include the competing ^{16}O(^{3}He, p)^{18}F and ^{16}O(^{3}He, n)^{18}Ne → ^{18}F using a 35 MeV ^{3}He beam directed onto solid or water targets [2]. At iThemba LABS the competing ^{16}O(α, pn)^{18}F, and ^{16}O(α, d)^{18}F channels, with indirect production from ^{16}O(α, 2n)^{18}Ne → ^{18}F, have been explored [6]. Figure 1 illustrates possible reaction channels on oxygen bearing targets leading to ^{18}F, noting that production from natural oxygen is paramount in producing phase representation.

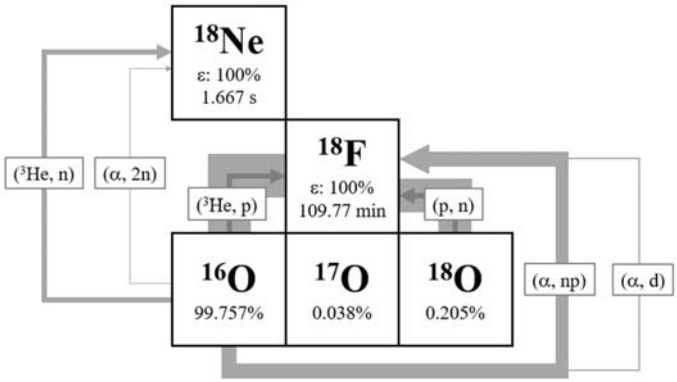

Figure 1. ^{18}F producing reaction channels from oxygen targets. The reaction pathways are scaled to the maximum microscopic cross-section, presented as millibarns / pixel. Data from reference [7].

4. Instrumentation & data acquisition

Large arrays of pixelated detectors are placed surrounding the system under study. The PEPT Cape Town laboratory at iThemba LABS hosts a modified ADAC Vertex dual-headed parallel plane gamma camera (NaI(Tl) scintillators) offering a large field of view and the ability to acquire in single photon (physical collimation) or coincidence (electronic collimation) modes with variable energy windows. The flagship device is a modified Siemens HR++ wide-bore tomograph of diameter 82.0 cm and 23.4 cm axial field of view (Figure 2, left). The HR++ uses detector blocks of 8 × 8 segmented bismuth germinate oxide (BGO) scintillator crystals, viewed by 4 photomultiplier tubes. Groups of 12 blocks are serviced by a detector controller functioning as a front-end data acquisition system, with blocks arranged to give 48 rings of crystal elements 4.1 mm transaxially × 4.0 mm axially × 30 mm radially. The front-end consists of variable gain pre-amplifiers, summing integrators and a single channel analyser (slow channel: determining event energy and crystal position) per block, and CFD timing (fast channel) at nanosecond resolution. Event data from each detector controller are transmitted in parallel to a lossless coincidence processor up to a deadtime limited rate of around 2 MHz per controller, where a coincidence gate of 12 ns is used to assign detected photons to annihilation pairs. Data describing the positions of the endpoints are transmitted over a high-speed fibre optic cable, timestamped, and written to disk storage in listmode format at a maximum rate of 16 MHz.

In the Department of Physics at UCT a dedicated nuclear physics research laboratory has been established. Modular detection systems utilising detector blocks as described above, and of differing

dimensions, have been developed for small-scale PEPT applications. A modular positron camera currently consists of 4 modules paired in opposing banks, with horizontal separation of 440 mm (Figure 2, middle). Detectors are controlled through serial communications allowing setting of energy windows, CFD parameters, and energy/spatial/temporal calibrations. Raw singles data are acquired as a serial listmode stream operating at 32.5 MHz, with data from each detector module acquired onto a 32-bit parallel bus. Data streams from up to 10 modules can be acquired simultaneously in parallel. The use of pixelated cadmium-zinc-telluride room-temperature semiconductor arrays (9680 pixels of $1.8 \times 1.8 \times 0.5$ mm^3), is being explored with a hybrid modular camera system consisting of both detector types offering the highest potential for precision measurements of small-scale flows. The design forms a field of view of $150 \times 200 \times 100$ mm^3, with a central high spatial resolution region [8], being described in detail in these proceedings [9]. A Siemens Biograph 16 combined PET/CT tomograph (Figure 2, right) capable of measuring structure (via X-ray attenuation) and function (via emission imaging) has recently been acquired (funded through the UCT Equipment Committee) [10]. The tomograph consists of a rotating X-ray source and opposing pixelated detector system, coupled to a ring of lutetium oxyorthosilicate (LSO) detector blocks of a similar design as described above, with 13 × 13 pixelation. Blocks are arranged into 39 rings of crystal elements of dimension 4.0 mm transaxially × 4.0 mm axially × 20 mm radially giving a uniform field of view of diameter 83.0 cm × 15.6 cm axially. The increased light output and faster decay time of the LSO scintillator improves the energy resolution and timing properties over the BGO based system, offering lower deadtime and higher data acquisition rates resulting in increased measurement precision. A novel fibre optic network-based data acquisition system supporting these devices in arbitrary geometrical configurations has been developed, enabling acquisition of singles and coincidences at the deadtime limited rates produced by the detectors. Real-time acquisition and processing enable the display of singles, coincidence, and tracking data, by sharing the computational load between multiple network nodes and utilising GPU vector processing.

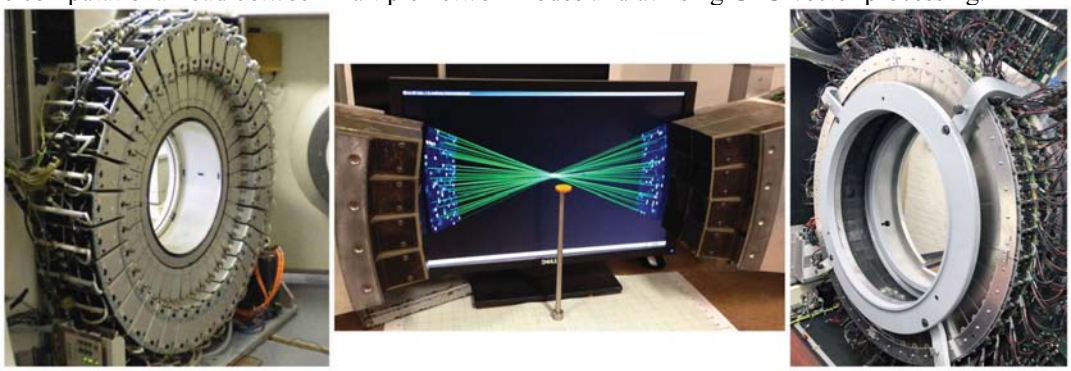

Figure 2. (Left) The HR++ scanner. (Middle) A modular positron camera of opposing banks of block detectors. The live display shows singles events per crystal (blue/white) and coincidence pairs (green lines) converging on the 3D representation of a centrally placed ^{22}Na calibration source (yellow disc). (Right) The Biograph 16 positron tomograph.

5. Positron emission & particle tracking

By regarding the tracer particle as stationary between consecutive coincidence events, the intersection of two reconstructed annihilation pairs is sufficient to localise the instantaneous position. In practice, due to contributions from random coincidences, scattering, and finite volume detector effects (which limit the overall spatial resolution in PET), a small number of consecutive events are used. An iterative minimisation approach rejects outlying events, and position is localised to a precision higher than the intrinsic spatial resolution due to the sampling statistics. The single particle Lagrangian viewpoint is therefore directly measured, with the ability to characterise dynamic processes and rapid changes unconstrained by the steady state or time averaged approaches usually used for flow visualisation. From the instantaneous trajectory data (time, position), first and second order time differentials can be

calculated to examine the velocity and acceleration vector fields, noting that these parameters cannot be measured from integral approaches. In a single phase, the local residence time (defined as the relative duration the tracer spends in each image voxel) is equivalent to the local material density. For more complex mixtures, the local densities of individual flow components are determined, being equivalent to steady state PET measurements of material concentration. Advantageously these analyses do not require the usual corrections for attenuation, scattering, or dead-time, and can be resolved to a higher precision than the equivalent integral measurements. Figure 3 illustrates the context of measurement.

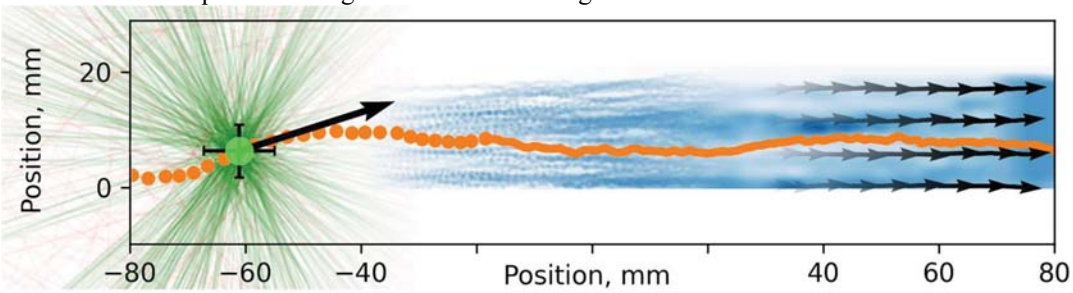

Figure 3. Measurements for a tracer moving in a laminar water channel of square cross-section. From left to right: A stylised single position measurement and associated velocity vector. A single pass through the channel is highlighted. The number of overlaid repeat passes increases until the full integral based description of local density (colour scale) and velocity field (vectors) is displayed.

6. Uncertainty, benchmarking, and validation towards metrology

The PEPT uncertainty budget is well understood, validated against known and established motions, and used to define the valid range(s) of applicability [3]. Three classes of motion can be considered, with equivalent, and increasingly sophisticated, analysis approaches. In the first, motion at constant velocity is used to determine uniformity of relative and absolute responses to position measurements, including stationary points and uniform linear motion produced using a robotic motion stage. In the second, motion at constant acceleration is used to determine the velocity response using uniform circular, or equivalent constant force, motion. Here, the laws of motion can be directly applied in validating the measurement against theoretical expectations. In the third, tracer particles moving within standard "textbook" flow conditions are investigated, with experimental data compared to those produced by theoretical modelling. Examples include unconstrained particles moving within convection cells or pipeline flows, with direct theoretical solutions enabling validation of all dynamic properties.

A simple validation process is outlined for uniformly accelerated motion, with tracer particles accelerating from rest under the influence of gravity. Upon release the particle accelerates with vertical displacement following the parabola $\frac{1}{2}gt^2$, with g the local gravitational acceleration and time t. Dividing the displacement by elapsed time resolves a linear relation proportional to the particle velocity, with respect to time the gradient of which measures the acceleration [11].

PEPT experiments were performed with a ^{68}Ga resin tracer inserted into a small steel ball placed within the field of view of the HR++ camera. An electromagnet supported the ball, which was allowed to drop by disconnecting the magnet current. The drop height was 40 cm, with the mass reaching a linear speed of ~1.5 ms^{-1} during the ~0.3 s flight time, before rebounding from the lower surface. Figure 4 shows the measured vertical trajectories (left) for repeated measurements alongside the analytical expectation. The same data, divided by elapsed time is shown (right), with the gradient of the parameterised line equal to $g/2$. A curve fitted to the linear section enables the gradient to be obtained (ignoring secondary effects such as air resistance), with g measured to be $9.798 \pm 0.001_{\text{stat}}$ ms^{-2}, correlating favourably with the accepted literature value of 9.796 ms^{-2} for our locale. This simple experiment, with a relatively high acceleration, is suitable to demonstrate that PEPT measurements are highly representative of the typical motions under consideration and can be extended to steady-state and transient flows without loss of accuracy [3].

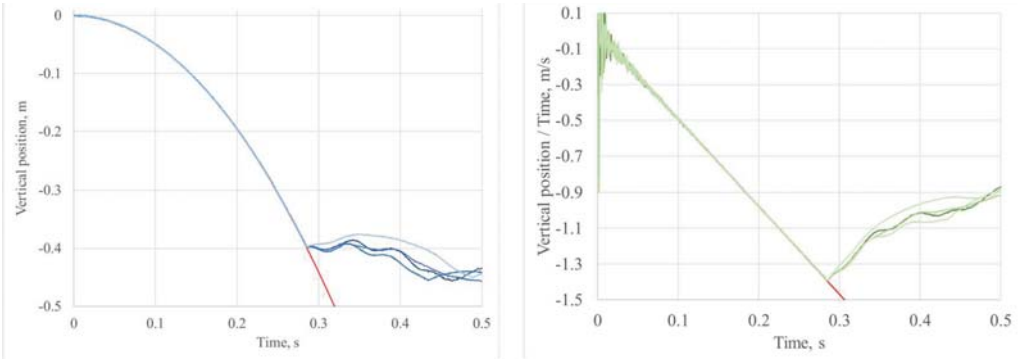

Figure 4. Analytical (red), measured vertical position (left, blue), and corresponding vertical velocity (right, green), measured for a small object falling from rest under gravitational acceleration.

7. Output and impact

Building on the validation of the measurement technique, a significant output from PEPT measurements has been in benchmarking direct measurement to theoretical models and simulations of flow processes. The Navier-Stokes equations describe a set of coupled partial derivatives used in modelling the motion of viscous substances with wide ranging applications. Due to their coupled nature integrable solutions do not exist, necessitating the use of precision measurement techniques such as PEPT to benchmark against, and to validate towards, the mathematical description. Measurement can be used to inform on dimensionless constants describing flow properties and/or provide numerical input data to theoretical models. PEPT has been extensively used in the study of mining and minerals applications, with experimental data informing underlying models of system behaviour, and used to optimise performance in terms of reducing waste streams, energy input, and raw materials requirements. From a design led approach, PEPT data have enabled greater understanding of material transport within flowing systems. In the case of flotation recovery cells, this approach has led to retrofitted adaptions of commercial units potentially saving millions of litres of water per year [12]. PEPT data are used to validate computational and/or theoretical models of turbulent flows and granular dynamics, perhaps offering the best experimental approach to non-invasively measuring flow in three dimensions.

References

[1] Jones T, Townsend D, 2017, J. Med. Imag. 4(1), 011013 (2017), doi: 10.1117/1.JMI.4.1.011013.
[2] Parker D, Broadbent C, Fowles P, Hawkesworth M and McNeil P 1993 Nucl. Instr. Meth. A326.
[3] Buffler A, Cole K, Leadbeater T W, van Heerden M, 2018, Int. J. Mod. Phys: Conference Series, 48, 1860113, 10.1142/S2010194518601138.
[4] Buffler A, Govender I, Cilliers J, Parker D, Franzidis J P, Mainza A, Newman R, Powell M and Van der Westhuizen A, 2009,Nuclear Research Applications and Utilization of Accelerators
[5] Camroodien A, van Heerden M, Nair S, Leadbeater T, 2021, Proc. of SAIP21, 65th Annual Conf. of the South African Institute of Physics (July 22-30 Potchefstroom).
[6] Leadbeater T W, Buffler A, Cole K, van Heerden M, Reich J, Camroodien A, Steyn D, 2023 Nuclear Science and Engineering, 10.1080/00295639.2023.2171234.
[7] Koning A, *et al.*, 2019, Nuclear Data sheets, 155.
[8] van der Merwe R, Peterson S, Buffler A, van Heerden M, McKnight A, Leadbeater T, 2022 Proc. Of SAIP2022, 66th Annual Conf. of the South African Institute of Physics (July 1-8 Gqeberha)
[9] van der Merwe R, Peterson S, Buffler A, van Heerden M, Hyslop N, Hutton T, and Leadbeater T, 2022, Proc. Int. Conf. on Nuclear Physics (September 12-16 Cape Town).
[10] McKnight A, Leadbeater T, van der Merwe R, 2022 Proc. of SAIP2022, 66th Annual Conf. of the South African Institute of Physics (July 1-8 Gqeberha).
[11] Wick K, Ruddick K, 1999, American J. of Physics 67, 962-965.
[12] Cilliers J, Cole K, 2013, UK Intellectual Property Office 1319600.1 (*Patent*).

A.5 NSS MIC RTSD 2023, van der Merwe

Abstract serving as conference proceedings produced as the primary author following an oral presentation at the 2023 IEEE Nuclear Science Symposium, Medical Imaging Conference and International Symposium on Room-Temperature Semiconductor Detectors (NSS MIC RTSD), published December 2023.

Citation:
R. van der Merwe, S. W. Peterson, A. Buffler, M. van Heerden and T. Leadbeater, Micro-scale particle tracking with hybrid detectors, 2023 IEEE Nuclear Science Symposium, Medical Imaging Conference and International Symposium on Room-Temperature Semiconductor Detectors (NSS MIC RTSD), Vancouver, BC, Canada, 2023, pp. 1-1, doi: 10.1109/NSSMICRTSD49126.2023.10338569.

Micro-scale particle tracking with hybrid detectors

Robert van der Merwe, Steve Peterson, Andy Buffler, Mike van Heerden, Tom Leadbeater

University of Cape Town, South Africa

Positron emission particle tracking (PEPT) is a tracer-based measurement technique used in the non-invasive study of dynamic and flowing systems. PEPT relies on positron imaging principles; using coincident detection of annihilation photons to determine the instantaneous 3D position of positron emitting tracers. Successful applications include laboratory scale systems across engineering disciplines, achieving millimetre spatial resolution and tracking speeds up to 10 m/s.

On smaller scales with reduced radiotracer activity, performance is limited by the efficiency of conventional fixed geometry detectors. To investigate micro-scale phenomena a modular hybrid system consisting of pixelated scintillator and semiconductor detectors has been constructed. 1024 BGO scintillator crystals (of mixed dimensions <6.75 x <6.25 x 30 mm^3) form a field of view 120 x 196 x 101 mm^3 with a pair of pixelated CZT room temperature semiconductors (9680 pixels of 1.8 x 1.8 x 0.5 mm^3) covering the central 62 x 42 x 20 mm^3 region at high spatial resolution.

Detection geometry was optimised through numerical modelling by maximising the absolute efficiency with high solid angle coverage of the scintillators, while enhancing the spatial resolution with the high pixelization of the semiconductors. At 511 keV, intrinsic efficiencies of 60% and 15%, and energy resolutions of 30.5% and 1.15%, were measured for the scintillators and semiconductors respectively. The combined high efficiency and high energy resolution enable precision windowing on detected events to discriminate noise. The timing resolution of both arrays was measured to be 12.7 ns and 268 ns respectively, allowing optimisation of coincidence gates. Sensitivity profile measurements were performed with a novel positioning stage benchmarked against modelling and demonstrating significant improvement in PEPT spatial resolution. Results indicate the potential study of micro-scale flows for the first time.